University College London

and

École Normale Supérieure de Lyon

Topological and Emergent Phenomena in Lattice BKT Systems

Michael Faulkner

A thesis submitted toward the degree of
Doctor of Philosophy

January 2015

I, Michael Faulkner, confirm that the work presented in this thesis is my own. Where information has been derived from other sources, I confirm that this has been indicated in the thesis.

This thesis is dedicated to the Harper, Denton, and McGrath families.

Abstract

This thesis addresses the emergent electrostatics of two-dimensional, toroidal magnetic models that possess XY symmetry, providing a platform for novel investigations into the Berezinskii-Kosterlitz-Thouless (BKT) phase transition.

The BKT transition drives the thermal dissociation of bound pairs of topological defects in many two-dimensional systems, including the two-dimensional XY model of magnetism. The XY model is closely analogous to the two-dimensional Coulomb gas, but can be simulated without computing the long-range interactions of the Coulombic system. This thesis elucidates this paradox by showing that Villain's approximation to the XY model is strictly equivalent to the Maggs-Rossetto (MR) electrostatic model when applied to the two-dimensional Coulomb gas.

The mapping is used to probe the BKT transition through the application of the MR algorithm to the two-dimensional Coulomb gas. By simulating the Coulombic system, fluctuations in the winding of charges around the torus are shown to turn on at the BKT transition temperature. These topological-sector fluctuations in the electric field therefore signal the high-temperature phase of the transition.

It is then shown that the effective critical exponent of Bramwell-Holdsworth (BH) theory can be measured in superfluid ^{4}He films, which correspond to effective Coulomb gases in the limit of large but finite system size. With the Coulombic system taken as the base BKT system, it is inferred that BH theory is a general property of BKT systems.

Résumé

Cette thèse s'intéresse aux phénomènes électrostatiques émergents dans les modèles magnétiques toroïdaux bi-dimensionnels à symétrie XY, fournissant ainsi un support pour de plus amples recherches dans le domaine de la transition de phase Berezinskii-Kosterlitz-Thouless (BKT).

Dans de nombreux systèmes bi-dimensionnels, dont le modèle bi-dimensionnel XY du magnétisme, la transition BKT contrôle la dissociation thermique de paires de défauts topologiques liés. Le modèle XY est analogue au gaz de Coulomb bi-dimensionnel, à ceci près qu'il peut être simulé sans avoir à modéliser les interactions à longue distance du système Coulombien. Cette thèse élucide ce paradoxe en démontrant que l'approximation de Villain appliquée au modèle XY est strictement équivalente au modèle électrostatique de Maggs-Rossetto (MR) appliqué au système Coulombien bi-dimensionnel.

Cette équivalence est utilisée pour sonder la transition BKT par l'application de l'algorithme MR au gaz de Coulomb bi-dimensionel. En simulant le système Coulombien, il est prouvé que les fluctuations dans l'organisation des charges autour du tore sont activées à la température de transition BKT. Ces fluctuations du champ électrique indiquent ainsi la phase de haute température de la transition.

Il est ensuite montré que l'exposant critique effectif de la théorie de Bramwell-Holdsworth (BH) peut être mesuré dans les films d'hélium 4 superfluide, qui correspondent à des gaz de Coulomb effectifs dans la limite de systèmes de grandes tailles finies.

Acknowledgements

First and foremost, I would like to thank my supervisors, Steven Bramwell and Peter Holdsworth. Peter and Steve form a unique and effective scientific partnership from which all of their students are very lucky to have benefited. Their input has been invaluable in both creating this work, and in developing my skills as a physicist.

I am grateful to the three of Steve and Peter's ex-students with whom I have had the most contact. When the science was proving tricky, Simon provided some support and advice that won't be forgotten. Adam was extremely helpful at the start of the project, with both the science and the French administration. Finally, not only did Andrea introduce me to programming at the beginning of the project, but it was his idea and investigation that led to Chapter 7 of this thesis: he has worked closely with us over the past six months while being very busy in the rest of his life. I am extremely thankful for his effort.

I thank everyone in Steve's spin-ice group for the scientific input, with a special thanks extended towards Marion for organising the group meetings. On the technical side of things, I'd also like to thank Gary Davies for many useful discussions, and Andrew Gormanly for his help with automating the repeated simulations that led to the results of Chapter 5.

The support staff at both the ENS and UCL have made everything as smooth as possible. At UCL, Rosie and Frédérique deserve special mentions for their help with the paperwork associated with a joint degree. At the ENS, Fatiha went out of her way to organise the three-month contract extension.

For the funding, I am grateful to both UCL and the CNRS for providing my stipend.

On a personal level, my life over the past three years would have been far less enjoyable without Rope Street and all those connected to the house, along with my friends from Nottingham and Kenilworth. At the LCN, there are too many people to thank for making the building what it is. Similarly at the Laboratoire, but I'd particularly like to thank Vojtech and David for the downtime during my visits. Finally, thanks to all of my extended family for the support and encouragement.

Contents

Abbreviations

AHNS	Ambegaokar-Halperin-Nelson-Siggia
BH	Bramwell-Holdsworth
BKT	Berezinskii-Kosterlitz-Thouless
GCE	Grand canonical ensemble
HXY	Harmonic XY
MEC	Minimum-energy configuration
MR	Maggs-Rossetto
PBCs	Periodic boundary conditions
RG	Renormalization group

Frequently Used Symbols

$\mathbf{A}$	Spin-wave propagator
A	Area of two-dimensional systems
a	Lattice spacing
$\mathbf{D}$	Externally applied, global electric field
D	Set of all charge-lattice or emergent-lattice sites
D'	Set conjugate to D / set of all spin-lattice sites
$\int \mathcal{D}\varphi$	Functional integral over all φ-variable values in the MR electrostatic model
$\int \bar{\mathcal{D}}\varphi$	Functional integral over all spin values
d	Dimensionality of the system
$\mathbf{E}$	Total electric field due to the charges and auxiliary field
$\hat{\mathbf{E}}$	Irrotational component of the total electric field due to the charges
$\tilde{\mathbf{E}}$	Lattice auxiliary field
$\bar{\mathbf{E}}$	Harmonic mode of the electric field due to the charges
$\bar{\mathbf{E}}_{\mathrm{p}}$	Polarization component of the harmonic mode of the electric field
$\bar{\mathbf{E}}_{\mathrm{w}}$	Winding component of the harmonic mode of the electric field
$\tilde{\mathbf{e}}$	Arbitrary purely rotational lattice vector field
F	Free energy of XY-type spin model
F^{SP}	Free energy of Salzberg-Prager system
$G(\mathbf{x}_i, \mathbf{x}_j)$	Green's function between positions $\mathbf{x}_i$ and $\mathbf{x}_j$
$G(\mathbf{0})$	Diagonal element of the Green's function
H_{HXY}	Hamiltonian of the HXY model
H_{SW}	Spin-wave Hamiltonian
H_{Villain}	Hamiltonian of the Villain model
H_{XY}	Hamiltonian of the XY model
J	Exchange constant (set to unity)
$K_{\mathrm{eff.}}$	Thermodynamic limit of the effective spin stiffness
K_{RG}	Effective spin stiffness found through RG techniques
$\tilde{K}_{\mathrm{eff.}}$	Finite-size effective spin stiffness
k_0	Longest-wavelength twist possible in HXY or XY models

k_{B}	Boltzmann's constant
L	Linear system size
$m(\mathbf{x})$	(Emergent) charge value at site $\mathbf{x}$ in units of q (2π)
N	Number of (emergent) charge or spin lattice sites
n	Number of (emergent) charges
n_m	Number of (emergent) charges of (emergent) charge value mq $(2\pi m)$
$\mathbf{P}$	The instantaneous (emergent) charge polarization of the (emergent) electrostatic system
$\mathbf{Q}$	The auxiliary gauge field for the continuum Maggs-Rossetto model
q	Elementary charge
q_i	Charge value of charge i
r_0	UV cut-off
$s(\mathbf{x}, \mathbf{x}')$	Modular variable between nearest-neighbour sites in D'
T	Temperature of the system
T_{BKT}	Screened BKT transition temperature for the standard Coulomb gas
$\bar{T}_{\mathrm{BKT}}$	Non-screened counterpart of T_{BKT}
$T_{\mathrm{BKT}}^{\mathrm{XY}}$	Screened BKT transition temperature for the XY model
$\tilde{T}_{\mathrm{BKT}}(L)$	Analogue of T_{BKT} measured through $\tilde{\Upsilon}$
$T^*(L)$	Low finite-size BKT transition temperature
$\tilde{T}^*(L)$	Analogue of $T^*(L)$ measured through $\tilde{\Upsilon}$
$T_{\mathrm{C}}(L)$	High finite-size BKT transition temperature
$\tilde{T}_{\mathrm{C}}(L)$	Analogue of $T_{\mathrm{C}}(L)$ measured through $\tilde{\Upsilon}$
$t(L)$	Reduced temperature
$\tilde{t}(L)$	Analogue of $t(L)$ measured through $\tilde{\Upsilon}$
U	Grand-canonical energy of the electrical system
$\tilde{U}$	Canonical energy of the electrical system
U_0	Internal energy of the electric fields
U_{Core}	Core-energy component of U
$U_{\mathrm{Harm.}}$	Harmonic-mode component of U_0
$U_{\mathrm{Int.}}$	Coulombic charge-charge interaction component of U_0
$U_{\mathrm{Rot.}}$	Auxiliary-field component of U_0
U_{Self}	Self-energy component of U_0
V	Volume of three-dimensional system
$\mathbf{w}$	Origin-independent winding field
$\mathbf{w}_0$	Origin-dependent winding field
X	Set of all possible charge-density configurations
$\bar{X}$	Set X with $q \equiv 2\pi$
$\mathbf{x}$	Position in space
$\mathbf{x}_i$	Position of particle or spin i

Y	Set of all possible $\boldsymbol{\nabla}^2\phi$ configurations
Z	Grand partition function of the Maggs-Rossetto model
$Z_{\mathrm{Coul.}}$	Grand partition function of the electrostatic system
$Z_{\mathrm{Coul.}}^{\mathrm{SP}}$	Partition function of the Salzberg-Prager system
$Z_{\mathrm{Coul.}}^{*}$	Reduced partition function of the Salzberg-Prager system
$Z_{\mathrm{eff.}}$	Effective partition function of XY-type spin models
Z_{HXY}	Partition function of the HXY model
$Z_{\mathrm{Rot.}}$	Auxiliary-field partition function of the Maggs-Rossetto model
Z_{SW}	Spin-wave partition function
Z_{Villain}	Partition function of the Villain model
Z_{XY}	Partition function of the XY model
β	Inverse temperature
$\tilde{\beta}$	Effective critical exponent of Bramwell-Holdsworth theory
$\tilde{\beta}^*$	Effective critical exponent of Bramwell-Holdsworth theory at $T = T^*(L)$
$\boldsymbol{\Delta}\theta$	Total microscopic-variable field / spin-difference field (inc. mod. periodicity)
$\boldsymbol{\Delta}\bar{\theta}$	MEC corresponding to $\boldsymbol{\Delta}\theta$
$\boldsymbol{\Delta}\psi$	Remainder of $\boldsymbol{\Delta}\theta$ once MEC is taken from the total
ϵ_0	Electric permittivity of free space (set to unity)
$\epsilon_c(m)$	Core-energy constant of each charge mq
$\epsilon_{\mathrm{eff.}}$	Effective electric permittivity of the Coulombic system
μ	Chemical potential of an elementary (emergent) charge
μ_{m}	Chemical potential of an (emergent) charge mq
ρ	Density of (emergent) charge
$\sum_{\langle \mathbf{x},\mathbf{x}'\rangle}$	Sum over nearest-neighbour sites in D'
Υ	Helicity modulus of an XY-type spin model
$\tilde{\Upsilon}$	Finite-size helicity modulus of an XY-type spin model
Υ_4	Fourth-order cumulant of an XY-type spin model
$\tilde{\Upsilon}_4$	Finite-size fourth-order cumulant of an XY-type spin model
Φ	Grand potential
ϕ	Electric scalar potential
ϕ_i	Electric scalar potential due to charge i
φ	Purely rotational microscopic variable / absolute value of spin
$\chi_{\bar{\mathbf{E}}}$	Harmonic-mode susceptibility
χ_{p}	Polarization susceptibility
χ_{w}	Winding-field susceptibility
$\chi_{\mathrm{w}}^{\mathrm{all}}$	Winding-field susceptibility using local and global moves
$\chi_{\mathrm{w}}^{\mathrm{global}}$	Winding-field susceptibility using global moves only
$\chi_{\mathrm{w}}^{\mathrm{local}}$	Winding-field susceptibility using local moves only

χ'	Standard susceptibility of electrostatic theory
Ω	Subsets of Euclidean space in which the continuum systems exist
$\boldsymbol{\nabla}\theta$	Continuum limit of $\boldsymbol{\Delta}\theta$
$\boldsymbol{\nabla}\theta_{\mathrm{Harm.}}$	Harmonic mode of $\boldsymbol{\nabla}\theta$
$\boldsymbol{\nabla}\bar{\theta}$	Continuum limit of $\boldsymbol{\Delta}\bar{\theta}$
$\boldsymbol{\nabla}\psi$	Continuum limit of $\boldsymbol{\Delta}\psi$
$\tilde{\boldsymbol{\nabla}}$	Forwards finite-difference operator
$\hat{\boldsymbol{\nabla}}$	Backwards finite-difference operator

Chapter 1

Introduction

The neutral Coulomb gas presents a statistical-mechanical problem in which the effect of dimensionality is particularly important. In three spatial dimensions, the continuum solution of Poisson's equation gives the well-known $1/r$ interaction potential. This potential is long-ranged, but is not quite sufficient to confine the positive and negative charges at finite temperature. In two spatial dimensions, however, the continuum solution of Poisson's equation gives a confining $\ln(r)$ potential. As first noted by Salzberg and Prager, who found an equation of state for the two-dimensional Coulomb gas [1], this results in a transition from a high-temperature phase of deconfined charge to a low-temperature phase of bound charge pairs.

Berezinskii [2], Kosterlitz and Thouless [3] discovered that the classical two-dimensional XY model of magnetism is, physically, very similar to the two-dimensional Coulomb gas. This mapping has a long history, fuelled by its remarkable statistical mechanics [2–4] and its relevance to a wide variety of experimental systems, such as superconducting films and two-dimensional Josephson junction arrays [5–8], superfluid films [9–12], liquid-crystal and polymer films [13], cold-atom systems [14], thin-film Bose-Einstein condensates [15, 16], superinsulating films [17, 18], and magnetic films and layers [19–21]. In the magnetic representation, the charge-binding transition discovered by Salzberg and Prager [1] becomes the famous Berezinskii-Kosterlitz-Thouless (BKT) transition [2, 3] that involves the unbinding of spin vortices: as the system passes through the transition temperature from the low-temperature phase, tightly bound vortex pairs unbind and destroy the quasi-long-range order of the system.

Despite the long history of the analogy between the XY model and the two-dimensional Coulomb gas, its precise form on a microscopic level is not so simple or transparent, and is not found in the pioneering work of BKT and others [2–4]. This omission was recognised by

Vallat and Beck [22], who provided the exact mapping between Villain's approximation to the XY model [23] and the two-dimensional Coulomb gas in the grand canonical ensemble (GCE). This thesis was inspired by this equivalence between the magnetic and Coulombic systems. From the outset, our aim was to further understand the mapping, and to present it in a more modern and transparent representation using the Maggs-Rossetto (MR) electrostatic model [24]. This led to a new measure of the BKT transition in Chapter 5, and to the generalization of Bramwell-Holdsworth (BH) theory [19, 20], which applies to magnetic films with XY symmetry, to all systems that are governed by BKT physics in Chapter 7.

Throughout this thesis, any real or model system that admits a BKT transition is termed a 'BKT system', and all systems will be square and subject to periodic boundary conditions (PBCs), unless stated otherwise. The PBCs enforce a toroidal topology, but the curvature of a true torus is not considered.

1.1 Thermodynamics and Phase Transitions

The thermodynamics of a system is the description of the system in its infinite-size limit: the thermodynamic limit. Any thermodynamic quantity is therefore only strictly defined for systems of infinite size, which, for most systems, corresponds to its macroscopic description. This definition is a consequence of the central limit theorem of statistics, which predicts that, for example, fluctuations from the mean of the internal energy per particle of a gas of N approximately independent particles is of the order $N^{-1/2}$, from which it follows that there are no fluctuations in this quantity in the thermodynamic limit. In general, most macroscopic volumes of matter at equilibrium can be treated as being in the thermodynamic limit. There are, however, some exceptions, one being the XY model of magnetism: this model is predicted to have zero magnetization in the thermodynamic limit [25], but the limit is approached so slowly that a magnetic film the size of the state of Texas for would still have finite magnetization [20]. Finite-size effects are therefore extremely important in the macroscopic description of this system.

Phase transitions are transformations of thermodynamic systems between different states of matter. Many phase transitions are measured by order parameters, which are zero in one phase and finite in the other: in a ferromagnetic system, for example, the order parameter is usually the magnetization of the system. This thesis revolves around the BKT transition, which governs the thermal dissociation of pairs of topological defects in the variety of different systems outlined above [5–21]. This phase transition is associated with a topological ordering, a term we will elucidate through the investigation presented in Chapter 5.

1.2 Monte Carlo Simulations

The majority of model systems are too complex for the analytic calculation of thermodynamic quantities. Simulations of the model systems are therefore performed in order to approximate the quantities of interest: throughout this thesis, the Metropolis Monte Carlo sampling procedure is used. This involves setting the components of the system in a certain initial configuration and then sampling a series of new configurations, which are either accepted or rejected on the basis of the Metropolis update scheme. Any configuration that is of a lower energy than that of the previous configuration is accepted; if, however, the energy change is not negative, the sampling procedure then accepts the new configuration if a random number in the set $[0, 1)$ is less than $\exp{(-\beta \Delta E)}$, where ΔE is the difference between the energies of the new and old configurations, $\beta := 1/k_{\mathrm{B}}T$ is the inverse temperature, k_{B} is Boltzmann's constant, and T is the temperature of the system. The exponential function effectively introduces a temperature to the system, by acting as an effective Boltzmann probability for the system changing from its initial to its final state at the temperature in question. Between a certain number of proposals, measurements of the system are then taken, from which the user is able to form approximate thermal averages of the desired quantities.

1.3 Topology and Ergodicity

Topology [26] and ergodicity [27] are two of the most important concepts in physics. In this thesis, it will be shown that they can both be used to classify the BKT phase transition outlined above.

In general, topology is the study of the properties of objects that are preserved under continuous deformation: it is the classification of shape. In the context of physics, this corresponds to the shapes of the fields that describe the systems in question. Divergences in electric fields, for example, cannot be removed by the continuous deformation (stretching or bending) of the fields: they can only be removed by operations such as the discrete reversal of field direction. Field configurations that contain a certain number and value of divergences - or topological defects - are classified as topologically distinct from field configurations that contain a different number or value of divergences. Topological defects are ubiquitous in nature, hence the importance of the concept of topology in physics.

The ergodic hypothesis states that a representative fraction of the accessible microstates of a real system will be visited by the system over a long enough period of time. (Note that, in a real system, the same thermal averages result from the representative fraction as though all accessible microstates have been visited.) A system is therefore in an ergodic state if its statistical averages are independent of the dynamics, provided the dynamics could theoretically explore all accessible microstates. When first introduced, this seems to be an abstract formalism of the language of physics, but it turns out to be very useful in classifying the states of certain systems. In this thesis, it will be shown that the two-dimensional Coulomb gas is classified as non-ergodic in the low-temperature phase of the BKT transition where charge is confined, but that it is classified as ergodic in the high-temperature phase where the charges are free to dissociate, or are deconfined. This is because it is valid to allow a global charge dynamics to complement the required local charge dynamics. The global dynamics amounts to winding a single charge around the torus, but, physically, confined charge can never wind around the torus: when charge is confined, the statistical averages are therefore dependent on the dynamics, and the system is in a non-ergodic state.

1.4 Aims and Thesis Plan

The aims of this thesis are to clearly present the mapping between the two-dimensional Coulomb gas and the two-dimensional XY model of magnetism in a modern and transparent representation and to then use this to both show the topological and ergodicity-breaking nature of the BKT transition, and to also generalize BH theory to all systems that are governed by BKT physics. To do this, the Coulomb interaction, the MR electrostatic model, the XY model, the BKT transition, and BH theory are introduced in Chapter 2. Following this, in Chapter 3, the standard physics of the two-dimensional lattice Coulomb gas is reformulated in a language suitable for the thesis, and an extension of the MR electrostatic model to the GCE in a lattice formalism is presented in detail in Chapter 4. The MR algorithm is then applied to the two-dimensional Coulomb gas in Chapter 5: this allows us to clearly describe the BKT transition in terms of topology and ergodicity. In Chapter 6, the equivalence between the MR electrostatic and Villain models in two spatial dimensions is shown, which allows us to define an emergent electric field for magnetic systems that possess XY symmetry, and to infer the relevance of Chapter 5 to experiment. Finally, in Chapter 7, the emergent-field representation outlined in Chapter 6 is applied to BH theory to generalize this theory to the general BKT system.

Chapter 2

Theoretical Background

This chapter is a review of the background material required for the thesis.

2.1 Classical Continuum Electrostatics

This project began with an analysis of the mapping between the two-dimensional XY model of magnetism and the two-dimensional lattice Coulomb gas. The theory of electrostatics on a lattice will therefore be analysed before being used to probe both the famous BKT transition [2, 3] and the mapping between the Coulomb gas and the ferromagnetic film.

Electrostatics is the theory of the interaction of stationary electric charges. This thesis concentrates on electrostatics in two spatial dimensions since this is considered to be the base system that admits BKT physics. Few electric charges are, however, known to behave two-dimensionally, so we begin with a discussion of three-dimensional continuum electrostatics, from which we will be able to form the axioms of the two-dimensional system.

2.1.1 Three-dimensional Electrostatics

In this subsection, the electric field is introduced before Gauss' law and the internal energy of the field are derived.

2.1.1.1 Gauss' Law

Three-dimensional electrostatics is governed by Coulomb's law [28]. This law states that the force experienced by one point charge q (q will be set as the elementary charge throughout) due to another point charge q_i in a vacuum is given by

$$\mathbf{F}_i(\mathbf{x}) = \frac{qq_i}{4\pi\epsilon_0}\frac{\mathbf{x}-\mathbf{x}_i}{|\mathbf{x}-\mathbf{x}_i|^3}\,\forall\mathbf{x}\neq\mathbf{x}_i, \tag{2.1}$$

where $\mathbf{x}$ and $\mathbf{x}_i$ are the positions of the charges q and q_i, respectively, and ϵ_0 is the electric permittivity of free space. (Note that this force does not account for any harmonic mode.) We generalize this to the force experienced by q due to a system of n point charges, and add a harmonic mode to the force $\bar{\mathbf{F}}$, which accounts for dipole-moment and charge-winding forces in general systems:

$$\mathbf{F}(\mathbf{x}) = \frac{q}{4\pi\epsilon_0}\sum_{i=1}^{n} q_i\frac{\mathbf{x}-\mathbf{x}_i}{|\mathbf{x}-\mathbf{x}_i|^3} + \bar{\mathbf{F}}\,\forall\mathbf{x}\neq\mathbf{x}_i. \tag{2.2}$$

The electric field experienced by some point charge q at $\mathbf{x}$ due to n other point charges is defined to be

$$\mathbf{E}(\mathbf{x}) := \frac{1}{q}\mathbf{F}(\mathbf{x}), \tag{2.3}$$

hence,

$$\mathbf{E}(\mathbf{x}) = \frac{1}{4\pi\epsilon_0}\sum_{i=1}^{n} q_i\frac{\mathbf{x}-\mathbf{x}_i}{|\mathbf{x}-\mathbf{x}_i|^3} + \bar{\mathbf{E}}\,\forall\mathbf{x}\neq\mathbf{x}_i, \tag{2.4}$$

where $\bar{\mathbf{E}} := \bar{\mathbf{F}}/q$ is the harmonic mode of the electric field. (We refer to a single harmonic mode because $\bar{\mathbf{E}}$ corresponds to the $\mathbf{k}=\mathbf{0}$ mode of the Fourier transform of the electric field, and we refer to this mode as harmonic because $\boldsymbol{\nabla}^2\,\bar{\mathbf{E}}=\mathbf{0}$, which follows from the standard vector calculus of constant vector fields.) From this, the superposition principle follows: the non-harmonic modes of the electric field experienced by a point charge are given by the sum of the non-harmonic modes of the fields due to each of the other constituent charges of the system. By defining the density of electric charge at some point $\mathbf{x}$ as

$$\rho(\mathbf{x}) := \sum_{i=1}^{n} q_i\delta^{(3)}(\mathbf{x}-\mathbf{x}_i), \tag{2.5}$$

we are able to rewrite Eq. (2.4) as

$$\mathbf{E}(\mathbf{x}) = \frac{1}{4\pi\epsilon_0}\int_\Omega \rho(\mathbf{x}')\frac{\mathbf{x}-\mathbf{x}'}{|\mathbf{x}-\mathbf{x}'|^3}d^3x' + \bar{\mathbf{E}}\,\forall\mathbf{x}\neq\mathbf{x}'. \tag{2.6}$$

Upon taking the divergence of both sides of Eq. (2.6),

$$\boldsymbol{\nabla}\cdot\mathbf{E}(\mathbf{x}) = \frac{1}{4\pi\epsilon_0}\int_\Omega \rho(\mathbf{x}')\boldsymbol{\nabla}_{\mathbf{x}}\cdot\left(\frac{\mathbf{x}-\mathbf{x}'}{|\mathbf{x}-\mathbf{x}'|^3}\right)d^3x'$$

$$=\frac{1}{\epsilon_0}\int_\Omega \rho(\mathbf{x}')\delta^{(3)}(\mathbf{x}-\mathbf{x}')d^3x', \tag{2.7}$$

we are left with Gauss' law:

$$\boldsymbol{\nabla}\cdot\mathbf{E}(\mathbf{x})=\rho(\mathbf{x})/\epsilon_0. \tag{2.8}$$

Note that $\boldsymbol{\nabla}_{\mathbf{x}}$ in Eq. (2.7) denotes that the divergence is taken with respect to the $\mathbf{x}$ variables. Eq. (2.8) shows that electric charges are topological defects in the electric field **E**: they puncture the electric field lines, which changes the topology of the electric field.

2.1.1.2 The Internal Energy

Upon supposing that the internal energy of the electric fields of the electrostatic system is given by

$$U_0=\frac{\epsilon_0}{2}\int_\Omega |\mathbf{E}(\mathbf{x})|^2 d^3x, \tag{2.9}$$

it follows, from the variational principle, that the functional

$$\mathcal{F}[\mathbf{E}(\mathbf{x})]:=\frac{\epsilon_0}{2}\int_\Omega |\mathbf{E}(\mathbf{x})|^2\, d^3x-\int_\Omega \bar{\phi}(\mathbf{x})\left(\epsilon_0\boldsymbol{\nabla}\cdot\mathbf{E}(\mathbf{x})-\rho(\mathbf{x})\right)d^3x, \tag{2.10}$$

which imposes Gauss' law, should be minimized with respect to the electric field for an electrostatic system in equilibrium. Here, $\{\bar{\phi}(\mathbf{x})\}$ acts as an infinite set of Lagrange multipliers introduced to enforce Gauss' law, and Ω is the subset of Euclidean space in which the charges exist. The functional is rearranged to

$$\begin{aligned}
\mathcal{F}[\mathbf{E}(\mathbf{x})]=&\frac{\epsilon_0}{2}\int_\Omega |\mathbf{E}(\mathbf{x})|^2\, d^3x-\epsilon_0\int_\Omega \bar{\phi}(\mathbf{x})\boldsymbol{\nabla}\cdot\mathbf{E}(\mathbf{x})d^3x+\int_\Omega \bar{\phi}(\mathbf{x})\rho(\mathbf{x})d^3x && (2.11)\\
=&\frac{\epsilon_0}{2}\int_\Omega |\mathbf{E}(\mathbf{x})|^2\, d^3x-\epsilon_0\boldsymbol{\nabla}\cdot\int_\Omega \bar{\phi}(\mathbf{x})\mathbf{E}(\mathbf{x})d^3x\\
&+\epsilon_0\int_\Omega \boldsymbol{\nabla}\bar{\phi}(\mathbf{x})\cdot\mathbf{E}(\mathbf{x})d^3x+\int_\Omega \bar{\phi}(\mathbf{x})\rho(\mathbf{x})d^3x && (2.12)\\
=&\frac{\epsilon_0}{2}\int_\Omega |\mathbf{E}(\mathbf{x})|^2\, d^3x-\epsilon_0\oint_{\partial\Omega} \bar{\phi}(\mathbf{x})\mathbf{E}(\mathbf{x})\cdot d\mathbf{a}(\mathbf{x})\\
&+\epsilon_0\int_\Omega \boldsymbol{\nabla}\bar{\phi}(\mathbf{x})\cdot\mathbf{E}(\mathbf{x})d^3x+\int_\Omega \bar{\phi}(\mathbf{x})\rho(\mathbf{x})d^3x, && (2.13)
\end{aligned}$$

where $d\mathbf{a}$ is an infinitesimal element of the surface of the system. The functional is varied with respect to the electric field:

$$\frac{\delta\mathcal{F}\left[\mathbf{E}(\mathbf{x}')\right]}{\delta\mathbf{E}(\mathbf{x})}=\epsilon_0\left(\mathbf{E}(\mathbf{x})+\boldsymbol{\nabla}\bar{\phi}(\mathbf{x})\right), \tag{2.14}$$

where the boundary term is assumed to be zero (which is the case for PBCs, certain Dirichlet and Neumann boundary conditions, and the infinite-size system). Hence, for a minimized functional, the electric field must be given by

$$\mathbf{E}(\mathbf{x}) = -\boldsymbol{\nabla}\phi(\mathbf{x}) + \mathbf{C}, \tag{2.15}$$

where

$$\bar{\phi}(\mathbf{x}) = \phi(\mathbf{x}) - \mathbf{C} \cdot \mathbf{x}. \tag{2.16}$$

Here, ϕ is the part of $\bar{\phi}$ that does not depend linearly on position, and $\mathbf{C}$ is a constant vector field.

By definition, the harmonic mode of the electric field is given by

$$\bar{\mathbf{E}} := \frac{1}{V}\int_{\Omega} \mathbf{E}(\mathbf{x}) d^3x. \tag{2.17}$$

Combining Eqs. (2.15) and (2.17), it follows that $\mathbf{C} = \bar{\mathbf{E}}$, because the non-harmonic modes of the electric field $-\boldsymbol{\nabla}\phi$ sum to zero. It therefore follows that the functional is minimized when the electric field is given by

$$\mathbf{E}(\mathbf{x}) = -\boldsymbol{\nabla}\phi(\mathbf{x}) + \bar{\mathbf{E}}. \tag{2.18}$$

Electric fields that describe electrostatics are, by definition, irrotational: rotational components generate magnetic fields that, in turn, accelerate electric charges. The functional therefore describes the electrostatics of a neutral charge fluid: Eq. (2.9) is taken to be the internal energy of the electric fields of the electrostatic system. The scalar field ϕ is the electric scalar potential that adheres to Poisson's equation of electrostatics:

$$\boldsymbol{\nabla}^2\phi(\mathbf{x}) = -\rho(\mathbf{x})/\epsilon_0. \tag{2.19}$$

$-\boldsymbol{\nabla}\phi$ and $\bar{\mathbf{E}}$ are referred to as the Poisson and harmonic components of the total electric field $\mathbf{E}$, respectively. The Poisson component is comprised of all $\mathbf{k} \neq \mathbf{0}$ modes of the electrostatic field.

2.1.1.3 The Green's Function

The internal energy of the electric fields is now rewritten in terms of the Green's function of the system. The Green's function $G(\mathbf{x}, \mathbf{x}')$ solves

$$\boldsymbol{\nabla}^2_{\mathbf{x}} G(\mathbf{x}, \mathbf{x}') = -\delta^{(3)}(\mathbf{x} - \mathbf{x}'), \tag{2.20}$$

which effectively amounts to stripping the information related to the charge value and the electric permittivity of free space from Poisson's equation. The above equation is solved by

$$G(\mathbf{x},\mathbf{x}') = \frac{1}{4\pi}\frac{1}{|\mathbf{x}-\mathbf{x}'|}\,\forall \mathbf{x} \neq \mathbf{x}', \tag{2.21}$$

while the diagonal element of the Green's function $G(\mathbf{x},\mathbf{x})$ is related to the self-energy of the charges. To write the internal energy of the electric fields in terms of the Green's function, the principle of superposition is applied to Eq. (2.9):

$$\begin{aligned}
U_0 =& \frac{\epsilon_0}{2}\int_\Omega |\mathbf{E}(\mathbf{x})|^2 d^3x && (2.22)\\
=& \frac{\epsilon_0}{2}\int_\Omega |-\boldsymbol{\nabla}\phi(\mathbf{x}) + \bar{\mathbf{E}}|^2 d^3x && (2.23)\\
=& \frac{\epsilon_0}{2}\int_\Omega |\boldsymbol{\nabla}\phi(\mathbf{x})|^2 d^3x - \epsilon_0\int_\Omega \boldsymbol{\nabla}\phi(\mathbf{x})\cdot\bar{\mathbf{E}}\,d^3x + \frac{\epsilon_0 V}{2}|\bar{\mathbf{E}}|^2 && (2.24)\\
=& \frac{\epsilon_0}{2}\int_{\partial\Omega} \phi(\mathbf{x})\boldsymbol{\nabla}\phi(\mathbf{x})\cdot d\mathbf{a}(\mathbf{x}) - \frac{\epsilon_0}{2}\int_\Omega \phi(\mathbf{x})\boldsymbol{\nabla}^2\phi(\mathbf{x})d^3x + \frac{\epsilon_0 V}{2}|\bar{\mathbf{E}}|^2 && (2.25)\\
=& -\frac{\epsilon_0}{2}\int_\Omega \phi(\mathbf{x})\boldsymbol{\nabla}^2\phi(\mathbf{x})d^3x + \frac{\epsilon_0 V}{2}|\bar{\mathbf{E}}|^2 && (2.26)\\
=& -\frac{\epsilon_0}{2}\int_\Omega \sum_{i=1}^n \phi_i(\mathbf{x})\boldsymbol{\nabla}^2\sum_{j=1}^n \phi_j(\mathbf{x})d^3x + \frac{\epsilon_0 V}{2}|\bar{\mathbf{E}}|^2 && (2.27)\\
=& -\frac{\epsilon_0}{2}\sum_{i,j=1}^n \int_\Omega \phi_i(\mathbf{x})\boldsymbol{\nabla}^2\phi_j(\mathbf{x})d^3x + \frac{\epsilon_0 V}{2}|\bar{\mathbf{E}}|^2 && (2.28)\\
=& \frac{\epsilon_0}{2}\sum_{i,j=1}^n \int_\Omega \frac{q_i}{\epsilon_0}G(\mathbf{x},\mathbf{x}_i)\frac{1}{\epsilon_0}q_j\delta^{(3)}(\mathbf{x}-\mathbf{x}_j)d^3x + \frac{\epsilon_0 V}{2}|\bar{\mathbf{E}}|^2 && (2.29)\\
=& \frac{1}{2\epsilon_0}\sum_{i,j=1}^n q_i G(\mathbf{x}_i,\mathbf{x}_j)q_j + \frac{\epsilon_0 V}{2}|\bar{\mathbf{E}}|^2 && (2.30)\\
=& \frac{G(\mathbf{x},\mathbf{x})}{2\epsilon_0}\sum_{i=1}^n q_i^2 + \frac{1}{2\epsilon_0}\sum_{i\neq j} q_i G(\mathbf{x}_i,\mathbf{x}_j)q_j + \frac{\epsilon_0 V}{2}|\bar{\mathbf{E}}|^2 && (2.31)\\
=& \frac{G(\mathbf{0})}{2\epsilon_0}\sum_{m\in\mathbb{Z}} n_m m^2 q^2 + \frac{1}{2\epsilon_0}\sum_{i\neq j} q_i G(\mathbf{x}_i,\mathbf{x}_j)q_j + \frac{\epsilon_0 V}{2}|\bar{\mathbf{E}}|^2 && (2.32)\\
=& U_{\text{Self}} + U_{\text{Int.}} + U_{\text{Harm.}}, && (2.33)
\end{aligned}$$

where $G(\mathbf{0}) := G(\mathbf{x},\mathbf{x})$, ϕ_i is the electric scalar potential due to particle i, $d\mathbf{a}$ is an infinitesimally small surface element, n_m is the number of charges mq, $m(\mathbf{x}) \in \mathbb{Z}$ is the electric charge at $\mathbf{x}$ in units of q, and $U_{\text{Self}} := \sum_{m\in\mathbb{Z}} n_m m^2 q^2 G(\mathbf{0})/2\epsilon_0$, $U_{\text{Int.}} := \sum_{i\neq j} q_i G(\mathbf{x}_i,\mathbf{x}_j)q_j/2\epsilon_0$ and $U_{\text{Harm.}} := \epsilon_0 V|\bar{\mathbf{E}}|^2/2$ are, respectively, the self-energy, Coulombic charge-charge interaction and harmonic-mode components of the internal energy of the electric fields U_0. The coupling between the harmonic and non-harmonic modes of the electric field in the third line of the above working is zero because the harmonic term moves outside of the integral and the spatial integral over the non-harmonic ($\mathbf{k} \neq \mathbf{0}$) modes is zero; the surface term in the fourth line is zero for systems with PBCs, or for systems in the thermodynamic limit, in which fields are assumed to vanish at the boundaries. Note that, while $U_{\text{Int.}}$ can be negative, the sum $U_{\text{Self}} + U_{\text{Int.}}$ is necessarily ≥ 0 as it arises from the term in $|\boldsymbol{\nabla}\phi|^2$.

2.1.1.4 The Chemical Potential

The full chemical potential for the introduction of a charge corresponds to the energy required to introduce each charge to the system, ignoring the Coulombic charge-charge interaction and harmonic components of the internal energy of the electric fields. This energy is a combination of the self-energies of the particles and a set of tuneable core energies. One may restrict to systems of certain charge species via the addition of the core-energy component of the internal energy:

$$U_{\text{Core}} := \frac{1}{2} \sum_{m \in \mathbb{Z}} n_m \epsilon_c(m) m^2 q^2. \tag{2.34}$$

Here, $\epsilon_c(m)$ is the core-energy constant of each charge mq, and $\epsilon_c(m) = \epsilon_c(-m)$, since charges are excited to the vacuum in neutral pairs. We extend the internal energy to include this term:

$$U := U_0 + U_{\text{Core}} = U_{\text{Self}} + U_{\text{Int.}} + U_{\text{Harm.}} + U_{\text{Core}}. \tag{2.35}$$

This is the grand-canonical energy of the whole system, whereas U_0 is the internal energy of the electric fields only.

We define the chemical potential

$$\mu_m := - \left[\frac{G(\mathbf{0})}{\epsilon_0} + \epsilon_c(m) \right] \frac{m^2 q^2}{2} \tag{2.36}$$

for the introduction of a charge mq, so that the grand-canonical energy U is now given by

$$U = - \sum_{m \in \mathbb{Z}} \mu_m n_m + \frac{1}{2\epsilon_0} \sum_{i \neq j} q_i G(\mathbf{x}_i, \mathbf{x}_j) q_j + \frac{\epsilon_0 V}{2} |\bar{\mathbf{E}}|^2. \tag{2.37}$$

One may then set infinite core energies for the addition of certain charge species such that the grand potential $\Phi := U - TS$ diverges positively upon their addition, thereby inhibiting the existence of the species. Note that $U \equiv \tilde{U} - \sum_{m \in \mathbb{Z}} \mu_m n_m$, where $\tilde{U}$ is the internal energy of electrostatics in the canonical ensemble.

2.1.2 Two-dimensional Electrostatics

The Green's function and the axioms of three-dimensional electrostatics are now applied to the two-dimensional system.

2.1.2.1 The Internal Energy and Gauss' Law

The grand-canonical energy of a three-dimensional electrostatic system is given by

$$U = \frac{\epsilon_0}{2}\int_\Omega |\mathbf{E}(\mathbf{x})|^2 d^3x + U_{\text{Core}}, \tag{2.38}$$

and the electric fields must adhere to Gauss' law,

$$\boldsymbol{\nabla}\cdot\mathbf{E}(\mathbf{x}) = \rho(\mathbf{x})/\epsilon_0. \tag{2.39}$$

These are the axioms of three-dimensional electrostatics, which we generalize to d-dimensional systems and consider the $d = 2$ case, whose grand-canonical energy is given by

$$U = \frac{\epsilon_0}{2}\int_\Omega |\mathbf{E}(\mathbf{x})|^2 d^2x + U_{\text{Core}}, \tag{2.40}$$

where the units of the electric field $\mathbf{E}$ and the electric permittivity of the vacuum ϵ_0 in two spatial dimensions are outlined in detail in Appendix A (for the lattice electric fields, but the units are identical to the continuum system).

The two-dimensional Green's function adheres to the two-dimensional analogue of Poisson's equation. Away from a single point charge positioned at the origin,

$$\frac{1}{r}\frac{\partial}{\partial r}\left(r\frac{\partial}{\partial r}G(r,\mathbf{0})\right) = 0\,\forall r \neq 0, \tag{2.41}$$

where we have dropped any angular dependence as we have assumed rotational symmetry. This is solved by

$$G(\mathbf{x},\mathbf{0}) = B\ln\left|\frac{\mathbf{x}}{r_0}\right|\ \forall\mathbf{x}\neq\mathbf{0}, \tag{2.42}$$

where B and r_0 are integration constants. We set $B = -1/2\pi$ to satisfy Gauss' law and generalize to source charges at position $\mathbf{x}'$:

$$G(\mathbf{x},\mathbf{x}') = -\frac{1}{2\pi}\ln\left|\frac{\mathbf{x}-\mathbf{x}'}{r_0}\right|\ \forall\mathbf{x}\neq\mathbf{x}'. \tag{2.43}$$

Eq. (2.37) then tells us that the grand-canonical energy for a system of electric charges in a two-dimensional continuum is given by

$$U = -\sum_{m\in\mathbb{Z}} \mu_m n_m - \frac{1}{4\pi\epsilon_0}\sum_{i\neq j} q_i \ln\left|\frac{\mathbf{x}_i - \mathbf{x}_j}{r_0}\right| q_j + \frac{\epsilon_0 A}{2}|\bar{\mathbf{E}}|^2, \tag{2.44}$$

where A is the area of the two-dimensional system, and the chemical potentials μ_m and the core-energy component of the grand-canonical energy U_{Core} are both defined as in the three-dimensional case.

2.1.2.2 Salzberg-Prager Theory

Two-dimensional electric charges are tightly bound in neutral pairs by their logarithmic interaction potential: this gives rise to the BKT phase transition. In the context of the two-dimensional Coulomb gas, this insulator-conductor transition was first discovered by Salzberg and Prager, who derived [1] an equation of state for a simply connected, square, continuum system of linear size L that predates BKT theory [2, 3]. Salzberg and Prager proceeded as follows.

From the expression for the grand-canonical energy of the system given by Eq. (2.44), one can transform to the canonical ensemble ($\tilde{U} = U + \sum_{m\in\mathbb{Z}} \mu_m n_m$) in which charge-species number is fixed and write the Salzberg-Prager partition function $Z_{\text{Coul.}}^{\text{SP}}$ as

$$Z_{\text{Coul.}}^{\text{SP}} := \int \mathcal{D}\mathbf{x}\, e^{\beta\sum_{i\neq j} q_i q_j \ln(|\mathbf{x}_i - \mathbf{x}_j|/r_0)/4\pi\epsilon_0}, \tag{2.45}$$

where the contribution from the harmonic mode of the electric field is assumed to be vanishingly small. This is a functional integral over all positions of all constituent charges, where the charge-species number is fixed, and each charge configuration is assigned the Boltzmann weighting $\exp\left[-\beta\tilde{U}\left(\{\mathbf{x}_i\},\{n_m\}\right)\right]$ (under the assumption of the vanishingly small contribution from the harmonic mode). Here, the functional integral $\int \mathcal{D}\mathbf{x}$ is defined as

$$\int \mathcal{D}\mathbf{x} := \prod_{m\in\mathbb{Z}}\left[\frac{1}{n_m!}\right]\prod_{i=1}^{n}\left[\int_\Omega d^2x_i\right], \tag{2.46}$$

where

$$\int_\Omega d^2x_i := \int_{r_0}^{L} dx_i \int_{r_0}^{L} dy_i \tag{2.47}$$

is the integral of the position of particle i over the area of the system. Here, r_0 is the UV cut-off, representing an effective radius of the particles.

In order to approximately isolate the system-size dependence of the partition function, Salzberg and Prager defined the coordinate system

$$\mathbf{x}'_i := \mathbf{x}_i/L, \tag{2.48}$$

and the measure

$$\int_{\Omega/L^2} d^2x'_i := \int_{r_0/L}^{1} dx'_i \int_{r_0/L}^{1} dy'_i, \tag{2.49}$$

so that the Salzberg-Prager partition function becomes

$$\begin{aligned} Z^{\mathrm{SP}}_{\mathrm{Coul.}} =& \prod_{m\in\mathbb{Z}} \left[\frac{1}{n_m!}\right] \prod_{i=1}^{n} \left[L^2 \int_{\Omega/L^2} d^2x'_i\right] e^{\beta \sum_{i\neq j} q_i q_j \ln(L|\mathbf{x}'_i - \mathbf{x}'_j|/r_0)/4\pi\epsilon_0} \\ =& L^{2n} \int \bar{\mathcal{D}}\mathbf{x}' e^{\beta \sum_{i\neq j} q_i q_j (\ln(L) + \ln(|\mathbf{x}'_i - \mathbf{x}'_j|/r_0))/4\pi\epsilon_0} \\ =& L^{2n} L^{\beta \sum_{i\neq j} q_i q_j/4\pi\epsilon_0} Z^{*}_{\mathrm{Coul.}}, \end{aligned} \tag{2.50}$$

where

$$Z^{*}_{\mathrm{Coul}} := \int \bar{\mathcal{D}}\mathbf{x}' e^{\beta \sum_{i\neq j} q_i q_j \ln(|\mathbf{x}'_i - \mathbf{x}'_j|/r_0))/4\pi\epsilon_0} \tag{2.51}$$

is the normalized Salzberg-Prager partition function, and the measure $\int \bar{\mathcal{D}}\mathbf{x}'$ is defined via

$$\int \bar{\mathcal{D}}\mathbf{x}' := \prod_{m\in\mathbb{Z}} \left[\frac{1}{n_m!}\right] \prod_{i=1}^{n} \left[\int_{\Omega/L^2} d^2x'_i\right]. \tag{2.52}$$

The Salzberg-Prager free energy is then given by

$$F^{\mathrm{SP}} = -\,\beta^{-1} \ln\left(Z^{*}_{\mathrm{Coul.}} A^{n(1-\beta q^2/8\pi\epsilon_0)}\right) \tag{2.53}$$

for the neutral Coulomb gas of elementary charges, since $\sum_{i\neq j} q_i q_j = -nq^2$ in this case.

The pressure that the system exerts on its boundaries is defined by

$$p := -\frac{\partial F^{\mathrm{SP}}}{\partial A}. \tag{2.54}$$

The normalized component of the partition function $Z^{*}_{\mathrm{Coul.}}$, which contains all charge-screening information, has a system-size dependence arising from the lower bound of its functional integral over charge positions. To proceed, however, Salzberg and Prager assumed that the system-size dependence of $Z^{*}_{\mathrm{Coul.}}$ is negligible, which is a good approximation for large systems in the limit of low charge density, thereby ignoring charge screening. The Salzberg-Prager equation of state for the non-screened, two-dimensional Coulomb gas of elementary charges in the continuum vacuum is therefore given by

$$p = \beta^{-1}\frac{n}{A}\left(1 - \beta q^2/8\pi\epsilon_0\right), \tag{2.55}$$

or

$$pA = nk_{\mathrm{B}}T\left(1 - \frac{q^2}{8\pi\epsilon_0 k_{\mathrm{B}}T}\right). \tag{2.56}$$

The above equation predicts that a two-dimensional Coulomb gas constrained to limitingly low charge density experiences a change from positive to negative pressure as it is cooled through the non-screened BKT transition temperature,

$$\bar{T}_{\mathrm{BKT}} = \frac{q^2}{8\pi\epsilon_0 k_{\mathrm{B}}}. \tag{2.57}$$

This is the BKT transition temperature for the Salzberg-Prager system: negative pressure is a characteristic of charge confinement. Charge-screening corrections, however, lower this transition temperature for the Coulomb gas of many charges. In the GCE, one is at liberty to tune the chemical potentials by varying the core-energy constant of each charge species, which, in turn, controls the thermal average of the number of charges in the system. For the harmonic XY (HXY) model [20, 22], $q = 2\pi$ and the core-energy constant is intrinsically set to zero (this will be outlined in detail in Chapter 6, where it will also be stated that non-elementary topological defects are not geometrically possible in the XY models). The standard core-energy configuration of the Coulomb gas is therefore taken to be $\{\epsilon_c(m = 0, \pm 1) = 0, \epsilon_c(m \neq 0, \pm 1) = \infty\}$ with the elementary charge set to $q = 2\pi$: upon setting $\epsilon_0 = k_{\mathrm{B}} = 1$, charge-screening corrections in this standard system then lower the bare, non-screened transition temperature $\bar{T}_{\mathrm{BKT}} = \pi/2$ to $T_{\mathrm{BKT}} = 1.35$ (to three significant figures) [29], which is the standard BKT transition temperature for the Coulomb gas in the literature. Throughout this thesis, this transition temperature is taken to be the BKT transition temperature for the Coulomb gas. It is stressed here that the BKT transition is driven by a competition between confining energy and entropy, and that its transition temperature is then lowered through charge screening. Note that the transition temperature of the XY model is lowered further due to the anharmonic terms in the cosine interaction potential.

Throughout the remainder of this thesis, we set $\epsilon_0 = k_{\mathrm{B}} = 1$ and $q = 2\pi$, but we may write each quantity explicitly to help the reader in identifying units.

2.2 The Maggs-Rossetto Electrostatic Model: Background

The MR algorithm [24], formulated by Maggs and co-workers [24, 30–34], simulates the physics of Coulombic interactions on a lattice via local electric-field updates, avoiding the need to treat computationally intensive long-range interactions. Its corresponding model introduces a freely fluctuating auxiliary field that is divergence free everywhere. This extends the electrostatic solution of Gauss' law to the general solution and results in local field updates alone being sufficient for the system to efficiently explore the Gibbs ensemble of the electrostatic problem. The validity of introducing the auxiliary field is seen in the context of the separability of the partition function into its Coulombic and auxiliary components: the auxiliary field contributes to the internal energy of the electric fields, but is statistically independent of the Coulombic element. A similar lattice-field model was formulated by Raghu *et al.* for the two-dimensional system [35].

MR formulated their model in the three-dimensional continuum. The general solution to Gauss' law is given by

$$\mathbf{E}(\mathbf{x}) = -\boldsymbol{\nabla}\phi(\mathbf{x}) + \boldsymbol{\nabla} \times \mathbf{Q}(\mathbf{x}) + \bar{\mathbf{E}}, \tag{2.58}$$

where $\mathbf{Q}$ is the auxiliary gauge field ($\boldsymbol{\nabla} \times \mathbf{Q}$ is the auxiliary field). Gauss' law follows:

$$\boldsymbol{\nabla} \cdot \mathbf{E}(\mathbf{x}) = \rho(\mathbf{x})/\epsilon_0. \tag{2.59}$$

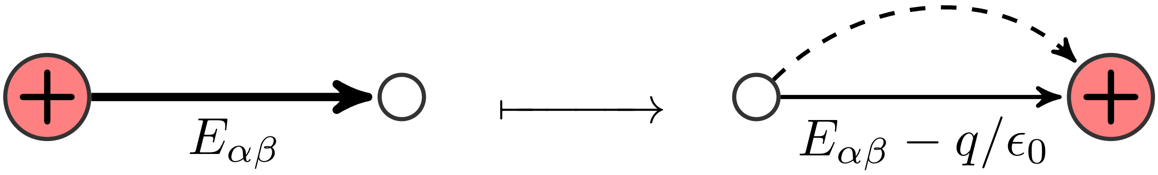

FIGURE 2.1: A charge-hop update: The field bond connecting charge sites α and β is updated to mimic a charge hopping from site α to β such that Gauss' law is obeyed. This updates all degrees of freedom of the field. The solid arrow represents the field flux flowing from site α to site β, with the thickness of the arrow representing its relative magnitude; the curly, dashed arrow represents the charge hopping; the white circle is an empty charge site; the red circle is a site occupied by a positive charge.

Using a lattice model, Maggs and co-workers initially consider the charge-hop updates depicted in Fig. 2.1. This first update alters the electric field to mimic a charge hopping between two lattice sites. They suppose site α is initially occupied by a positive charge, and its neighbouring site β is initially an empty charge site. When considering the new charge configuration in which the charge has moved to site β, one attempts the electric-field update corresponding to $E_{\alpha\beta} \mapsto E_{\alpha\beta} - q/\epsilon_0$ via standard sampling, where $E_{\alpha\beta}$ denotes the electric flux flowing from site α to site β. Gauss' law is satisfied by the new charge configuration, as required.

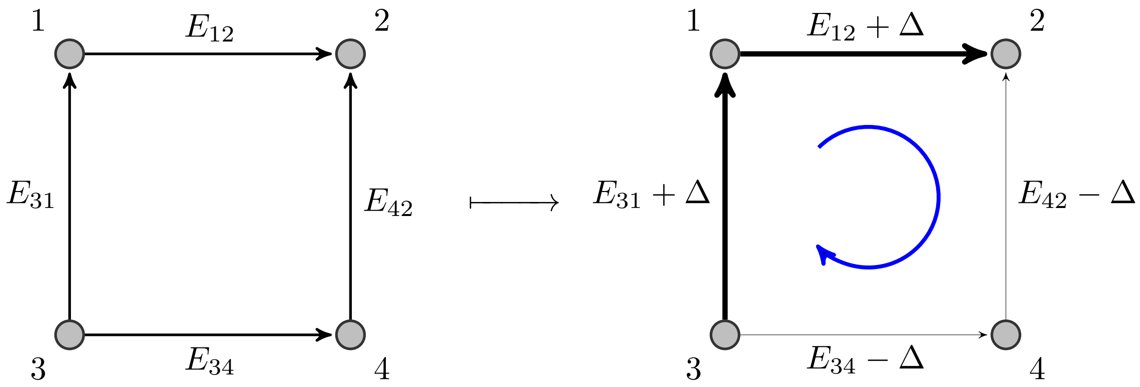

FIGURE 2.2: An update of the rotational degrees of freedom of the electric field: The flux is rotated by an amount Δ around a randomly-chosen lattice plaquette, leaving Gauss' law satisfied. The black arrow represents the flux flowing from site α to site β, with the thickness of the arrow representing its relative magnitude; the blue arrow represents the direction of flux rotation; the grey circles represent sites of arbitrary charge.

The charge-hop update alters all degrees of freedom of the field. Electrostatics, however, is described by field configurations for which the auxiliary field is strictly zero, hence the algorithm explicitly samples the auxiliary gauge field to improve efficiency. This involves randomly selecting a lattice plaquette and proposing a rotation of the electric field around the plaquette such that the new field configuration satisfies Gauss' law and leaves the charge configuration unchanged, as shown in Fig. 2.2. Sampling a suitable ratio of the two local field updates described here allows the system to reproduce Coulombic physics.

The algorithm may also employ a global update of the harmonic mode of the electric field to improve efficiency.

2.3 The Two-dimensional XY Model of Magnetism

The classical two-dimensional XY model of magnetism remains an area of active interest in condensed-matter physics due in part to its experimental relevance outlined in Chapter 1 [5–21]. BKT showed [2, 3] that the system is critical in the low-temperature phase but paramagnetic above the BKT transition temperature. Villain proposed [23] an analytic approximation to the XY model that separates the roles of spin vortices and spin waves, the latter of which dominate fluctuations in the critical phase. The HXY model, a simplification of the Villain model that captures the physics of the BKT transition, was later independently introduced by Vallat and Beck [22] and BH [20]. In this section, we review these three models.

2.3.1 Physical Background

Magnetic systems can be modelled using spin models. Spin is a quantum-mechanical phenomenon that causes certain particles to possess an intrinsic magnetic moment that cannot be explained by its orbital angular momentum. In general, magnetic particles have both a spin and an orbital contribution to their magnetic moment, but, for most purposes, the total moment can be represented by an effective spin operator. For this reason, spin models can be used to describe real magnets, and magnetic moments are often referred to as spins.

In materials, spins can interact with one another in a variety of different ways. One such interaction is the exchange interaction, which causes interacting spins to either align or anti-align in the zero-temperature state of the (non-frustrated) system in which all spins are correlated. A system in which all the spins are aligned with one another gives rise to a macroscopic magnetization of the system: this is ferromagnetism (the ground state of a system whose spins anti-align is an antiferromagnet). As the temperature of such a system is increased, thermal effects can dominate the exchange effects to destroy the ferromagnetism, leaving the system in an uncorrelated, paramagnetic state.

At finite temperature, non-frustrated ferromagnetic spin systems that are dominated by exchange-interaction effects can be modelled as systems of classical spins with a Hamiltonian given by

$$H = -J \sum_{\langle \mathbf{x},\mathbf{x}' \rangle} \mathbf{s}(\mathbf{x}) \cdot \mathbf{s}(\mathbf{x}'), \tag{2.60}$$

where $J > 0$ is the exchange constant, $\mathbf{s}(\mathbf{x})$ is the spin vector at site $\mathbf{x}$, and the sum is over nearest-neighbour spin sites only, since nearest-neighbour effects are assumed to dominate.

The XY model of magnetism uses this Hamiltonian for planar spins on a two-dimensional lattice. Its normalized spin field is given by

$$\mathbf{s}(\mathbf{x}) := (\cos(\varphi(\mathbf{x})), \sin(\varphi(\mathbf{x}))), \tag{2.61}$$

where φ is the phase of each spin, and is referred to as the spin at each lattice point (the spins are represented by arrows in Fig. 2.3). The Hamiltonian of the XY model becomes

$$H_{\text{XY}} = -J \sum_{\langle \mathbf{x},\mathbf{x}' \rangle} \cos(\varphi(\mathbf{x}) - \varphi(\mathbf{x}')). \tag{2.62}$$

This Hamiltonian is composed of two symmetries: one is the global $U(1)$ symmetry, while the other is the modular symmetry with respect to the set $(-\pi, \pi]$ (with respect to each spin difference). An XY-type spin model is any two-dimensional ferromagnetic model that possesses these two symmetries.

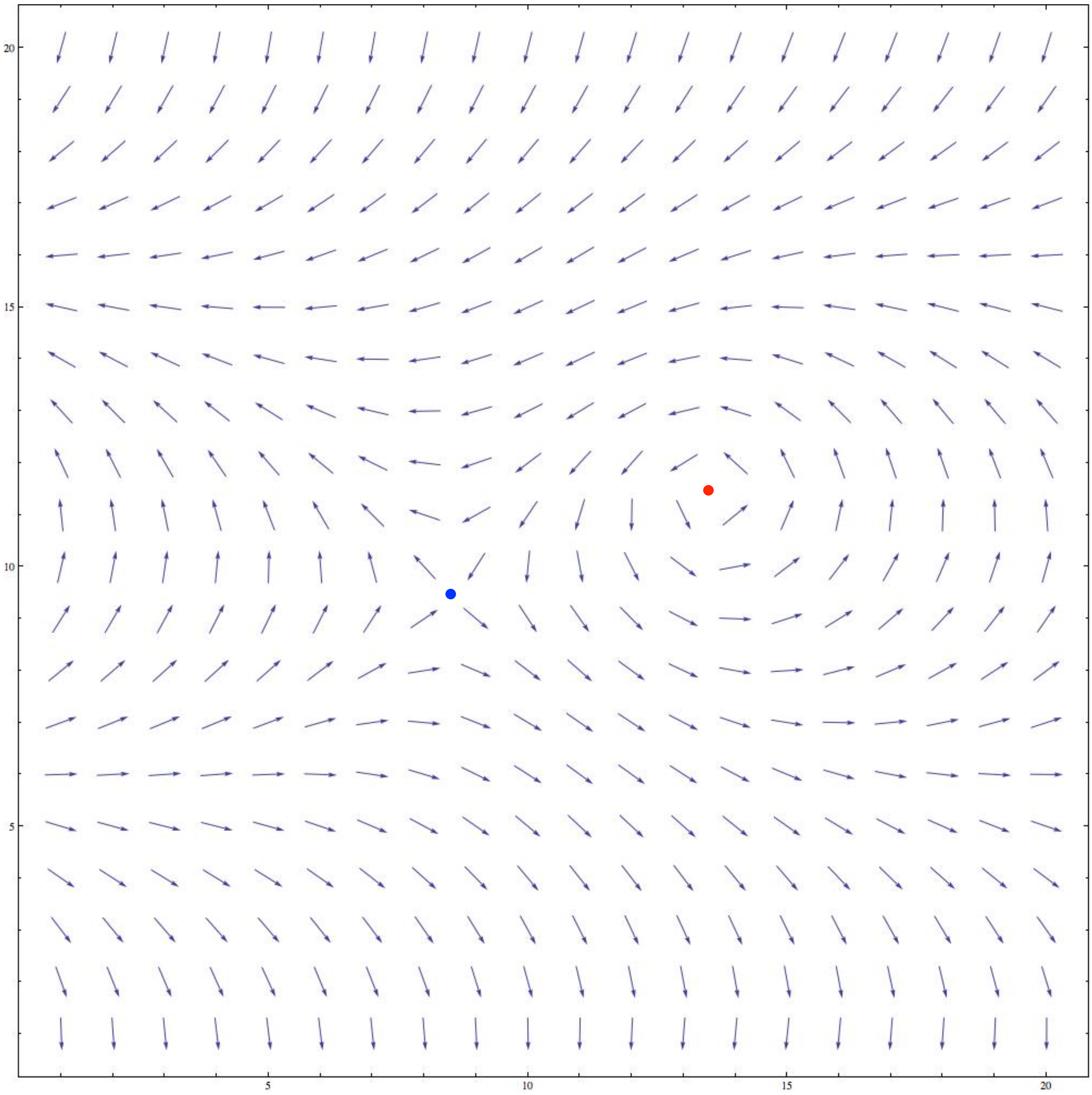

FIGURE 2.3: An example of an XY spin configuration. This configuration contains one pair of topological defects, or vortices. The red circle is the positive vortex; the blue circle is the negative vortex.

Fig. 2.3 shows a snapshot of a 20×20 XY model magnet. This particular spin configuration contains a vortex – antivortex pair. Vortices are topological defects in the spin-difference field and approximately behave as two-dimensional Coulombic charges. In Chapter 6, we will present an emergent electric field description of XY-type spin models in which the topological defects are emergent electric charges and the spin-wave fluctuations are emergent auxiliary-field fluctuations.

2.3.2 Continuum Approximation

To see the basis of the emergent electric charges, the continuum limit of the Taylor expansion of the Hamiltonian up to second order is considered, ignoring the constant zeroth order term. This system is described by the continuum, harmonic XY Hamiltonian:

$$H_{\text{Cont.}} = \frac{J}{2} \int_{\Omega} d^2x \left| \boldsymbol{\nabla}\theta(\mathbf{x}) \right|^2 , \tag{2.63}$$

where the gradient of the spin field $\boldsymbol{\nabla}\theta$ is subject to the constraint

$$\boldsymbol{\nabla}\theta(\mathbf{x}) \in (-\pi,\, \pi] \tag{2.64}$$

in order to take account of the modular symmetry of the real (lattice) Hamiltonian.

The integral of $\boldsymbol{\nabla}\theta$ around any closed contour $\partial\Gamma$ is given by $2\pi p$:

$$\oint_{\partial\Gamma} \boldsymbol{\nabla}\theta(\mathbf{x}) \cdot d\mathbf{l}(\mathbf{x}) = 2\pi p \tag{2.65}$$

where $p = 0,\, \pm 1$. Closed contours that return values of $p = \pm 1$ contain vortices: in Fig. 2.3, the right-hand vortex (red circle) has $p = 1$ and the left-hand vortex (blue circle) has $p = -1$ (for contours that only enclose the vortex in question). Ignoring spin-wave fluctuations, it follows that the energy of an isolated vortex in this continuum formulation is given by

$$\begin{aligned} E_{\text{Vort.}} =& \frac{J}{2} \int_0^{2\pi} \int_{r_0}^{L} \left| \frac{p}{r} \right|^2 r dr d\phi \\ =& \pi J \int_{r_0}^{L} \frac{dr}{r} \\ =& \pi J \ln\left(\frac{L}{r_0} \right) , \end{aligned} \tag{2.66}$$

where $r_0 := ae^{-\gamma}/2\sqrt{2}$ is now the UV lattice cut-off, representing an effective radius of the vortices. This shows that the energy of an isolated vortex diverges logarithmically with the size of the system. The entropy associated with an isolated vortex, however, is given by

$$S_{\text{Vort.}} = k_{\text{B}} \ln\left(N\right) , \tag{2.67}$$

where N is the number of lattice sites (N will also be the number of charge-lattice sites of the lattice Coulomb gas). It follows that the free energy associated with an isolated vortex diverges negatively with the system size at temperatures above [2, 3]

$$\bar{T}_{\text{BKT}} = \frac{\pi J}{2k_{\text{B}}}, \tag{2.68}$$

the non-screened BKT transition temperature for the system. In the thermodynamic limit, an isolated vortex is equivalent to a neutral pair of deconfined vortices, from which it follows that the continuum, harmonic XY model also admits a BKT transition. As explained in Section 2.1.2.2, this bare, non-screened BKT transition temperature for the continuum, harmonic XY model is reduced through screening corrections. In Chapter 6, we will see that Villain's approximation to the XY model [23] maps on to the lattice Coulomb gas with a vacuum permittivity given by the inverse exchange constant, hence the equivalence of this bare transition temperature and that derived in Section 2.1.2.2.

Throughout the remainder of this thesis, we set $J = 1$, but we may write this quantity explicitly to help the reader in identifying units.

2.3.3 The Villain Model

Villain introduced the Villain model [23] to approximate the XY model with an analytically tractable partition function. José *et al.* provide a useful discussion on the validity of the approximation [4]. The model uses a set of modular variables $\{s(\mathbf{x}, \mathbf{x}') \in \mathbb{Z}\}$, which exist between each lattice site, to mimic the modular symmetry of the XY model. Its partition function is given by

$$Z_{\text{Villain}} = \sum_{\{s(\mathbf{x},\mathbf{x}')\in\mathbb{Z}\}} \int \bar{\mathcal{D}}\varphi \exp\left[-\frac{\beta J}{2} \sum_{\langle \mathbf{x},\mathbf{x}' \rangle} |\varphi(\mathbf{x}) - \varphi(\mathbf{x}') + 2\pi s(\mathbf{x},\mathbf{x}')|^2 \right], \tag{2.69}$$

where the functional integral $\int \bar{\mathcal{D}}\varphi$ is defined via

$$\int \bar{\mathcal{D}}\varphi := \prod_{\mathbf{x}\in D'} \left[\int_{-\pi}^{\pi} d\varphi(\mathbf{x}) \right], \tag{2.70}$$

and D' is the set of all spin lattice sites. In this model, the modular s variables are not defined by the spin variables φ: topological defects are therefore not topological defects in the spin-difference field, in contrast with the XY model. In Chapter 6, however, we will see that the topological defects are topological defects in the emergent electric field. The Villain model is also used to model the physics of superfluid films [9–12], where the spin variables φ become the phase of the condensate wavefunction: when the phases at all sites are correlated, the system is in its superfluid state in which it behaves as one body.

2.3.4 The 2dHXY Model

The harmonic XY (HXY) model is a model of two-dimensional magnetism that is very similar to the Villain model. Its modular variables, however, are now functions of the spin variables, rather than an independently sampled set. This offers a closely related but much simplified algorithm. Its partition function is given by Eq. (2.69) without the sum over the set $\{s\}$. In the HXY model, the s variables are defined via the associated spin difference: $s(\mathbf{x}, \mathbf{x}') \in \{0, \pm 1\}$ is chosen such that $\varphi(\mathbf{x}) - \varphi(\mathbf{x}') + 2\pi s(\mathbf{x}, \mathbf{x}') \in (-\pi, \pi]$. This instills the modular symmetry required in XY-type spin models, but the spin variables now define the modular variables. It follows that the topological defects of this model are topological defects in both the spin-difference and emergent fields. As in the XY model, we refer to these topological defects as vortices, because they are topological defects in the spin-difference field of the model.

2.3.5 Spin-wave Magnetization

In this subsection, the spin-wave analysis of the magnetization of the Villain model [36] is reviewed. Spin-wave analysis amounts to ignoring the modular term in the partition function of the Villain model: this removes all topological defects from the system, thereby disallowing the BKT transition. This analysis will help us to understand the effect of topological defects and the BKT transition on XY-type spin models. The Villain model with the modular symmetry removed is referred to as the harmonic model.

2.3.5.1 Instantaneous Magnetization: Definition

To begin, the average instantaneous magnetization direction $\bar{\varphi}$ is defined by

$$\bar{\varphi} := \frac{1}{N} \sum_{\mathbf{x} \in D'} \varphi(\mathbf{x}), \tag{2.71}$$

where the instantaneous magnetization m is defined via

$$m := \frac{1}{N} \sum_{\mathbf{x} \in D'} \cos(\varphi(\mathbf{x}) - \bar{\varphi}). \tag{2.72}$$

The field $\psi(\mathbf{x}) := \varphi(\mathbf{x}) - \bar{\varphi}$ is defined to be the deviation from the average instantaneous magnetization at each spin site. As shown in Appendix B, the magnetization is related to ψ by [37]

$$\langle m \rangle = \exp\left[\left(-\frac{1}{2}\langle \psi^2(\mathbf{0}) \rangle\right)\right]. \tag{2.73}$$

2.3.5.2 Spin-spin Correlation Functions

In order to proceed from the above equation, we must find an expression for the spin-spin correlation function $\langle\varphi(\mathbf{x})\varphi(\mathbf{x}')\rangle$, which describes the correlations between the spins at spin sites $\mathbf{x}$ and $\mathbf{x}'$. The partition function of the harmonic model is given by

$$Z_{\mathrm{SW}} = \int \bar{\mathcal{D}}\varphi \exp\left(-\beta H_{\mathrm{SW}}\right), \tag{2.74}$$

where

$$H_{\mathrm{SW}} := \frac{J}{2} \sum_{\langle \mathbf{x},\mathbf{x}'\rangle} (\varphi(\mathbf{x}) - \varphi(\mathbf{x}'))^2 \tag{2.75}$$

is the harmonic (spin-wave) Hamiltonian.

We define the Fourier-transform pair

$$\varphi(\mathbf{x}) := \frac{1}{N} \sum_{\mathbf{k}\in B} e^{i\mathbf{k}\cdot\mathbf{x}}\phi(\mathbf{k});\ \phi(\mathbf{k}) := \sum_{\mathbf{x}\in D'} e^{-i\mathbf{k}\cdot\mathbf{x}}\varphi(\mathbf{x}), \tag{2.76}$$

and consider

$$(\varphi(\mathbf{x}) - \varphi(\mathbf{x}'))^2 = \frac{1}{N^2} \sum_{\mathbf{k},\mathbf{k}'\in B} e^{i\mathbf{k}\cdot\mathbf{x}} e^{i\mathbf{k}'\cdot\mathbf{x}} (1 - e^{-i\mathbf{k}\cdot(\mathbf{x}-\mathbf{x}')})(1 - e^{-i\mathbf{k}'\cdot(\mathbf{x}-\mathbf{x}')})\phi(\mathbf{k})\phi(\mathbf{k}'), \tag{2.77}$$

where the sum $\sum_{\mathbf{k}\in B} := \prod_{\mu\in\{x,y\}} \left[\sum_{k_\mu\in B_\mu}\right]$, and $B_\mu := \{0, \pm\frac{2\pi}{N_\mu a}, \pm 2\frac{2\pi}{N_\mu a}, \cdots, \pm(\frac{N_\mu}{2} - 1)\frac{2\pi}{N_\mu a}, \frac{N_\mu}{2}\frac{2\pi}{N_\mu a}\}$ is the set of $\mathbf{k}$-space values in the μ direction. Note that the sum over nearest neighbours is given by

$$\sum_{\langle \mathbf{x},\mathbf{x}'\rangle} \equiv \sum_{\boldsymbol{\delta}\in NN_{\mathbf{x}}} \sum_{\mathbf{x}\in D'}, \tag{2.78}$$

where the set $NN_{\mathbf{x}} := \{\mathbf{x} + a\mathbf{e}_x, \mathbf{x} + a\mathbf{e}_y\}$ is the set of the nearest neighbours of $\mathbf{x}$ in the positive directions. It follows that

$$\sum_{\langle \mathbf{x},\mathbf{x}'\rangle} (\varphi(\mathbf{x}) - \varphi(\mathbf{x}'))^2 = \frac{1}{N^2} \sum_{\boldsymbol{\delta}\in NN_{\mathbf{x}}} \sum_{\mathbf{k},\mathbf{k}'\in B} (1 - e^{i\mathbf{k}\cdot\boldsymbol{\delta}})(1 - e^{i\mathbf{k}'\cdot\boldsymbol{\delta}}) \sum_{\mathbf{x}} e^{i(\mathbf{k}+\mathbf{k}')\cdot\mathbf{x}}\phi(\mathbf{k})\phi(\mathbf{k}') \tag{2.79}$$

$$= \frac{1}{N} \sum_{\boldsymbol{\delta}\in NN_{\mathbf{x}}} \sum_{\mathbf{k}\in B} (1 - e^{i\mathbf{k}\cdot\boldsymbol{\delta}})(1 - e^{-i\mathbf{k}\cdot\boldsymbol{\delta}})\phi(\mathbf{k})\phi(-\mathbf{k}) \tag{2.80}$$

$$= \frac{1}{N} \sum_{\mathbf{k}\in B} \sum_{\boldsymbol{\delta}} (2 - e^{i\mathbf{k}\cdot\boldsymbol{\delta}} - e^{-i\mathbf{k}\cdot\boldsymbol{\delta}})|\phi(\mathbf{k})|^2 \tag{2.81}$$

$$= \sum_{\mathbf{k}\in B} \tilde{\gamma}_{\mathbf{k}} |\phi(\mathbf{k})|^2, \tag{2.82}$$

where

$$\tilde{\gamma}_{\mathbf{k}} := \frac{2}{N}(2 - \cos(k_x a) - \cos(k_y a)). \tag{2.83}$$

Hence,

$$\beta H_{\mathrm{SW}} = \frac{\beta J}{2} \sum_{\mathbf{x},\mathbf{x}' \in D'} \varphi(\mathbf{x}) \tilde{G}(\mathbf{x},\mathbf{x}') \varphi(\mathbf{x}'), \tag{2.84}$$

where

$$\tilde{G}(\mathbf{x},\mathbf{x}') := \sum_{\mathbf{k} \in B} \tilde{\gamma}_{\mathbf{k}} e^{-i\mathbf{k}\cdot(\mathbf{x}-\mathbf{x}')} \tag{2.85}$$

is the spin-wave propagator. This leaves us with a Hamiltonian that goes like a double summation over the whole lattice, rather than a sum over nearest-neighbour lattice sites.

For ease of notation, we define the spin column vector $\boldsymbol{\varphi}$,

$$\boldsymbol{\varphi} := \begin{pmatrix} \varphi(\mathbf{x}_1) \\ \vdots \\ \varphi(\mathbf{x}_N) \end{pmatrix}, \tag{2.86}$$

and the spin-wave propagator matrix $\mathbf{A}$,

$$\mathbf{A} := \beta J \begin{pmatrix} \tilde{G}(\mathbf{x}_1,\mathbf{x}_1) & \dots & \tilde{G}(\mathbf{x}_1,\mathbf{x}_N) \\ \vdots & \ddots & \vdots \\ \tilde{G}(\mathbf{x}_N,\mathbf{x}_1) & \dots & \tilde{G}(\mathbf{x}_N,\mathbf{x}_N) \end{pmatrix}. \tag{2.87}$$

The partition function is now given by

$$Z_{\mathrm{SW}} = \int \mathcal{D}\varphi \exp\left(-\frac{1}{2}\boldsymbol{\varphi}^T \mathbf{A} \boldsymbol{\varphi}\right). \tag{2.88}$$

We can now write the spin-wave thermal average of some scalar function of the spin variables $f(\boldsymbol{\varphi})$ as

$$\langle f(\boldsymbol{\varphi}) \rangle_{\mathrm{SW}} := \frac{1}{Z_{\mathrm{SW}}} \int \bar{\mathcal{D}}\varphi f(\boldsymbol{\varphi}) \exp\left(-\beta H_{\mathrm{SW}}\right) \tag{2.89}$$

$$= \frac{1}{Z_{\mathrm{SW}}} \int \bar{\mathcal{D}}\varphi f(\boldsymbol{\varphi}) \exp\left(-\frac{1}{2}\boldsymbol{\varphi}^T \mathbf{A} \boldsymbol{\varphi}\right) \tag{2.90}$$

$$= \frac{1}{Z_{\mathrm{SW}}} \int \bar{\mathcal{D}}\varphi f\left(-\frac{\delta}{\delta \mathbf{b}}\right) \exp\left(-\frac{1}{2}\boldsymbol{\varphi}^T \mathbf{A} \boldsymbol{\varphi} - \mathbf{b}^T \boldsymbol{\varphi}\right)\bigg|_{\mathbf{b}=\mathbf{0}} \tag{2.91}$$

$$= \frac{1}{Z_{\mathrm{SW}}} f\left(-\frac{\delta}{\delta \mathbf{b}}\right) \int \bar{\mathcal{D}}\varphi \exp\left(-\frac{1}{2}\boldsymbol{\varphi}^T \mathbf{A} \boldsymbol{\varphi} - \mathbf{b}^T \boldsymbol{\varphi}\right)\bigg|_{\mathbf{b}=\mathbf{0}} \tag{2.92}$$

$$=\frac{(2\pi)^{N/2}}{Z_{\mathrm{SW}}\sqrt{\det\mathbf{A}}}\, f\left(-\frac{\delta}{\delta\mathbf{b}}\right)\exp\left(\frac{1}{2}\mathbf{b}^T\mathbf{A}^{-1}\mathbf{b}\right)\Bigg|_{\mathbf{b}=\mathbf{0}}, \tag{2.93}$$

which we combine with the definition $\partial_i := \partial/\partial b_i$ to write

$$\langle\varphi_\mu\varphi_\nu\rangle_{\mathrm{SW}} = \frac{(2\pi)^{N/2}}{Z_{\mathrm{SW}}\sqrt{\det\mathbf{A}}}\,\partial_\mu\partial_\nu\exp\left(\frac{1}{2}b_\alpha A^{-1}_{\alpha\beta}b_\beta\right)\Bigg|_{\mathbf{b}=\mathbf{0}}, \tag{2.94}$$

where repeated Greek indices are summed over. We compute the derivatives:

$$\partial_\mu\partial_\nu\exp\left(\frac{1}{2}b_\alpha A^{-1}_{\alpha\beta}b_\beta\right)\Bigg|_{\mathbf{b}=\mathbf{0}} = \frac{1}{2}\left(A^{-1}_{\mu\nu}+A^{-1}_{\nu\mu}\right)\exp\left(\frac{1}{2}b_\rho A^{-1}_{\rho\sigma}b_\sigma\right)\Bigg|_{\mathbf{b}=\mathbf{0}}. \tag{2.95}$$

It follows that

$$\langle\varphi^2(\mathbf{0})\rangle_{\mathrm{SW}} = A^{-1}_{00}. \tag{2.96}$$

2.3.5.3 The Inverse Propagator

To compute the spin-wave magnetization (the magnetization of the harmonic model), we must now find an expression for the inverse propagator $\mathbf{A}^{-1}_{ij}$. We require that

$$\left[\mathbf{A}^{-1}\mathbf{A}\right]_{ij} = \delta_{ij}, \tag{2.97}$$

which is solved by

$$A^{-1}_{ij} = \frac{1}{\beta J}\sum_{\mathbf{k}\in B}\gamma_{\mathbf{k}}e^{i\mathbf{k}\cdot(\mathbf{x}_i-\mathbf{x}_j)}, \tag{2.98}$$

where

$$\gamma_{\mathbf{k}} := \frac{1}{2N(2-\cos(k_x a)-\cos(k_y a))}, \tag{2.99}$$

and $\gamma_{\mathbf{k}=\mathbf{0}} \in \mathbb{R}$ which we choose to be zero (this is known to be valid from simulation [19, 20]). We are left with

$$A^{-1}_{ij} = \frac{1}{\beta J}\sum_{\mathbf{k}\neq\mathbf{0}}\frac{e^{i\mathbf{k}\cdot(\mathbf{x}_i-\mathbf{x}_j)}}{2N(2-\cos(k_x a)-\cos(k_y a))}, \tag{2.100}$$

and we may now write

$$\langle\varphi^2(\mathbf{0})\rangle_{\mathrm{SW}} = \frac{1}{K}G(\mathbf{0}) \tag{2.101}$$

where $K := \beta J$ is the spin stiffness, G is the Green's functions of the two-dimensional lattice Coulomb gas,

$$G(\mathbf{x}, \mathbf{x}') = \frac{1}{2N} \sum_{\mathbf{k} \neq \mathbf{0}} \frac{e^{i\mathbf{k}\cdot(\mathbf{x}-\mathbf{x}')}}{2 - \cos(k_x a) - \cos(k_y a)}, \tag{2.102}$$

and

$$G(\mathbf{x}) := G(\mathbf{x}, \mathbf{0}). \tag{2.103}$$

2.3.5.4 Instantaneous Magnetization: Final Expression

To convert this working to the expression for the spin-wave magnetization, we must now compute the quantity

$$\langle \psi(\mathbf{x})\psi(\mathbf{x}')\rangle = \langle \varphi(\mathbf{x})\varphi(\mathbf{x}')\rangle - \langle \varphi(\mathbf{x})\bar{\varphi}\rangle - \langle \varphi(\mathbf{x}')\bar{\varphi}\rangle + \langle \bar{\varphi}\bar{\varphi}\rangle. \tag{2.104}$$

As shown in Appendix B, the final three terms of the above expression are zero, hence

$$\langle \psi(\mathbf{x})\psi(\mathbf{x}')\rangle = \langle \varphi(\mathbf{x})\varphi(\mathbf{x}')\rangle. \tag{2.105}$$

Using the Abel-Plana formula,

$$G(\mathbf{0}) = \frac{1}{4\pi} \ln(cN), \tag{2.106}$$

hence,

$$\langle \psi^2(\mathbf{0})\rangle_{\mathrm{SW}} = \frac{1}{4\pi K} \ln(cN), \tag{2.107}$$

and the spin-wave magnetization is therefore given by [37]

$$\langle m\rangle_{\mathrm{SW}} = \left(\frac{1}{cN}\right)^{1/8\pi K}. \tag{2.108}$$

Eq. (2.108) describes the magnetization for a planar ferromagnet that comprises of N harmonically coupled spins: this is known as the spin-wave magnetization of a general planar ferromagnet with XY symmetry. At finite temperatures ($T \neq 0$), this object is zero in the thermodynamic limit: XY-type spin models cannot sustain long-range order in the thermodynamic limit, even in the absence of topological defects [25]. The magnetization of the finite-size system is, however, known to be both measurable [21] and extremely important to the critical theory of the system [19, 20]. This is due to Eq. (2.108) approaching the thermodynamic limit so slowly that a ferromagnetic film the size of the state of Texas would have a finite-size magnetization [19]. In the above working, $c = 1.8456$.

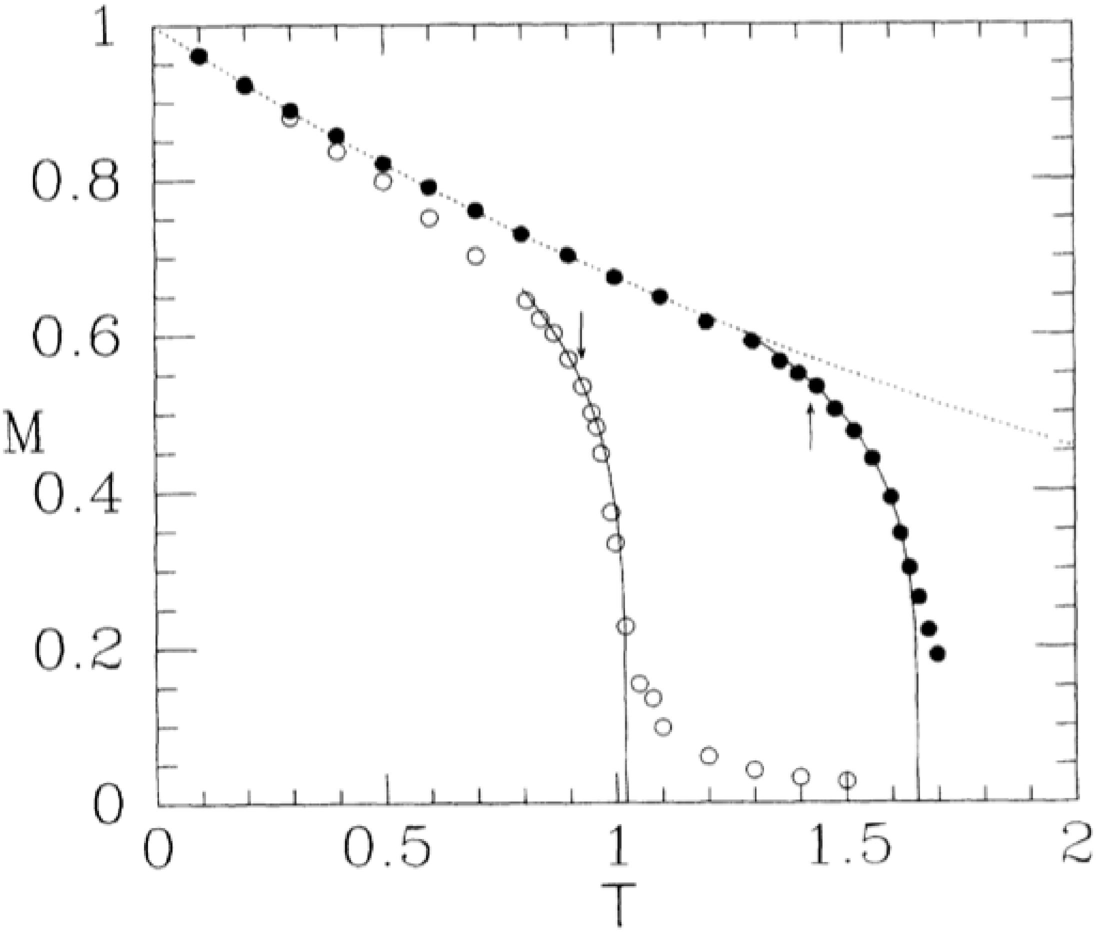

FIGURE 2.4: (Ref. [20]) The magnetization of the HXY (filled circles) and XY (empty circles) models for square lattices of 10^4 spins. The dashed curve is the spin-wave magnetization of Eq. (2.108). The deviation from the spin-wave magnetization for the HXY model is due to the appearance of topological defects: this is unsurprising, since the Villain and HXY models are equivalent when topological defects are not present. The XY data deviates at a lower temperature where topological defects are not present: this is due to the anharmonic terms in the cosine potential suppressing the magnetization. The arrows represent the transition temperature outlined in Section 2.5.2. The solid line represents the BH scaling of each system, as outlined in Section 2.5.

Fig. 2.4 shows the magnetization of XY and HXY models of 10^4 spins with the spin-wave magnetization curve superimposed. Both data sets show that the finite-size system can sustain long-range order, and also agree with the spin-wave magnetization at low temperature. The deviation from the spin-wave magnetization for the HXY model is due to the appearance of topological defects and the BKT transition: this is unsurprising, since the Villain and HXY models are equivalent when topological defects are not present. The XY data deviates at a lower temperature at which topological defects are not present because the anharmonic terms in the cosine potential suppress the magnetization.

2.3.6 Helicity Moduli

In the XY and HXY models, the helicity modulus Υ is proportional to the second derivative of the free energy F of the system with respect to the longest-wavelength twist possible in either component of the spin field, with the twist length taken continuously to infinity. The helicity modulus therefore measures the response of the system in question to the long-wavelength twist being externally applied. The twist is equivalent to adding

$$k_0 := \frac{2\pi a}{L}, \tag{2.109}$$

to each nearest-neighbour spin difference, where L is the linear system size: taking the twist length to infinity is therefore equivalent to taking the thermodynamic limit.

The helicity modulus of the Villain model is not measured with a twist, since the modular variables are not defined by the spin variables. Here, k_0 is just added to each $\varphi(\mathbf{x}) - \varphi(\mathbf{x}') + 2\pi s(\mathbf{x}, \mathbf{x}')$ in Eq. (2.69). In fact, the helicity modulus of each XY-type spin model is equivalent to performing this perturbation, but the mechanics of the HXY and XY models means that this perturbation is controlled by a twist in the spin field. This will be outlined in detail in Chapter 6.

For the general XY-type spin model, the helicity modulus is defined by

$$\Upsilon(T) := \frac{1}{N} \left. \frac{\partial^2 F(A, T, k_0)}{\partial k_0^2} \right|_{k_0 \to 0}, \tag{2.110}$$

where $F(A, T, k_0)$ is the free energy of the system under the influence of the perturbation k_0. Since taking the twist length to infinity (in the XY and HXY models) is equivalent to taking the thermodynamic limit, this measure is only truly defined in the thermodynamic limit. The resultant helicity modulus, however, turns out to be measurable in finite-size systems, so we introduce the finite-size helicity modulus $\tilde{\Upsilon}$, which is a function of both system size and temperature.

Following analogous working to that presented in Section 3.4, it follows that the finite-size helicity modulus of the XY model is given by

$$\tilde{\Upsilon}(N, T) = \langle e \rangle - N\beta \langle j^2 \rangle, \tag{2.111}$$

where

$$e := \frac{J}{N} \sum_{\langle \mathbf{x}, \mathbf{x}' \rangle_i} \cos(\varphi(\mathbf{x}) - \varphi(\mathbf{x}')), \tag{2.112}$$

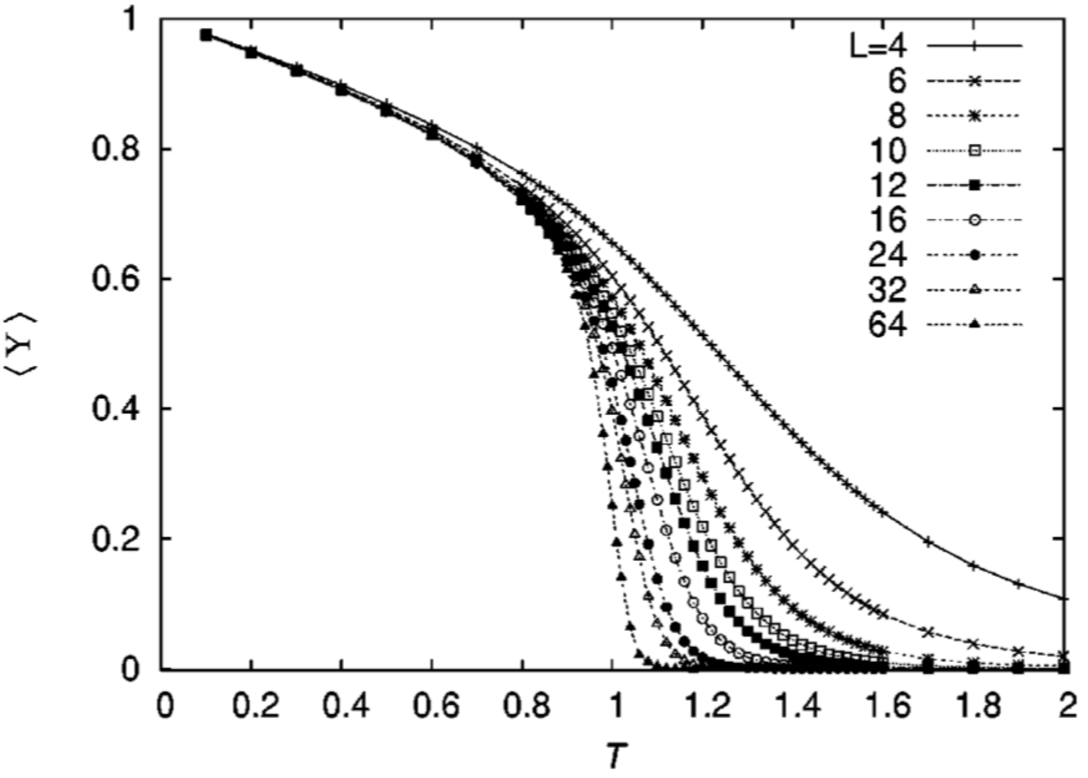

FIGURE 2.5: (Ref. [38]) The finite-size helicity modulus $\tilde{\Upsilon}$ of the two-dimensional XY model as a function of T for various system sizes. The helicity modulus is clearly tending towards zero in the high-temperature phase and to a finite value in the low-temperature phase.

and

$$j := \frac{J}{N} \sum_{\langle \mathbf{x},\mathbf{x}' \rangle_i} \sin(\varphi(\mathbf{x}) - \varphi(\mathbf{x}')), \tag{2.113}$$

with $\sum_{\langle \mathbf{x},\mathbf{x}' \rangle_i}$ denoting a sum over nearest-neighbour spins in the i direction.

Similarly, for the HXY and Villain models, the finite-size helicity modulus is given by

$$\tilde{\Upsilon}(N,T) = J \left(1 - \frac{\beta J}{N} \langle \left[\sum_{\langle \mathbf{x},\mathbf{x}' \rangle_i} \left(\varphi(\mathbf{x}) - \varphi(\mathbf{x}') + 2\pi s(\mathbf{x},\mathbf{x}') \right) \right]^2 \rangle \right). \tag{2.114}$$

Minnhagen and Kim [38] performed extensive Monte Carlo simulations of the XY model and measured the helicity modulus for systems of linear size $L = 4$ to 64, as shown in Fig. 2.5. As seen in the figure, increasing system size shows that this quantity is zero in the high-temperature phase, above the BKT transition. Note that a phase is only defined in the thermodynamic limit.

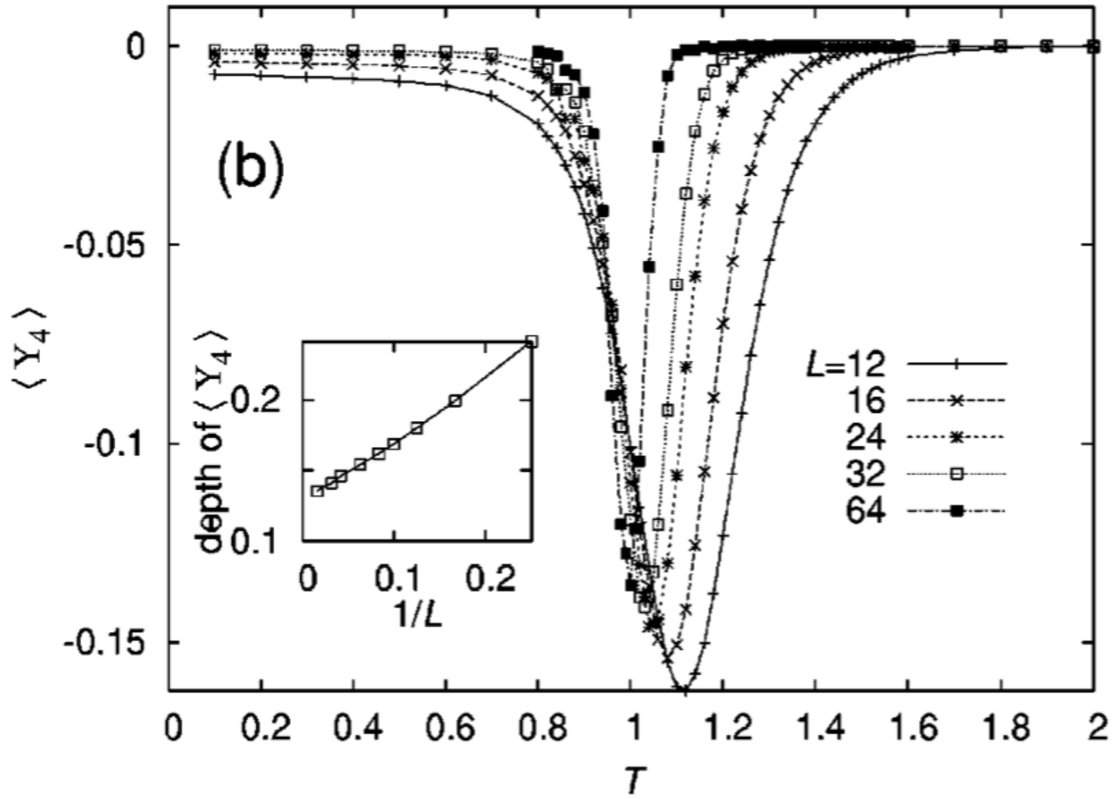

FIGURE 2.6: (Ref. [38]) The finite-size fourth-order cumulant $\tilde{\Upsilon}_4$ of the two-dimensional XY model as a function of T for various system sizes. As system size increases, the centres of the wells of the curves move closer to $T = T_{\text{BKT}}$ (where T_{BKT} is the renormalized BKT transition temperature for the system): a finite-size scaling of the data (shown in the inset) reveals a well of finite depth in the thermodynamic limit. A combination of a well of finite depth and a zero-valued helicity modulus Υ at T_{BKT} is reconciled by a discontinuous jump to zero in the helicity modulus at T_{BKT}.

In order to model the deviation of an XY-type spin stiffness from harmonic spin-wave behaviour, one can define the effective partition function:

$$Z_{\text{eff.}}(L,T) := \int \bar{\mathcal{D}}\varphi \exp\left[-\frac{\tilde{K}_{\text{eff.}}(L,T)}{2}\sum_{\langle \mathbf{x},\mathbf{x}'\rangle}\left(\varphi(\mathbf{x})-\varphi(\mathbf{x}')\right)^2\right]. \tag{2.115}$$

This is the harmonic partition function with the spin stiffness K replaced with the finite-size effective spin stiffness $\tilde{K}_{\text{eff.}}$. Upon identifying the partition function of the XY-type spin model in question with $Z_{\text{eff.}}$, it follows that $(\tilde{K}_{\text{eff.}}(L,T) - K(T))$ then has the effect of measuring the deviation of the system in question from harmonic spin-wave behaviour. $\tilde{K}_{\text{eff.}}$ therefore takes on the role of the finite-size effective spin stiffness and it follows that

$$\frac{\beta}{N}\left.\frac{\partial^2 F(A,T,k_0)}{\partial^2 k_0}\right|_{k_0\to 0} = \lim_{L\to\infty}\left[\tilde{K}_{\text{eff.}}(L,T)\right] =: K_{\text{eff.}}(T), \tag{2.116}$$

where $K_{\text{eff.}}$ is the thermodynamic limit of the effective spin stiffness, which is the effective spin stiffness that is standard in the literature (since the majority of the literature on XY-type spin models is in the thermodynamic limit). Combining Eqs. (2.110) and (2.116), one finds that the effective spin stiffness is closely related to the helicity modulus in the thermodynamic limit:

$$K_{\text{eff.}}(T) = \beta\Upsilon(T). \tag{2.117}$$

In the thermodynamic limit, all systems are predicted to experience a universal jump in their effective spin stiffness (and therefore in their helicity moduli) as they pass through their BKT transition temperatures from below [2–4, 22, 38, 39]: at these transition temperatures, the effective spin stiffness of each system jumps discontinuously from $2/\pi$ to zero [4, 22, 38, 39]. The significance of the value $2/\pi$ will become clear in Section 3.32.

The universal jump is consistent with the data in Fig. 2.5 that shows that the helicity modulus is finite in the low-temperature phase of the BKT transition and zero in the high-temperature phase. To confirm the discontinuous nature of the universal jump, Minnhagen and Kim [38] performed a finite-size scaling analysis on the higher-order cumulant Υ_4, defined by

$$\Upsilon_4(T) := \frac{1}{N^2}\,\frac{\partial^4 F(A,T,k_0)}{\partial^4 k_0}\bigg|_{k_0\to 0} \tag{2.118}$$

in the thermodynamic limit. It is again generalized to the finite-size system by introducing the finite-size cumulant $\tilde{\Upsilon}_4$.

Minnhagen and Kim [38] use the argument that for a system with a finite twist the free energy of the system can be written as an expansion in small k_0:

$$F(L,T,k_0) = \tilde{\Upsilon}(L,T)\,\frac{k_0^2}{2!} + \tilde{\Upsilon}_4(L,T)\,\frac{k_0^4}{4!} + \ldots, \tag{2.119}$$

and that $F(L,T,k_0 = 0) \leq F(L,T,k_0)$. This means that $\Upsilon \geq 0$ because the lowest-order non-vanishing derivative of the free energy will always dominate for small enough k_0. It also implies that, for the helicity modulus to be continuous everywhere, the next-order derivative Υ_4 has to be ≥ 0 at any T where $\Upsilon(T) = 0$. Their argument was then the observation that Υ cannot continuously tend to zero at the transition temperature T_{BKT} if Υ_4 simultaneously approaches a non-zero negative value at T_{BKT}. But, since Υ is zero in the high-temperature phase, this means that, if $\tilde{\Upsilon}_4$ approaches a negative value at T_{BKT} in the thermodynamic limit, then the jump has to be discontinuous.

The depth of the well in Fig. 2.6 scales to a finite value in the thermodynamic limit, implying that Υ_4 takes a non-zero negative value at $T = T_{\text{BKT}}$, and hence that Υ experiences a discontinuous jump at the BKT transition temperature T_{BKT}. This discontinuous jump is a signature of BKT physics.

2.4 The Berezinskii-Kosterlitz-Thouless Transition

The destruction of the magnetization of the finite-size XY-type spin models shown in Fig. 2.4 is due to (the finite-size analogue of) the BKT phase transition. The BKT transition governs the thermal dissociation of topological-defect pairs that are bound together by a logarithmic interaction potential. As previously discussed, these pairs correspond to topological defects in the electric field of the two-dimensional Coulomb gas and to topological defects in the spin fields of the XY and HXY models of ferromagnetic films, along with defect pairs in many other condensed-matter systems. The background theory of the transition is provided here because the reader has now been presented with a couple of basic arguments regarding the existence of the transition.

BKT introduced the concept of quasi-long-range order and a phase transition in the two-dimensional XY model [2, 3]. Topological order corresponds to topological defects in the XY model being tightly bound in neutral pairs in the low-temperature phase of the transition by the diverging, logarithmic energy barrier presented in Section 2.3.2. As discussed in Section 2.1.2.2 in the context of the two-dimensional Coulomb gas, the phase transition is a result of entropy reducing the free-energy barrier to deconfined charge to a finite value.

Kosterlitz [39] and José *et al.* [4, 40] presented extensive renormalization group (RG) analysis of the two-dimensional XY model to show that XY-type spin models obey the RG equation for the renormalized spin stiffness K_{RG}:

$$K_{\mathrm{RG}}^{-1} = K^{-1} + 4\pi^2 y^2 \int_{r_0}^{\infty} \frac{dr}{r_0} \left(\frac{r}{r_0} \right)^{3-2\pi K_{\mathrm{RG}}} \tag{2.120}$$

in the thermodynamic limit and for $K_{\mathrm{RG}} > 2/\pi$, where $y := 4\pi K \tau^2$ and τ is the renormalized lattice spacing.

The above equation diverges as K_{RG} approaches $2/\pi$ from the low-temperature phase: this corresponds to the system reaching the topological-defect critical point, the point at which the spin-spin correlation length diverges with the system size (when approached from the high-temperature phase), and implies a universal jump from $2/\pi$ to zero.

The universal jump in K_{RG} is the same universal jump that occurs in the effective spin stiffness in the thermodynamic limit $K_{\mathrm{eff.}}$, hence the finite-size scaling analysis of Minnhagen and Kim [38] shows the RG analysis of Kosterlitz [39] and José *et al.* [4] to be correct.

Tobochnik and Chester [41] fitted BKT theory to their simulation data of the two-dimensional XY model to find the topological-defect critical point at $T_{\mathrm{BKT}}^{\mathrm{XY}} \simeq 0.89$. This was followed by the transfer-matrix approach of Mattis [42] who found that $T_{\mathrm{BKT}}^{\mathrm{XY}} \simeq 0.883$. Weber and Minnhagen [43] then performed a finite-size scaling analysis of the system to find that $T_{\mathrm{BKT}}^{\mathrm{XY}} = 0.887$ up to an error of the order of a tenth of a percent. This final value is taken to be the renormalized BKT transition temperature of the two-dimensional XY model and is the value used in the finite-size scaling analysis of Minnhagen and Kim [38].

A simulation of the Villain model was performed by Janke and Nather [29] to find that the renormalized BKT transition temperature of the Villain system is $T_{\mathrm{BKT}} \simeq 1.35$ (to three significant figures). This is also taken to be the BKT transition temperature for the HXY model due to their similarity at low topological-defect density. The Villain model allows the excitation of non-elementary topological defects: these defects, however, do not alter the transition temperature from that of the Villain model restricted to elementary defects, since the self energies of the non-elementary defects are large enough that the thermal average of their densities are negligibly low at $T = 1.35$.

Lapilli *et al.* [44] listed three criteria to which systems must adhere in order to be classified as BKT systems: (i) the universal jump in $\beta\Upsilon$ in the thermodynamic limit [9]; (ii) an exponentially diverging, high-temperature spin-spin correlation length: $\zeta \sim \exp\left(c'/|T - T_{\mathrm{BKT}}|^{1/2}\right)$ (where c' is a constant) [39]; (iii) exponents $\eta(T) = 1/2\pi K_{\mathrm{eff.}}(T) \to 1/4$ at $T = T_{\mathrm{BKT}}$ (from the low-temperature phase) [39] and $\tilde{\beta} = 3\pi^2/128$ at $T = T_{\mathrm{BKT}}$ [19] (the latter of which is an effective critical exponent, and is covered in the next section).

2.5 Bramwell-Holdsworth Theory

The spin-wave magnetization described by Eq. (2.108) approaches zero slowly as the system size approaches the thermodynamic limit, so that finite-size effects remain extremely important in surprisingly large systems, where the magnetization is known to be measurable [21]. As shown by Fig. 2.3, the introduction of topological defects to the system should affect this experimentally measurable finite-size magnetization.

Bramwell-Holdsworth (BH) theory applies the RG equations derived by Kosterlitz [39] for the XY model to the finite-size system to find a universal effective critical exponent at the topological-defect critical point (where the unbinding of topological defects drives the transition) for XY-type spin models. Clearly, this can only be achieved for systems of finite magnetization: this prediction and measurement is a key step towards the understanding of the importance of finite-size effects in magnetic films with XY symmetry. The exponent will be introduced once the basis of the theory has been outlined. We stress here that the exponent is perfectly well defined in the thermodynamic limit, which is taken once the finite-size analysis has been performed.

2.5.1 Renormalization Group Equations

Kosterlitz derived [39] the following RG equation for large lattice systems:

$$\frac{a_f}{a_i} = \exp\left[\frac{1}{\sqrt{c'(T - T_{\mathrm{BKT}})}}\left(\tan^{-1}\left(\frac{\sqrt{c'(T - T_{\mathrm{BKT}})}}{x_f}\right) - \tan^{-1}\left(\frac{\sqrt{c'(T - T_{\mathrm{BKT}})}}{x_i}\right)\right)\right], \tag{2.121}$$

where he used the continuum XY Hamiltonian, which is a good approximation to large lattice systems, and where c' is a constant, a_i and a_f are the initial and final values of the renormalized lattice spacing a, and x_i and x_f are the initial and final values of the renormalized deviation from $\pi K_{\mathrm{eff.}} - 2 = 0$, x, defined via

$$x := \pi K_{\mathrm{eff.}} - 2. \tag{2.122}$$

Here, BH use a measuring system in which T is measured in units of J/k_{B}, hence the $(T - T_{\mathrm{BKT}})/T_{\mathrm{BKT}}$ term that Kosterlitz [39] has in his RG equation becomes $T - T_{\mathrm{BKT}}$ in Eq. (2.121).

This RG flow is towards the point where $x = 0$, hence $x_i > x_f$. It follows that, for $a_f \gg a_i$ (topological-defect critical point),

$$\frac{a_f}{a_i} \simeq \exp\left[\frac{1}{\sqrt{c'(T - T_{\mathrm{BKT}})}}\tan^{-1}\left(\frac{\sqrt{c'(T - T_{\mathrm{BKT}})}}{x_f}\right)\right], \tag{2.123}$$

since the first term of Eq. (2.121) dominates. This corresponds to

$$x_f \simeq \frac{\sqrt{c'(T - T_{\mathrm{BKT}})}}{\tan\left(\sqrt{c'(T - T_{\mathrm{BKT}})}\ln(a_f/a_i)\right)} \tag{2.124}$$

near the topological-defect critical point.

2.5.2 Finite-size Transition Temperatures

In the thermodynamic limit, BKT systems undergo a transition at the BKT transition temperature T_{BKT}. In finite-size systems, however, the transition occurs over a temperature range of finite width that is bounded by the two finite-size transition temperatures of the

BKT transition. BH defined these temperatures to be $T^*(L)$ (lower bound) and $T_\mathrm{C}(L)$ (upper bound). The three transition temperatures then satisfy the double inequality,

$$T_\mathrm{BKT} \leq T^*(L) \leq T_\mathrm{C}(L), \tag{2.125}$$

where both inequalities become equalities in the thermodynamic limit.

The lower of the two finite-size transition temperatures $T^*(L)$ is the temperature at which the effective spin stiffness equals $2/\pi$, since this is equivalent to approaching the universal jump [4, 39] in the thermodynamic limit from below.

The RG equations used in the thermodynamic limit are for $x \geq 0$, which is equivalent to approaching the transition from below. $T^*(L)$ therefore has to correspond to the topological-defect critical point of the RG equations, or, equivalently, to the temperature at which $x_f = 0$ in Eq. (2.124). This cannot occur for a zero-valued numerator in Eq. (2.124) because this possibility has been cut off by the finite-size system. Hence,

$$0 \simeq \frac{\sqrt{c'(T^*(L) - T_\mathrm{BKT})}}{\tan\left(\sqrt{c'(T^*(L) - T_\mathrm{BKT})}\,\ln(k_1 L)\right)}, \tag{2.126}$$

where k_1 is a constant of order unity (introduced because $a_f/a_i \sim L$ for the finite-size system), can only correspond to a divergent denominator, which is satisfied by

$$\frac{\pi}{2} \simeq \sqrt{c'(T^*(L) - T_\mathrm{BKT})}\,\ln(k_1 L), \tag{2.127}$$

or, equivalently, by

$$T^*(L) \simeq T_\mathrm{BKT} + \frac{\pi^2}{4c' \ln^2(k_1 L)}. \tag{2.128}$$

The arrows on Fig. 2.4 mark $T^*(L)$ for the XY and HXY models consisting of 10^4 spins.

The higher of the two finite-size transition temperatures $T_\mathrm{C}(L)$ corresponds to the finite-size analogue of the temperature at which the transition into the high-temperature phase is complete. One would therefore assume that this corresponds to the lowest temperature at which $K_\mathrm{eff.} = 0$. BH, however, noted that a measure of $T_\mathrm{C}(L)$ via the correlation length of the system ζ is more suitable, since this allows the system size to be taken into account. BH therefore set $T_\mathrm{C}(L)$ to be the temperature at which the correlation length decreases to the linear system size (when $T_\mathrm{C}(L)$ is approached from below).

Kosterlitz defined the correlation length of the system ζ to be the smallest value of a_f/a_i at which there is a significant deviation from fixed-point behaviour in the RG equations. BH used this to set the correlation length ζ equal to a_f/a_i when the argument of the tangent in Eq. (2.124) is approximately π. It follows that

$$\zeta \simeq \exp\left(\frac{\pi}{\sqrt{c'(T - T_{\text{BKT}})}}\right). \tag{2.129}$$

BH then noted that the correlation length decreasing to the system size corresponds to $\zeta \sim L$, or to $\zeta = k_1 L$ (the constant k_1 of $T^*(L)$ appears here because Eq. (2.124) is used again: it is approximated to diverge in this case). Hence,

$$k_1 L \simeq \exp\left(\frac{\pi}{\sqrt{c'(T_{\text{C}}(L) - T_{\text{BKT}})}}\right), \tag{2.130}$$

which results in

$$T_{\text{C}}(L) \simeq T_{\text{BKT}} + \frac{\pi^2}{c' \ln^2(Lk_1)}. \tag{2.131}$$

Combining Eqs. (2.128) and (2.131), BH approximated the width of the transition temperature range to be

$$T_{\text{C}}(L) - T^*(L) \simeq \frac{3\pi^2}{4c' \ln^2(Lk_1)}. \tag{2.132}$$

2.5.3 The Critical Exponent

The effective critical exponent $\tilde{\beta}$ relates the reduced temperature $t := T_{\text{C}}(L) - T$ and the magnetization of the system near the critical point:

$$\langle m \rangle \sim t^{\tilde{\beta}} \tag{2.133}$$

in the vicinity of $T^*(L)$. It follows that

$$\tilde{\beta} = \frac{\partial \ln\langle m \rangle}{\partial \ln t} \tag{2.134}$$

in the vicinity of $T^*(L)$. It is this exponent for which BH found a universal law at $T = T^*(L)$: the law occurs away from the temperature from which the temperature T is reduced ($T_{\text{C}}(L)$).

BH then adapt the spin-wave magnetization given by Eq. (2.108) to make the following ansatz:

$$\langle m \rangle = \left(\frac{1}{cN}\right)^{1/8\pi K_{\text{eff.}}(T)} \tag{2.135}$$

for $T \leq T^*(L)$. Eq. (2.122) then leads us to

$$\tilde{\beta} = \ln(cN)\frac{t}{8(2+x)^2}\frac{\partial x}{\partial t}. \tag{2.136}$$

Near the topological-defect critical point, it follows that

$$\begin{aligned}\frac{\partial x}{\partial t} = &-\frac{1}{2}\sqrt{\frac{c'}{T - T_{\mathrm{BKT}}}}\frac{1}{\tan\left(\sqrt{c'(T-T_{\mathrm{BKT}})}\ln(k_1 L)\right)} \\ &+ \frac{c'}{2}\ln(k_1 L)\left(1 + \frac{1}{\tan^2\left(\sqrt{c'(T-T_{\mathrm{BKT}})}\ln(k_1 L)\right)}\right).\end{aligned} \tag{2.137}$$

The divergent denominator that leads to Eq. (2.128) also leads to

$$\left.\frac{\partial x}{\partial t}\right|_{T=T^*(L)} \simeq \frac{c'}{2}\ln(k_1 L). \tag{2.138}$$

Defining $\tilde{\beta}^* := \tilde{\beta}\Big|_{T=T^*(L)}$ to be the critical exponent at $T = T^*(L)$, it follows that

$$\begin{aligned}\tilde{\beta}^* &\simeq \ln(cN)\frac{T_{\mathrm{C}}(L) - T^*(L)}{8.\,2^2}\frac{c'}{2}\ln(k_1 L) && (2.139)\\ &= \frac{c'}{64}(T_{\mathrm{C}}(L) - T^*(L))\ln(cN)\ln(k_1 L) && (2.140)\\ &\simeq \frac{c'}{64}\frac{3\pi^2}{4c'\ln^2(k_1 L)}\ln(cN)\ln(k_1 L) && (2.141)\\ &= \frac{3\pi^2}{256}\frac{\ln(cN)}{\ln(k_1 L)} && (2.142)\\ &= \frac{3\pi^2}{128}\frac{\ln(k_2 L)}{\ln(k_1 L)} && (2.143)\\ &= \frac{3\pi^2}{128}\frac{1+\ln(k_2)/\ln(L)}{1+\ln(k_1)/\ln(L)}, && (2.144)\end{aligned}$$

where Eq. (2.132) is used in the third line, and $k_2 := \sqrt{c}$. In the thermodynamic limit, the effective critical exponent $\tilde{\beta}$ therefore takes a universal value at $T = T_{\mathrm{BKT}}$:

$$\tilde{\beta}^* = \frac{3\pi^2}{128}. \tag{2.145}$$

The thermodynamic limit taken here is perfectly well defined because the derivative of the finite-size magnetization is computed before the limit is taken.

The signature of BH theory given by Eq. (2.145) is expected to apply to large but finite-size systems (since $\ln(k_1), \ln(k_2) \ll \ln(L)$ for large L) [19]. BH numerically tested the application of their theory to finite-size systems: Fig. 2.7 shows $\log_{10}\langle m\rangle$ versus $\log_{10}(T_{\mathrm{C}}(L) - T)$ for XY

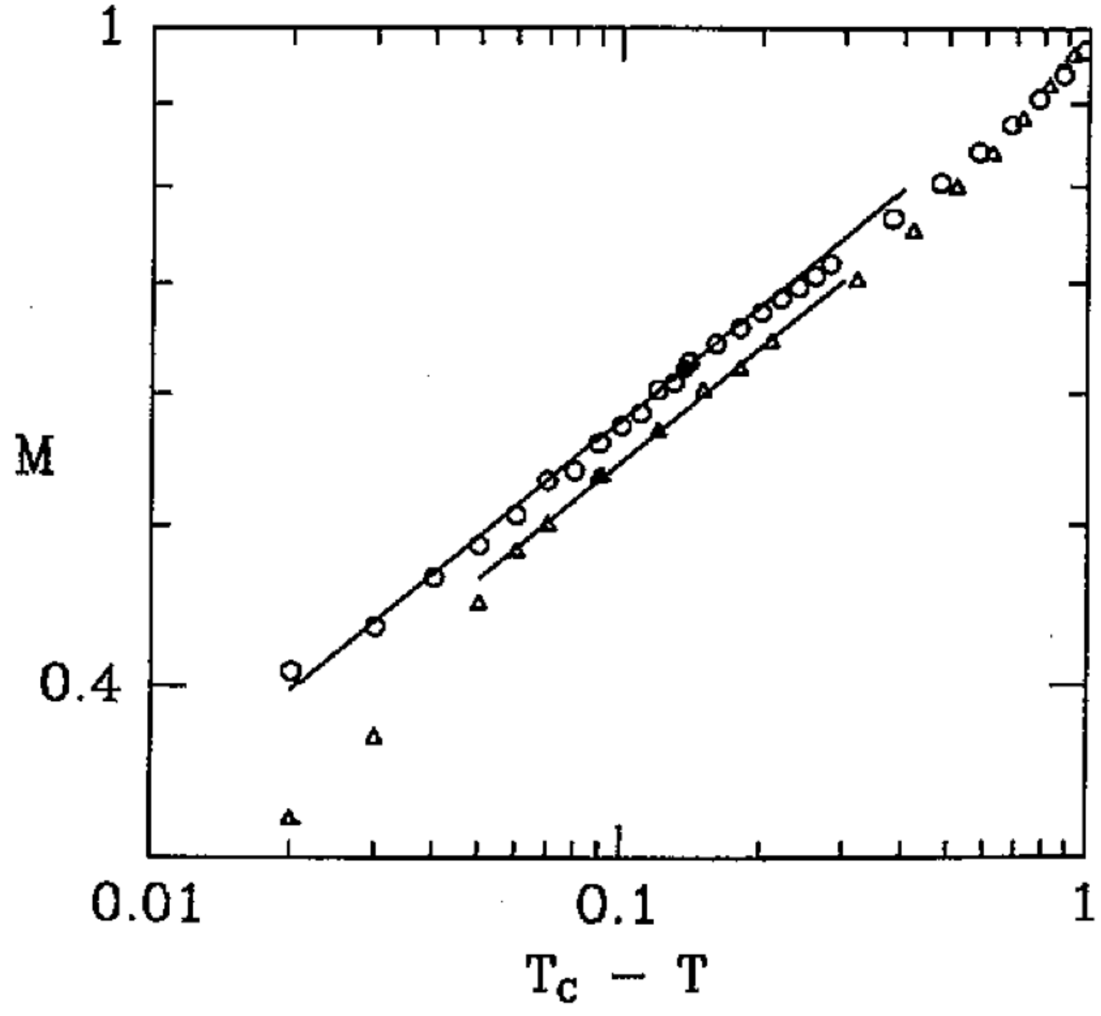

FIGURE 2.7: (Ref. [19]) $\log_{10}\langle m\rangle$ versus $\log_{10}(T_{\rm C}(L) - T)$ for XY models consisting of $N = 1024$ spins (circles) and $N = 10^4$ spins (triangles). The filled points correspond to the theoretical $T^*(L)$ of each system size. Curves corresponding to Eq. (2.133) with $\tilde{\beta} = 3\pi^2/128$ have been superimposed on the data.

models consisting of $N = 1024$ spins (circles) and $N = 10^4$ spins (triangles) [19]. Curves corresponding to Eq. (2.133) with $\tilde{\beta} = 3\pi^2/128$ have been superimposed on the data, showing the theory to apply to the system sizes presented. Here, BH set $T^*(L)$ to be the temperature at which $\langle m\rangle = (1/cN)^{1/16}$, since this corresponds to the effective spin stiffness $K_{\rm eff.}$ being $2/\pi$. $T_{\rm C}(L)$ is then set using the relationship that follows from combining Eqs. (2.128) and (2.131):

$$4\left(T^*(L) - T_{\rm BKT}\right) = T_{\rm C}(L) - T_{\rm BKT}. \tag{2.146}$$

This result has been commonly used by experimentalists to explain the fact that magnetic films and layers with XY symmetry invariably show a magnetization with an effective critical exponent given by $\tilde{\beta}^* = 3\pi^2/128$. A literature survey was performed by Taroni *et al.* [21] in which they categorize the critical exponents of a wide variety of magnetic systems: they find that an extensive number of layered [45–52] and thin-film [53–57] magnets display this signature of BH theory.

Chapter 3

Classical Electrostatics on a Lattice

In this chapter, the standard theory of two-dimensional lattice electrostatics is reformulated in a representation suitable for the thesis. To do this, the axioms of continuum electrostatics that were derived in Chapter 2 are rewritten in terms of discrete mathematics. This will be followed with an analysis of the harmonic mode of the electric field, the lattice partition function, and then the lattice Green's function and the chemical potentials.

3.1 Axioms and Notation

All lattice physics will be based upon functions being defined to be the discrete counterparts of smooth vector fields, any lattice vector field $\mathbf{F}$ will be defined [58] component-wise via

$$\mathbf{F}(\mathbf{x}) := F_x\left(\mathbf{x} + \frac{a}{2}\mathbf{e}_x\right)\mathbf{e}_x + F_y\left(\mathbf{x} + \frac{a}{2}\mathbf{e}_y\right)\mathbf{e}_y, \tag{3.1}$$

where $\mathbf{x}$ is a lattice point of the lattice D and $\mathbf{e}_{x/y}$ is the unit vector in the x/y direction, and the functional integral $\int \mathcal{D}\mathbf{F}$ of any lattice vector field $\mathbf{F}$ will be defined via

$$\int \mathcal{D}\mathbf{F} := \prod_{\mathbf{x}\in D}\left[\int_{\mathbb{R}} dF_x(\mathbf{x}) \int_{\mathbb{R}} dF_y(\mathbf{x})\right]. \tag{3.2}$$

All functions will be redefined as the lattice counterparts of their original continuum formulation, where applicable.

The grand-canonical energy of the two-dimensional lattice system is given by

$$U = \frac{\epsilon_0 a^2}{2}\sum_{\mathbf{x}\in D}|\mathbf{E}(\mathbf{x})|^2 + U_{\text{Core}}, \tag{3.3}$$

where D is the set of all charge lattice sites and a is the lattice spacing: the a^2 term gives the base element of area of the lattice system.

Introducing $\tilde{\boldsymbol{\nabla}}$ and $\hat{\boldsymbol{\nabla}}$ as the forwards and backwards finite-difference operators [58], respectively, Gauss' law on a lattice becomes

$$\hat{\boldsymbol{\nabla}} \cdot \mathbf{E}(\mathbf{x}) = \rho(\mathbf{x})/\epsilon_0, \tag{3.4}$$

where $\rho(\mathbf{x}) := qm(\mathbf{x})/a^2$ is the charge density at $\mathbf{x}$. In analogy with the functional analysis outlined in Section 2.1.1.2, it then follows that the electrostatic solution to this equation is given by

$$\mathbf{E}(\mathbf{x}) = -\tilde{\boldsymbol{\nabla}}\phi(\mathbf{x}) + \bar{\mathbf{E}}. \tag{3.5}$$

Upon defining $\boldsymbol{\nabla}^2 f(\mathbf{x}) := \hat{\boldsymbol{\nabla}} \cdot \tilde{\boldsymbol{\nabla}} f(\mathbf{x})$ as the lattice Laplacian [58] acting on some general scalar function f, Poisson's equation on a lattice follows:

$$\boldsymbol{\nabla}^2 \phi(\mathbf{x}) = -\rho(\mathbf{x})/\epsilon_0. \tag{3.6}$$

3.2 Polarization

The harmonic mode of the electric field contains two components: one describes the polarization of the system, while the other corresponds to the winding of charges around the torus. We note that, while there are no charge dynamics in electrostatics, certain electrostatic field configurations are the field configurations that would be left behind if a charge were to wind around the torus with a true dynamics: sampling electrostatic field configurations using the Gibbs ensemble leads to thermal averages from which one can infer an effective time average of charge-winding dynamics, hence, we refer to charge windings throughout. We now analyse the harmonic mode of the electric field by employing Gauss' law over subsets of the system.

In order to analyse the harmonic mode, we consider the sum of each component of the electric field over the entire lattice. We split the sum of the x/y-component into separate sums over all x/y-components that enter a particular strip of plaquettes of width a that wrap around the torus in the y/x direction. With this, we express each component of the harmonic mode $\bar{E}_{x/y}$ in terms of the charge enclosed along each of the strips of plaquettes:

$$L^2 \bar{E}_x = a^2 \sum_{\mathbf{x} \in D} E_x \left(\mathbf{x} + \frac{a}{2}\mathbf{e}_x \right) \tag{3.7}$$

$$
\begin{aligned}
=&a\sum_{x=0}^{L-2a}(x+a)\sum_{y=0}^{L-a}\left[E_x\left(x+\frac{a}{2},\,y\right)-E_x\left(x+\frac{3a}{2},\,y\right)\right]\\
&+La\sum_{y=0}^{L-a}\left[E_x\left(L-\frac{a}{2},\,y\right)-E_x\left(\frac{a}{2},\,y\right)\right]\\
&+La\sum_{y=0}^{L-a}E_x\left(\frac{a}{2},\,y\right) && (3.8)\\
=&-\frac{a^2}{\epsilon_0}\sum_{x=a}^{L}x\sum_{y=a}^{L}\rho\left(\mathbf{x}\right)+La\sum_{y=a}^{L}E_x\left(\frac{a}{2},\,y\right), && (3.9)
\end{aligned}
$$

which follows from applying Gauss' law to each strip of plaquettes that wrap around the torus in the y direction. The same argument holds for the y-component, hence, the harmonic mode is given by

$$\bar{\mathbf{E}}=-\frac{1}{\epsilon_0}\mathbf{P}+\frac{q}{L\epsilon_0}\mathbf{w}_0, \tag{3.10}$$

where $\mathbf{P}:=\sum_{\mathbf{x}\in D}\mathbf{x}\rho(\mathbf{x})/N$ is the origin-dependent polarization vector of the system and $w_{0,x}:=\epsilon_0 a\sum_{y=a}^{L}E_x(a/2,y)/q$ is the x-component of the origin-dependent winding field, with the y-component defined analogously. Here, $\mathbf{P}$ and $\mathbf{w}_0$ are measured from a specific origin. The above applies to systems composed of either single- or multi-valued charges.

We have thus shown that $\bar{\mathbf{E}}$, which is origin-independent, is given by the sum of two origin-dependent terms. One of these is attributed to the polarization of the system, while the other describes the winding of charges around the torus given that the polarization is measured with respect to the chosen origin: the harmonic-mode configurations that describe a given charge configuration are multi-valued. The topological sector of the system changes when a charge pair unbinds and winds around the torus in opposing directions before assuming its original configuration. This decomposition of $\bar{\mathbf{E}}$ therefore generates an origin-dependent measure of the topological sector of the system because, in certain cases, shifting the origin can lead to the exchange of quanta of field between the two $\bar{\mathbf{E}}$ terms.

Restricting our attention to the gas of elementary charges, we now devise an origin-independent measure of the topological sector of the system. First, we note that adding ω windings to either component of the harmonic mode $\bar{\mathbf{E}}$ corresponds to

$$\bar{E}_{x/y}\mapsto\bar{E}_{x/y}+\frac{q}{L\epsilon_0}\omega, \tag{3.11}$$

and that this results in a change in the grand-canonical energy of the system given by

$$\Delta U=\frac{Lq}{2}\omega\left(\frac{q}{L\epsilon_0}\omega+2\bar{E}_{x/y}\right). \tag{3.12}$$

Hence, given an arbitrary charge distribution, the lowest-energy harmonic mode that describes the charge distribution is an element of the set

$$\left(-\frac{q}{2L\epsilon_0}, \frac{q}{2L\epsilon_0}\right]. \tag{3.13}$$

We therefore define a convention in which the harmonic mode is written as

$$\bar{\mathbf{E}} = \bar{\mathbf{E}}_{\mathrm{p}} + \bar{\mathbf{E}}_{\mathrm{w}} \tag{3.14}$$

where $\bar{\mathbf{E}}_{\mathrm{p}}$ and $\bar{\mathbf{E}}_{\mathrm{w}}$ are the origin-independent polarization and winding components of the harmonic mode, respectively. This convention identifies the polarization component with the lowest-energy harmonic mode that describes a given charge distribution. The polarization component is found by applying modular-arithmetic to $\bar{\mathbf{E}}$:

$$\bar{E}_{\mathrm{p},x/y} \in \left(-\frac{q}{2L\epsilon_0}, \frac{q}{2L\epsilon_0}\right]. \tag{3.15}$$

$\bar{\mathbf{E}}_{\mathrm{w}}$ is then given by

$$\bar{\mathbf{E}}_{\mathrm{w}} = \frac{q}{L\epsilon_0}\mathbf{w}, \tag{3.16}$$

where the integer-valued vector field $\mathbf{w}$ (the winding field) is the origin-independent measure of the topological sector of the system and is chosen such that polarization component $\bar{\mathbf{E}}_{\mathrm{p}}$ fulfils Eq. (3.15). The winding field $\mathbf{w}$ now defines the topological sector of the system, corresponding to the number of times charges have wound around the torus in each direction. The lowest-energy electric-field configuration corresponds to $\mathbf{w} = \mathbf{0}$ for all charge configurations, and electric-field configurations corresponding to $\mathbf{w} \neq \mathbf{0}$ are the electrostatic field configurations that would be left behind if a charge were to wind around the torus from the $\mathbf{w} = \mathbf{0}$ field configuration with a true dynamics.

Non-zero topological sectors correspond to topological defects in the winding field $\mathbf{w}$. These topological defects are special in that they are not restricted to exist in plus-minus pairs. Electrostatics on a torus is therefore associated with two topologies: the local topological defects in the total electric field and the global topological defects in the winding field.

3.3 The Partition Function

In order to formulate the partition function in its full generality, we return to treat the gas of multi-valued charges: that is, the charges may be integer multiples of the elementary charge q.

The constraints imposed upon the electric-field representation by the strictly irrotational nature of the electric field, and by Eqs. (3.4) and (3.10), are combined with the grand-canonical energy of the system to write the partition function in terms of lattice electric fields. We define the set $X := q\mathbb{Z}/a^2$ such that the partition function for the two-dimensional electrostatic system on a lattice with toroidal topology is given by

$$Z_{\text{Coul.}} = \sum_{\{\rho(\mathbf{x})\in X\}} \sum_{\mathbf{w}_0\in\mathbb{Z}^2} \int \mathcal{D}\mathbf{E} \prod_{\mathbf{x}\in D} \left[\delta\left(\hat{\boldsymbol{\nabla}}\cdot\mathbf{E}(\mathbf{x}) - \rho(\mathbf{x})/\epsilon_0\right)\delta\left(\tilde{\boldsymbol{\nabla}}\times\mathbf{E}(\mathbf{x})\right)\right] \\ \times\delta\left(\frac{\epsilon_0}{N}\sum_{\mathbf{x}\in D}\mathbf{E}(\mathbf{x}) + \left(\mathbf{P} - \frac{q}{L}\mathbf{w}_0\right)\right)\exp\left(-\frac{\beta\epsilon_0 a^2}{2}\sum_{\mathbf{x}\in D}|\mathbf{E}(\mathbf{x})|^2\right)e^{-\beta U_{\text{Core}}}, \tag{3.17}$$

where $\sum_{\{\rho(\mathbf{x})\in X\}} := \prod_{\mathbf{x}\in D}\left[\sum_{\rho(\mathbf{x})\in X}\right]$ is the sum over all possible charge configurations.

The above partition function describes the grand-canonical physics of an irrotational $U(1)$ gauge field of multi-valued topological defects, where we only sum over $\{\mathbf{w}_0\}$ since the polarization is given by the charge configuration. The delta functions in Eq. (3.17) enforce the constraints imposed upon the electrostatic system: Gauss' law; the electric fields describing the unique, low-energy, irrotational solution to Gauss' law (a purely rotational field can be added to the total electric field without affecting Gauss' law); the form of the harmonic mode of the electric field. Note that charge neutrality does not need to be enforced with a delta function because electric fields on a torus describe charge-neutral systems.

In terms of the grand-canonical energy, the harmonic mode decouples from the Poisson part of the electric field (as shown in detail in Appendix C), hence,

$$Z_{\text{Coul.}} = \sum_{\{\boldsymbol{\nabla}^2\phi(\mathbf{x})\in Y\}} \exp\left(-\frac{\beta\epsilon_0 a^2}{2}\sum_{\mathbf{x}\in D}|\tilde{\boldsymbol{\nabla}}\phi(\mathbf{x})|^2\right)\sum_{\mathbf{w}_0\in\mathbb{Z}^2}\exp\left(-\frac{\beta}{2\epsilon_0}|L\mathbf{P} - q\mathbf{w}_0|^2\right)e^{-\beta U_{\text{Core}}}, \tag{3.18}$$

with the set $Y := q\mathbb{Z}/\epsilon_0 a^2$. We will show an extension to this transformation in more detail in Section 4.2.3.

3.4 The Effective Electric Permittivity

The effective electric permittivity of the Coulombic system $\epsilon_{\text{eff.}}$ rescales the electric permittivity of the vacuum ϵ_0 in the presence of charges: in the GCE, neutral charge pairs can be excited out of the vacuum, with the thermal averages of each species of charge pair dependent on both the temperature of the system and the value of the core-energy constant

ϵ_c of the charge species. The appearance of these charge pairs means that, on average, the system is no longer a vacuum at finite temperature, and its electric permittivity must change accordingly.

The effective electric permittivity is an important measure of Coulombic systems: in its two-dimensional form, it has direct analogues in all of the systems on to which the two-dimensional Coulomb gas maps, and is an important signature of the BKT transition [4, 22, 39]. It is the product of the electric permittivity of free space ϵ_0 and the temperature-dependent relative permittivity of the system $\epsilon_{\text{rel.}}$, which is proportional to the reciprocal of the second partial derivative of the grand potential of the system with respect to a small, global applied field $\mathbf{D}$, with the applied field taken continuously to zero. In the following, we consider an applied field restricted to the i direction.

Vallat and Beck showed [22] that the inverse effective electric permittivity $\epsilon_{\text{eff.}}^{-1}$ is given by the response function

$$\epsilon_{\text{eff.}}^{-1}(L,T) := \frac{1}{\epsilon_0^2 L^2} \left.\frac{\partial^2 \Phi(L,T,D_i)}{\partial D_i^2}\right|_{D_i \to 0}, \tag{3.19}$$

where D_i is the non-zero component of the applied field $\mathbf{D}$ and $\Phi(L,T,D_i)$ is the grand potential of the system at temperature T and under the influence of the applied field.

In the following, the field $\mathbf{E}$ is taken to be the electric field due to the charges. The partition function of the system under the influence of the applied field is then given by

$$\begin{aligned}
Z_{\text{Coul.},D_i} &:= \int \tilde{\mathcal{D}}\mathbf{E} \exp\left(-\frac{\beta\epsilon_0 a^2}{2}\sum_{\mathbf{x}\in D}|\mathbf{E}(\mathbf{x})+\mathbf{D}|^2\right)\exp\left(-\beta U_{\text{Core}}\right) && (3.20)\\
&= \int \tilde{\mathcal{D}}\mathbf{E} \exp\left(-\frac{\beta\epsilon_0 a^2}{2}\left(\sum_{\mathbf{x}\in D}|\mathbf{E}(\mathbf{x})|^2 + 2\sum_{\mathbf{x}\in D}\mathbf{E}(\mathbf{x})\cdot\mathbf{D} + \sum_{\mathbf{x}\in D}|\mathbf{D}|^2\right)\right)\\
&\quad \times \exp\left(-\beta U_{\text{Core}}\right) && (3.21)\\
&= \int \tilde{\mathcal{D}}\mathbf{E} \exp\left(-\frac{\beta\epsilon_0 a^2}{2}\left(\sum_{\mathbf{x}\in D}|\mathbf{E}(\mathbf{x})|^2 + 2\mathbf{D}\cdot\sum_{\mathbf{x}\in D}\mathbf{E}(\mathbf{x}) + N|\mathbf{D}|^2\right)\right)\\
&\quad \times \exp\left(-\beta U_{\text{Core}}\right) && (3.22)\\
&= \int \tilde{\mathcal{D}}\mathbf{E} \exp\left(-\frac{\beta\epsilon_0 a^2}{2}\left(\sum_{\mathbf{x}\in D}|\mathbf{E}(\mathbf{x})|^2 + 2ND_i\bar{E}_i + ND_i^2\right)\right)\\
&\quad \times \exp\left(-\beta U_{\text{Core}}\right), && (3.23)
\end{aligned}$$

where

$$\int \tilde{\mathcal{D}}\mathbf{E} := \sum_{\{\rho(\mathbf{x})\in X\}} \int \mathcal{D}\mathbf{E} \prod_{\mathbf{x}\in D}\left[\delta\left(\boldsymbol{\nabla}\cdot\mathbf{E}(\mathbf{x}) - \rho(\mathbf{x})/\epsilon_0\right)\delta\left(\tilde{\boldsymbol{\nabla}}\times\mathbf{E}(\mathbf{x})\right)\right] \tag{3.24}$$

is the constrained functional integral over electrostatic electric-field configurations. Combining this with the definition,

$$\Phi(L,T,D_i) := -\beta^{-1}\ln\left(Z_{\text{Coul.},D_i}\right), \tag{3.25}$$

the grand potential of the system under the influence of the applied field is given by

$$\Phi(L,T,D_i) = -\beta^{-1}\ln\left[\int \tilde{\mathcal{D}}\mathbf{E}\,\exp\left(-\frac{\beta\epsilon_0 a^2}{2}\left(\sum_{\mathbf{x}\in D}|\mathbf{E}(\mathbf{x})|^2 + 2ND_i\bar{E}_i + ND_i^2\right)\right)e^{-\beta U_{\text{Core}}}\right]. \tag{3.26}$$

The first partial derivative of the above equation with respect to the applied field D_i is given by

$$\frac{\partial\Phi(L,T,D_i)}{\partial D_i} = \frac{1}{\beta Z_{\text{Coul.},D_i}}\int\tilde{\mathcal{D}}\mathbf{E}\,\beta\epsilon_0 L^2\left(\bar{E}_i + D_i\right)\exp\left(-\beta U_{D_i}\right), \tag{3.27}$$

where U_{D_i} is the grand-canonical energy of the system under the influence of the applied field. In the limit of vanishing applied field, this quantity is the i-component of the harmonic mode of the electric field due to the charges, which was shown to be proportional to the charge polarization of a simply connected system (with a winding-field contribution for the toroidal system) in Section 3.2. The response function given by Eq. (3.19) is therefore the response of the harmonic mode of the electric field (due to the charges) to a small applied field (in the limit of vanishing applied field). The second partial derivative that generates this response function is then given by

$$\begin{aligned}\frac{\partial^2\Phi(L,T,D_i)}{\partial D_i^2} =& \frac{1}{\beta Z_{\text{Coul.},D_i}^2}\left(\int\tilde{\mathcal{D}}\mathbf{E}\,\beta\epsilon_0 L^2\left(\bar{E}_i + D_i\right)\exp\left(-\beta U_{D_i}\right)\right)^2\\ &+\frac{1}{\beta Z_{\text{Coul.},D_i}}\int\tilde{\mathcal{D}}\mathbf{E}\,\beta\epsilon_0 L^2\left(1-\beta\epsilon_0 L^2(\bar{E}_i + D_i)^2\right)\exp\left(-\beta U_{D_i}\right). \end{aligned}\tag{3.28}$$

Combining this with Eq. (3.19), we find that

$$\epsilon_{\text{eff.}}^{-1}(L,T) = \epsilon_0\left(1-\beta\epsilon_0 L^2\left(\langle\bar{E}_i^2\rangle - \langle\bar{E}_i\rangle^2\right)\right) \tag{3.29}$$

$$= \epsilon_0\left(1-\frac{1}{2}\chi_{\bar{\mathbf{E}}}(L,T)\right), \tag{3.30}$$

where

$$\chi_{\bar{\mathbf{E}}}(L,T) := \beta\epsilon_0 L^2\left(\langle\bar{\mathbf{E}}^2\rangle - \langle\bar{\mathbf{E}}\rangle^2\right) \tag{3.31}$$

is the harmonic-mode susceptibility, which measures fluctuations in the harmonic mode of the electric field due to the presence of charges. Eq. (3.30) follows from taking the average of both components of the electric field. It follows that the effective electric permittivity is given by

$$\epsilon_{\text{eff.}}(L,T) = \frac{\epsilon_0}{1 - \chi_{\bar{\mathbf{E}}}(L,T)/2}. \tag{3.32}$$

This is the effective electric permittivity of the system due to the introduction of charges to the vacuum.

Combining Eqs. (3.10) and (3.32), it follows that the effective electric permittivity is intimately related to the charge-charge correlations, and is therefore a signature of Coulombic physics. It is a function of the sum,

$$\sum_{\mathbf{x},\mathbf{x}' \in D} \mathbf{x} \cdot \mathbf{x}' \langle \rho(\mathbf{x}) \rho(\mathbf{x}') \rangle, \tag{3.33}$$

which increases dramatically when charge begins to deconfine, so that the effective electric permittivity, in turn, increases. In a conductor, the charges are able to rearrange to completely cancel the applied field, which results in a divergent effective electric permittivity.

In the thermodynamic limit, the standard two-dimensional Coulomb gas experiences a discontinuous universal jump in the effective electric permittivity as it passes through the BKT transition temperature T_{BKT} from below [4, 22, 39]. Here, $k_{\text{B}} T \epsilon_{\text{eff.}}$ discontinuously diverges from $\pi/2$ to infinity [4, 22, 39] as the system enters its conducting phase. The effective electric permittivity describes a renormalized vacuum permittivity due to the presence of charges: the value $k_{\text{B}} T \epsilon_{\text{eff.}}(L,T) = \pi/2$ at $T = T_{\text{BKT}}$ reflects precisely the same competition between confining energy and entropy that is seen with respect to the quantity $k_{\text{B}} T \epsilon_0 = \pi/2$ at $T = \bar{T}_{\text{BKT}}$ in Eq. (2.57) for the limitingly dilute Salzberg-Prager system, hence charge is deconfined in the standard two-dimensional Coulomb gas at temperatures above T_{BKT}. Note that the discontinuous jump is universal in the sense that it is a universal property of all systems in the XY universality class: the significance of the value $K_{\text{eff.}}(T) = 2/\pi$ at $T = T_{\text{BKT}}$ given in Section 2.3.6 is due to precisely the same competition as that described here with respect to the value $k_{\text{B}} T \epsilon_{\text{eff.}}(A,T) = \pi/2$ at $T = T_{\text{BKT}}$.

Fig. 3.1 shows the inverse effective electric permittivity for two-dimensional lattice Coulomb gases (of elementary charges) of various system sizes as functions of temperature. The data clearly shows a transition from an insulating (low-temperature) to a conducting (high-temperature) phase: as T_{BKT} is approached from below, the effective electric permittivity diverges, signalling charge deconfinement and the high-temperature phase of the BKT transition. We simulated this system using the MR algorithm, which is outlined in detail in Chapter 4. The lattice spacing a is set to unity: throughout the remainder of this thesis, we set $a = 1$, but we may write this quantity explicitly to help the reader in identifying units.

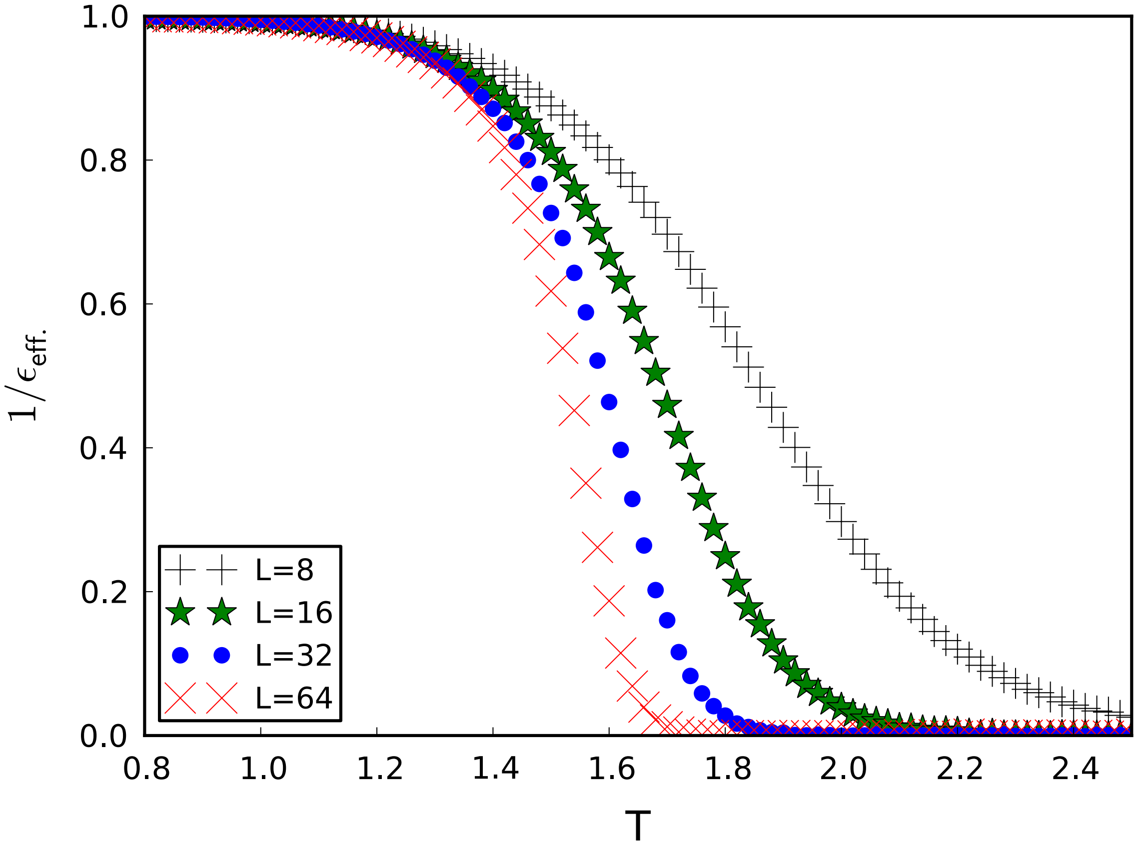

FIGURE 3.1: The inverse effective electric permittivity $1/\epsilon_{\mathrm{eff.}}$ for two-dimensional lattice Coulomb gases composed of elementary charges and of linear size $L = 8$, 16, 32 and 64 as functions of temperature T, where the lattice spacing a, the vacuum permittivity ϵ_0 and Boltzmann's constant k_{B} are set to unity and the elementary charge q is set to 2π. The data clearly shows a transition from an insulating (low-temperature) to a conducting (high-temperature) phase. We simulated this system using the MR algorithm, which is outlined in detail in Chapter 4. Simulation details are outlined in Appendix E.

Finally, the harmonic-mode susceptibility $\chi_{\bar{\mathbf{E}}}$ is not to be confused with the standard susceptibility of electrostatic theory χ', which is defined by

$$\chi'(L,T) := -\lim_{D_i \to 0} \left[\frac{\langle \bar{E}_i \rangle}{\langle \bar{E}_i + D_i \rangle} \right]. \tag{3.34}$$

Note that, in a more standard representation, the above becomes

$$\epsilon_0 \chi'(L,T) = \lim_{D_i \to 0} \left[\frac{\langle P_i \rangle}{\langle -P_i/\epsilon_0 + D_i \rangle} \right] \tag{3.35}$$

for a simply connected system (a toroidal topology results in the additional winding-field contribution), where P_i is the i-component of the charge polarization of the system. The harmonic-mode susceptibility is bounded above by 2, whereas the standard susceptibility diverges for a conductor (since the constituent charges of a conductor rearrange to cancel the applied field). The standard susceptibility is related to the effective electric permittivity by

$$\epsilon_{\text{eff.}}(L,T) = \epsilon_0 \left(1 + \chi'(L,T)\right). \tag{3.36}$$

3.5 The Lattice Green's Function

The use of lattice electric fields necessitates a Fourier description of the system in discrete **k**-space. The Green's function that describes the lattice electric field in two spatial dimensions is of a different form to the logarithmic continuum **k**-space expression: for large systems, the lattice Green's function converges on the continuum expression. To write the partition function in terms of the lattice Green's function, we consider Poisson's equation on a lattice (Eq. 3.5). This reduces to

$$\sum_{\mathbf{x}_\mu \in NN_{\mathbf{x}}} [\phi(\mathbf{x}) - \phi(\mathbf{x}_\mu)] = \frac{q}{\epsilon_0} \sum_{\mathbf{x}' \in D} m(\mathbf{x}')\, \delta_{\mathbf{x}\mathbf{x}'}, \tag{3.37}$$

where $NN_{\mathbf{x}}$ is the set of the nearest neighbours of $\mathbf{x}$ in the positive directions and $\delta_{\mathbf{x}\mathbf{x}'}$ is the Kronecker delta function.

We apply the principle of superposition such that the scalar potential at $\mathbf{x}$ (in terms of the lattice Green's function) is given by

$$\phi(\mathbf{x}) = \frac{q}{\epsilon_0} \sum_{\mathbf{x}' \in D} G(\mathbf{x}, \mathbf{x}')\, m(\mathbf{x}'), \tag{3.38}$$

which is combined with Eq. (3.37) to give

$$\delta_{\mathbf{x},\mathbf{x}'} = \sum_{\mu \in \{x,y\}} \left[2G(\mathbf{x},\mathbf{x}') - G(\mathbf{x} + a\mathbf{e}_\mu, \mathbf{x}') - G(\mathbf{x} - a\mathbf{e}_\mu, \mathbf{x}')\right]. \tag{3.39}$$

The system exists on a torus, hence the Green's function is periodic. We define the **k**-space Green's function via

$$\tilde{G}_{\mathbf{x}'}(\mathbf{k}) := \sum_{\mathbf{x} \in D} e^{-i\mathbf{k}\cdot\mathbf{x}} G(\mathbf{x}, \mathbf{x}'), \tag{3.40}$$

with the inverse Fourier transform given by

$$G(\mathbf{x}, \mathbf{x}') = \frac{1}{N} \sum_{\mathbf{k} \in B} e^{i\mathbf{k}\cdot\mathbf{x}} \tilde{G}_{\mathbf{x}'}(\mathbf{k}), \tag{3.41}$$

where $\sum_{\mathbf{k}\in B} := \prod_{\mu\in\{x,y\}} \left[\sum_{k_\mu \in B_\mu}\right]$, the set of **k**-space values in the μ-direction is given by

$$B_\mu := \{0, \pm\frac{2\pi}{N_\mu a}, \pm 2\frac{2\pi}{N_\mu a}, \cdots, \pm\left(\frac{N_\mu}{2} - 1\right)\frac{2\pi}{N_\mu a}, \frac{N_\mu}{2}\frac{2\pi}{N_\mu a}\}, \tag{3.42}$$

and $N_x = N_y = \sqrt{N}$.

To proceed, we use the standard result that $\sum_{\mathbf{k}\in B} e^{i\mathbf{k}\cdot(\mathbf{x}-\mathbf{x}')} = N\delta_{\mathbf{x}\mathbf{x}'}$, and write

$$\begin{aligned}\sum_{\mathbf{k}\in B} e^{i\mathbf{k}\cdot(\mathbf{x}-\mathbf{x}')} =& N \sum_{\mu\in\{x,y\}} \left[2G(\mathbf{x},\mathbf{x}') - G(\mathbf{x}+a\mathbf{e}_\mu,\mathbf{x}') - G(\mathbf{x}-a\mathbf{e}_\mu,\mathbf{x}')\right] && (3.43)\\ =& \sum_{\mathbf{k}\in B} e^{i\mathbf{k}\cdot\mathbf{x}}\left(4 - e^{ik_x a} - e^{-ik_x a} - e^{ik_y a} - e^{-ik_y a}\right)\tilde{G}_{\mathbf{x}'}(\mathbf{k}) && (3.44)\\ =& 2\sum_{\mathbf{k}\in B} e^{i\mathbf{k}\cdot\mathbf{x}}\left[2 - \cos(k_x a) - \cos(k_y a)\right]\tilde{G}_{\mathbf{x}'}(\mathbf{k}). && (3.45)\end{aligned}$$

This is solved by

$$\tilde{G}_{\mathbf{x}'}(\mathbf{k}) = \frac{e^{-i\mathbf{k}\cdot\mathbf{x}'}}{2\left[2-\cos(k_x a)-\cos(k_y a)\right]}\ \forall \mathbf{k} \neq \mathbf{0}, \tag{3.46}$$

where the $\mathbf{k} = \mathbf{0}$ part of the lattice Green's function is set to zero since the harmonic component of **E** is attributed to $\bar{\mathbf{E}}$. It follows that

$$G(\mathbf{x},\mathbf{x}') = \frac{1}{2N}\sum_{\mathbf{k}\neq\mathbf{0}} \frac{e^{i\mathbf{k}\cdot(\mathbf{x}-\mathbf{x}')}}{2 - \cos(k_x a) - \cos(k_y a)}. \tag{3.47}$$

The Green's function is the key difference between lattice and continuum electrostatics in any dimension. The lattice Green's function describes electric fields that are constrained to flow along lattice bonds connecting lattice sites, rather than fields that are free to emanate throughout position space. For suitably dilute lattice Coulomb gases, the continuum Green's function is a good approximation to the lattice physics since the lattice-field lines resemble continuum fields well; as the lattice becomes more densely populated with charge, the approximation begins to break down. As shown by Spitzer [59], the lattice Green's function approximation is given by

$$\lim_{L\to\infty} G(\mathbf{x},\mathbf{x}') \simeq -\frac{1}{2\pi}\ln\left|\frac{\mathbf{x}-\mathbf{x}'}{r_0}\right| \tag{3.48}$$

in the thermodynamic limit, and for $\mathbf{x} \neq \mathbf{x}'$. Here, $r_0 := ae^{-\gamma}/2\sqrt{2}$ (where γ is Euler's constant).

Finally, combining Eqs. (3.18), (3.37) and (3.38) with working analogous to that in Section 2.1.1.3, the partition function of a two-dimensional electrostatic lattice Coulomb gas on a torus is given by

$$Z_{\text{Coul.}} = \sum_{\{\rho(\mathbf{x})\in X\}} \delta\left(\sum_{\mathbf{x}\in D}\rho(\mathbf{x})\right)\exp\left[-\frac{\beta a^4}{2\epsilon_0}\sum_{\mathbf{x}_i,\mathbf{x}_j\in D}\rho(\mathbf{x}_i)G(\mathbf{x}_i,\mathbf{x}_j)\rho(\mathbf{x}_j)\right] \times \sum_{\mathbf{w}_0\in\mathbb{Z}^2}\exp\left(-\frac{\beta}{2\epsilon_0}|L\mathbf{P}-q\mathbf{w}_0|^2\right)e^{-\beta U_{\text{Core}}}, \tag{3.49}$$

with the Green's function given by Eq. (3.47), and where the delta function is introduced to enforce charge neutrality.

3.6 The Chemical Potential

The grand-canonical energy of the system is given by

$$U = U_{\text{Self}} + U_{\text{Int.}} + U_{\text{Harm.}} + U_{\text{Core}}, \tag{3.50}$$

where $U_{\text{Self}} := a^4\,G(\mathbf{0})\sum_{\mathbf{x}\in D}\rho(\mathbf{x})^2/2\epsilon_0$, $U_{\text{Int.}} := a^4\sum_{\mathbf{x}_i\neq\mathbf{x}_j\in D}\rho(\mathbf{x}_i)G(\mathbf{x}_i,\mathbf{x}_j)\rho(\mathbf{x}_j)/2\epsilon_0$ and $U_{\text{Harm.}} := L^2|\bar{\mathbf{E}}|^2/2\epsilon_0$ are the self, Coulombic charge-charge interaction and harmonic-mode components of the grand-canonical energy for the system, respectively, and the core-energy component U_{Core} is given by Eq. (2.34).

The chemical potentials are defined as in Eq. (2.36), so that, in full, the partition function given by

$$Z_{\text{Coul.}} = \sum_{\{\rho(\mathbf{x})\in X\}} \delta\left(\sum_{\mathbf{x}\in D}\rho(\mathbf{x})\right)\exp\left[-\frac{\beta a^4}{2\epsilon_0}\sum_{\mathbf{x}_i\neq\mathbf{x}_j}\rho(\mathbf{x}_i)G(\mathbf{x}_i,\mathbf{x}_j)\rho(\mathbf{x}_j)\right] \times e^{\beta\sum_{m\in\mathbb{Z}}\mu_m n_m}\sum_{\mathbf{w}_0\in\mathbb{Z}^2}\exp\left(-\frac{\beta}{2\epsilon_0}|L\mathbf{P}-q\mathbf{w}_0|^2\right) \tag{3.51}$$

describes a grand-canonical, charge-neutral electrostatic system on a two-dimensional lattice with toroidal topology. In Chapter 4, we will outline the MR electrostatic model in a lattice-field formulation, before using it to probe the BKT transition for the two-dimensional lattice Coulomb gas on a torus (which we consider to be the base BKT system) in Chapter 5. When probing the transition, we will control the number of each charge species by tuning each core energy.

Chapter 4

The Maggs-Rossetto Electrostatic Model

In Chapter 2, Coulombic charges were shown to interact with one another via long-ranged interaction potentials. This chapter is based around the work of Maggs and co-workers [24, 30–34], who devised a local model of Coulombic physics on a lattice. Here, we reformulate the MR electrostatic model [24] using a lattice notation and extend it to the GCE.

The MR electrostatic model [24] is a remarkable feat of statistical mechanics in which the Coulomb fluid is transformed into a local problem. The resultant algorithm locally simulates the physics of long-range Coulombic interactions on a lattice via the introduction of a freely fluctuating auxiliary field: the canonical electric-field description of Coulombic systems is extended to include all degrees of freedom of the field, utilizing the fact that the partition function of the MR electrostatic model is completely separable into its irrotational and rotational components. The model is an example of long-range interactions emerging from purely local physics. In Chapter 6, we will show the equivalence between the MR electrostatic model and the Villain model [23], thereby demonstrating this emergent phenomenon appearing in nature: this was the inspiration for the thesis.

The algorithm simulates Coulombic physics on a lattice: in this chapter, it is therefore formulated using discrete vector calculus. The formulation is also restricted to two spatial dimensions since this thesis is based on two-dimensional physics, and promotion to three dimensions follows easily.

4.1 Mathematical Background

The MR electrostatic model introduces a freely fluctuating auxiliary field to the Coulombic system. This field is divergence free everywhere and extends the electrostatic solution of Gauss' law to the general solution: its introduction results in local field updates alone being sufficient for the system to efficiently explore the Gibbs ensemble of the electrostatic problem. We will show that the partition function for the total field is separable into its Coulombic and auxiliary (or rotational) components: the auxiliary field contributes to the internal energy of the electric fields, but its partition function is independent of the Coulombic component.

The construction of the MR electrostatic model begins with a consideration of Gauss' law on a lattice,

$$\hat{\boldsymbol{\nabla}} \cdot \mathbf{E}(\mathbf{x}) = \rho(\mathbf{x})/\epsilon_0. \tag{4.1}$$

From here, it is standard practice to write the solution to Eq. (4.1) in terms of the unique minimum-energy configuration (MEC) of the electric field given by Eq. (3.5). This is not, however, the general solution to Gauss' law: Helmholtz' theorem of vector calculus allows us to extend this electric-field description to include the rotational degrees of freedom of the field. The total electric field of the MR electrostatic model is given by

$$\mathbf{E}(\mathbf{x}) = -\tilde{\boldsymbol{\nabla}}\phi(\mathbf{x}) + \tilde{\mathbf{E}}(\mathbf{x}) + \bar{\mathbf{E}}, \tag{4.2}$$

where the auxiliary field $\tilde{\mathbf{E}}$ contains the rotational degrees of freedom of the field and nothing else. This holds with previous electrostatic discussions, where $\tilde{\mathbf{E}}(\mathbf{x}) = \mathbf{0}$ everywhere. The lattice divergence of this extra term is zero, leaving us with Poisson's equation on a lattice:

$$\boldsymbol{\nabla}^2\phi(\mathbf{x}) = -\rho(\mathbf{x})/\epsilon_0. \tag{4.3}$$

The units of the electric field and of the electric permittivity are discussed in Appendix A.

Upon inserting the general solution to Gauss' law (on a lattice) given by Eq. (4.2) into Eq. (3.3), it follows that the grand-canonical energy of the MR electrostatic model is given by

$$U = U_{\text{Self}} + U_{\text{Int.}} + U_{\text{Rot.}} + U_{\text{Harm.}} + U_{\text{Core}}, \tag{4.4}$$

where $U_{\text{Rot.}} := \epsilon_0 a^2 \sum_{\mathbf{x}\in D} |\tilde{\mathbf{E}}(\mathbf{x})|^2/2$ is the auxiliary-field component of the grand-canonical energy, and we have used the fact that all coupling terms sum to zero, as shown in detail in Appendix C. This holds with the grand-canonical energy of the electrostatic system introduced in Chapter 2, where $U_{\text{Rot.}} = 0$.

4.2 Microscopic-variable Representation and the Partition Function

We start by defining two sets of microscopic variables that represent the local field updates outlined in Section 2.2. We will then write the partition function for the system in this microscopic-variable representation before transforming to the electric-field representation. Rewriting the partition function for the system in the electric-field representation will show that the MR electrostatic model reproduces Coulombic physics. In order to avoid bulky notation, we will use the same notation in the microscopic-variable representation as that used in the Villain model since the systems will be shown to be equivalent.

4.2.1 Microscopic Variables

A conjugate lattice D' is defined such that each site exists at the centre of each plaquette of D (D' is used because the conjugate lattice will be shown to be equivalent to the spin lattice of XY-type spin models in Chapter 6). Each site in D' is associated with a real-valued variable φ whose adjustment corresponds to an update of the auxiliary field (the rotational degrees of freedom of the total electric field), while each pair of nearest-neighbour sites is associated with an integer-valued variable s whose adjustment corresponds to a charge-hop update. Both sets of variables are subject to PBCs. Component-wise, we now define the field

$$[\boldsymbol{\Delta}\theta]_i\left(\mathbf{x}+\frac{a}{2}\mathbf{e}_i\right) := \frac{\varphi(\mathbf{x}+a\mathbf{e}_i)-\varphi(\mathbf{x})+qs(\mathbf{x}+a\mathbf{e}_i,\mathbf{x})}{a}, \tag{4.5}$$

where $\mathbf{e}_i$ is the unit vector in the i-direction ($i \in \{x, y\}$). The field $\boldsymbol{\Delta}\theta$ should be considered a field in itself, rather than the change in a scalar field. We identify the lattice electric field $\mathbf{E}$ with the following vector field:

$$\mathbf{E}(\mathbf{x}) \equiv \frac{1}{\epsilon_0}\begin{pmatrix} [\boldsymbol{\Delta}\theta]_y(\mathbf{x}+\frac{a}{2}\mathbf{e}_x) \\ \\ -[\boldsymbol{\Delta}\theta]_x(\mathbf{x}+\frac{a}{2}\mathbf{e}_y) \end{pmatrix}. \tag{4.6}$$

Note that the sites of the lattice vector-field components of lattices D and D' coexist.

We now consider the local field updates in terms of these new variables. A charge hop in the positive x/y direction corresponds to a decrease/increase in the relevant s variable by an amount q, as shown in Fig. 4.1 (where s_{ij} represents the s variable between sites $\mathbf{x}_i$ and $\mathbf{x}_j$ of the conjugate lattice).

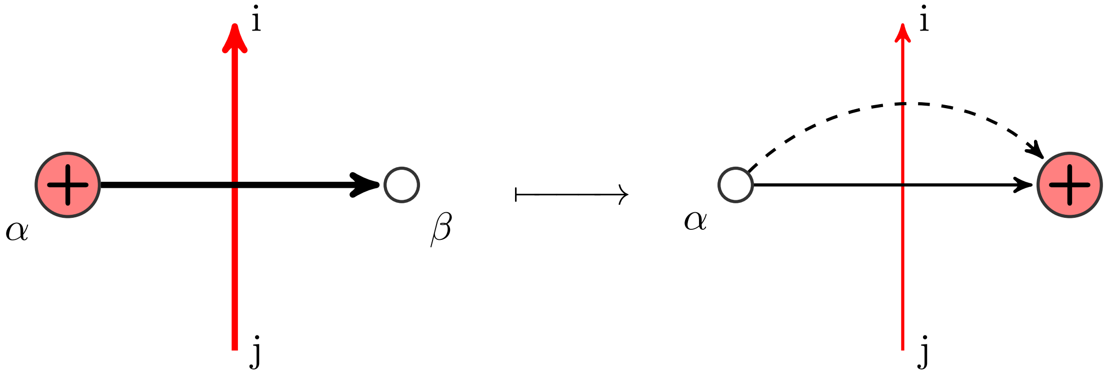

FIGURE 4.1: A charge-hop update in the positive x direction: The s_{ij} variable (red arrow) has its value decreased by an amount q. The value of the electric field flux $E_{\alpha\beta}$ (black arrow) flowing from site α to site β then decreases by q/ϵ_0, corresponding to a charge-hop update. Red circles represent positive charges; white circles represent empty charge sites.

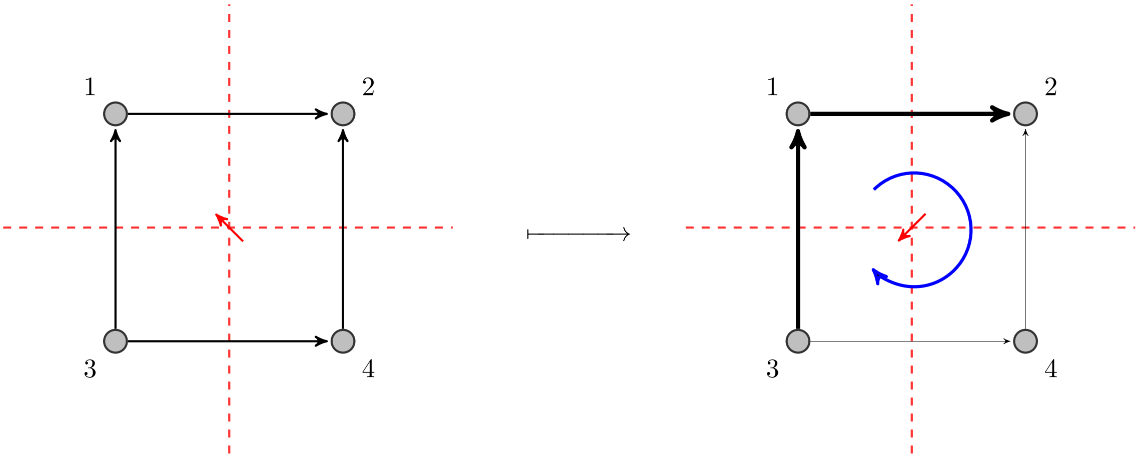

FIGURE 4.2: An update of the rotational degrees of freedom of the electric field: The value of the φ variable at the centre of a randomly chosen lattice plaquette decreases by an amount Δ. This rotates the electric flux by an amount Δ/ϵ_0 around the plaquette, leaving Gauss' law satisfied. Red arrows represent φ variables, black arrows represent the electric field, dashed red lines represent the conjugate lattice D', the blue arrow represents the direction of the field rotation and grey circles represent sites of arbitrary charge.

Fig. 4.2 then shows the microscopic-variable representation of an auxiliary-field update, with an alteration of a particular φ variable rotating the field around its surrounding plaquette: a change in the φ variable by an amount Δ rotates the electric flux around the surrounding plaquette by an amount Δ/ϵ_0. We represent the φ variables with spin-like arrows to emphasize the rotation of the electric field around the relevant plaquette.

With the grand-canonical energy of the system given by Eq. (3.3) we are able to write the partition function in the microscopic-variable representation. We consider the GCE, so we allow charge-hop updates to excite charges out of the vacuum, and we also include the possibility of all integer-valued multiples of the elementary charge. From Eq. (4.6) it then follows that

$$Z = \sum_{\{s(\mathbf{x},\mathbf{x}')\in\mathbb{Z}\}} \int \mathcal{D}\varphi \exp\left(-\frac{\beta}{2\epsilon_0}\sum_{\langle\mathbf{x},\mathbf{x}'\rangle} |\varphi(\mathbf{x}) - \varphi(\mathbf{x}') + qs(\mathbf{x},\mathbf{x}')|^2\right) \exp\left(-\beta U_{\mathrm{Core}}\right), \tag{4.7}$$

where the functional integral $\int \mathcal{D}\varphi$ is defined via

$$\int \mathcal{D}\varphi := \prod_{\mathbf{x}\in D'} \left[\int_{-q/2}^{q/2} d\varphi(\mathbf{x})\right]. \tag{4.8}$$

Here, the φ variables are restricted to the set $(-q/2, q/2]$ to avoid a multiple counting of electric-field configurations. In a representation that reflects the mechanics of the MR electrostatic model, this partition function describes a two-dimensional $U(1)$ lattice vector field permitted to explore all real values in each of its components. The reader may notice that the partition function given above is that of the Villain model of two-dimensional magnetism [23] (omitting the U_{Core} term, and with $q = 2\pi$). For sums over nearest-neighbour positions, all positions are on the D' lattice.

4.2.2 Gauss' Law

The microscopic variables reproduce Gauss' law:

$$\sum_{\mathbf{x}\in\partial\Gamma} \boldsymbol{\Delta}\theta(\mathbf{x}) \cdot \mathbf{l}(\mathbf{x}) = Q_\Gamma, \tag{4.9}$$

where Q_Γ is the charge enclosed within some subset of the lattice $\Gamma \subseteq D$, $\partial\Gamma \subset D'$ is the boundary enclosing Γ, and $\mathbf{l}$ traces an anticlockwise path along $\partial\Gamma$ and has dimensions of length. This equation results from the φ variables cancelling and the s variables being integer-valued. Combining Eqs. (4.6) and (4.9), it follows that

$$\sum_{\mathbf{x}\in\partial\Gamma} \boldsymbol{\Delta}\theta(\mathbf{x}) \cdot \mathbf{l}(\mathbf{x}) = a^2 \sum_{\mathbf{x}\in\Gamma} \epsilon_0 \hat{\boldsymbol{\nabla}} \cdot \mathbf{E}(\mathbf{x}) \tag{4.10}$$

$$\Rightarrow \hat{\boldsymbol{\nabla}} \cdot \mathbf{E}(\mathbf{x}) = \rho(\mathbf{x})/\epsilon_0, \tag{4.11}$$

recovering Eq. (4.1), as required.

The microscopic-variable representation transforms to the electric-field representation and also reproduces Gauss' law, resulting in the required lattice fields.

4.2.3 The Partition Function in the Electric-field Representation

Now that we have described the model using a representation that mimics the mechanics of the model, we rewrite the partition function in the electric-field representation to probe the validity of introducing the auxiliary field. The partition function is given by

$$
\begin{aligned}
Z = \sum_{\{\rho(\mathbf{x})\in X\}} \sum_{\mathbf{w}_0\in\mathbb{Z}^2} \int \mathcal{D}\mathbf{E} \prod_{\mathbf{x}\in D} \left[\delta\left(\hat{\boldsymbol{\nabla}}\cdot\mathbf{E}(\mathbf{x}) - \rho(\mathbf{x})/\epsilon_0\right)\right] \delta\left(\sum_{\mathbf{x}\in D}\mathbf{E}(\mathbf{x}) + \left(\frac{N}{\epsilon_0}\mathbf{P} - \frac{Lq}{\epsilon_0 a^2}\mathbf{w}_0\right)\right) \\
\times \exp\left(-\frac{\beta\epsilon_0 a^2}{2}\sum_{\mathbf{x}\in D}|\mathbf{E}(\mathbf{x})|^2\right)\exp\left(-\beta U_{\text{Core}}\right). \qquad (4.12)
\end{aligned}
$$

Notice that the delta function that enforced the electric fields of the system described by Eq. (3.17) to be irrotational is no longer included in order to allow the auxiliary field to freely fluctuate.

This partition function is separated into two components by defining the divergence-free field $\mathbf{e}$ [30] via

$$
\mathbf{e}(\mathbf{x}) := \mathbf{E}(\mathbf{x}) + \tilde{\boldsymbol{\nabla}}\phi(\mathbf{x}). \qquad (4.13)
$$

Then, since $\boldsymbol{\nabla}^2\phi(\mathbf{x}) = -\rho(\mathbf{x})/\epsilon_0$ and $\bar{\mathbf{E}} = -\mathbf{P}/\epsilon_0 + q\mathbf{w}_0/L\epsilon_0$, it follows that

$$
\begin{aligned}
Z = &\sum_{\{\boldsymbol{\nabla}^2\phi(\mathbf{x})\in Y\}} \exp\left(-\frac{\beta\epsilon_0 a^2}{2}\sum_{\mathbf{x}\in D}|\tilde{\boldsymbol{\nabla}}\phi(\mathbf{x})|^2\right) \sum_{\mathbf{w}_0\in\mathbb{Z}^2} \int \mathcal{D}\mathbf{e} \prod_{\mathbf{x}\in D}\left[\delta\left(\hat{\boldsymbol{\nabla}}\cdot\mathbf{e}(\mathbf{x})\right)\right] \\
&\times \delta\left(\sum_{\mathbf{x}\in D}\mathbf{e}(\mathbf{x}) + \left(\frac{N}{\epsilon_0}\mathbf{P} - \frac{Lq}{\epsilon_0 a^2}\mathbf{w}_0\right)\right) \exp\left(-\frac{\beta\epsilon_0 a^2}{2}\sum_{\mathbf{x}\in D}|\mathbf{e}(\mathbf{x})|^2\right) e^{-\beta U_{\text{Core}}} \qquad (4.14) \\
= &\sum_{\{\boldsymbol{\nabla}^2\phi(\mathbf{x})\in Y\}} \exp\left(-\frac{\beta\epsilon_0 a^2}{2}\sum_{\mathbf{x}\in D}|\tilde{\boldsymbol{\nabla}}\phi(\mathbf{x})|^2\right) \sum_{\mathbf{w}_0\in\mathbb{Z}^2} \exp\left(-\frac{\beta}{2\epsilon_0}|L\mathbf{P} - q\mathbf{w}_0|^2\right) e^{-\beta U_{\text{Core}}} \\
&\times \int \mathcal{D}\tilde{\mathbf{e}} \prod_{\mathbf{x}\in D}\left[\delta\left(\hat{\boldsymbol{\nabla}}\cdot\tilde{\mathbf{e}}(\mathbf{x})\right)\right] \delta\left(\sum_{\mathbf{x}\in D}\tilde{\mathbf{e}}(\mathbf{x})\right) \exp\left(-\frac{\beta\epsilon_0 a^2}{2}\sum_{\mathbf{x}\in D}|\tilde{\mathbf{e}}(\mathbf{x})|^2\right), \qquad (4.15)
\end{aligned}
$$

where $\tilde{\mathbf{e}}(\mathbf{x}) := \mathbf{e}(\mathbf{x}) - \bar{\mathbf{E}}$ is a purely rotational field and $Y := q\mathbb{Z}/\epsilon_0 a^2$ is the set of all charge configurations divided by ϵ_0. We now write the partition function as

$$
Z = Z_{\text{Coul.}}\, Z_{\text{Rot.}}, \qquad (4.16)
$$

where

$$Z_{\text{Coul.}} := \sum_{\{\boldsymbol{\nabla}^2\phi(\mathbf{x})\in Y\}} \exp\left(-\frac{\beta\epsilon_0 a^2}{2}\sum_{\mathbf{x}\in D}|\tilde{\boldsymbol{\nabla}}\phi(\mathbf{x})|^2\right)\sum_{\mathbf{w}_0\in\mathbb{Z}^2}\exp\left(-\frac{\beta}{2\epsilon_0}|L\mathbf{P}-q\mathbf{w}_0|^2\right)e^{-\beta U_{\text{Core}}} \tag{4.17}$$

and

$$Z_{\text{Rot.}} := \int \mathcal{D}\tilde{\mathbf{e}} \prod_{\mathbf{x}\in D}\left[\delta\left(\hat{\boldsymbol{\nabla}}\cdot\tilde{\mathbf{e}}(\mathbf{x})\right)\right]\delta\left(\sum_{\mathbf{x}\in D}\tilde{\mathbf{e}}(\mathbf{x})\right)\exp\left(-\frac{\beta\epsilon_0 a^2}{2}\sum_{\mathbf{x}\in D}|\tilde{\mathbf{e}}(\mathbf{x})|^2\right) \tag{4.18}$$

are the Coulombic and auxiliary-field components of the partition function, respectively.

The partition function given by Eq. (4.17) is precisely of the form of the partition function given by Eq. (3.18). This Coulombic component of the partition function separates from the auxiliary-field component: the auxiliary field is statistically independent of charge-charge correlations and the MR electrostatic model reproduces the desired grand-canonical, two-dimensional lattice Coulomb physics.

At this point, it is helpful to emphasize that charge-hop updates alter fields that are described by the entire partition function (hence the non-zero auxiliary field) while auxiliary-field updates only alter fields that are described by the auxiliary-field component of the partition function $Z_{\text{Rot.}}$. A local charge-hop update produces a greater change in the total energy density than the energy change due to electrostatic-field updates alone. The freely fluctuating auxiliary field solves this problem by allowing the total fields to relax to field configurations of lower energy.

4.2.4 The Partition Function in Terms of the Lattice Green's Function

The Coulombic partition function generated by the MR electrostatic model can now be written in terms of the lattice Green's function $G(\mathbf{x}_i, \mathbf{x}_j)$, as in Section 3.5:

$$\begin{aligned} Z_{\text{Coul.}} = \sum_{\{\rho(\mathbf{x})\in X\}} \delta\left(\sum_{\mathbf{x}\in D}\rho(\mathbf{x})\right)\exp\left[-\frac{\beta a^4}{2\epsilon_0}\sum_{\mathbf{x}_i,\mathbf{x}_j\in D}\rho(\mathbf{x}_i)G(\mathbf{x}_i,\mathbf{x}_j)\rho(\mathbf{x}_j)\right] \\ \times \sum_{\mathbf{w}_0\in\mathbb{Z}^2}\exp\left(-\frac{\beta}{2\epsilon_0}|L\mathbf{P}-q\mathbf{w}_0|^2\right)\exp\left(-\beta U_{\text{Core}}\right). \end{aligned} \tag{4.19}$$

With the chemical potentials introduced as in Section 2.1.1.4, the partition function given by

$$Z_{\text{Coul.}} = \sum_{\{\rho(\mathbf{x}) \in X\}} \delta\left(\sum_{\mathbf{x} \in D} \rho(\mathbf{x})\right) \exp\left[-\frac{\beta a^4}{2\epsilon_0} \sum_{\mathbf{x}_i \neq \mathbf{x}_j} \rho(\mathbf{x}_i) G(\mathbf{x}_i, \mathbf{x}_j) \rho(\mathbf{x}_j)\right]$$
$$\times e^{\beta \sum_{m \in \mathbb{Z}} \mu_m n_m} \sum_{\mathbf{w}_0 \in \mathbb{Z}^2} \exp\left(-\frac{\beta}{2\epsilon_0} |L\mathbf{P} - q\mathbf{w}_0|^2\right) \tag{4.20}$$

describes the electrostatics of the MR electrostatic model with tuneable chemical potentials. Again, we have the ability to control the number of each charge species by tuning each core energy as desired.

4.3 The Coulomb Gas of Elementary Charges

For the remaining analysis, we will restrict our attention to the standard BKT Coulomb gas of elementary charges by setting the core-energy constants to zero and infinity, as required: $\epsilon_c(m = 0, \pm 1) = 0$ and $\epsilon_c(m \neq 0, \pm 1) = \infty$. It follows that the Coulombic partition function for this system is given by

$$Z_{\text{Coul.}} = \sum_{\{\rho(\mathbf{x}) \in \{0, \pm q/a^2\}\}} \delta\left(\sum_{\mathbf{x} \in D} \rho(\mathbf{x})\right) \exp\left[-\frac{\beta a^4}{2\epsilon_0} \sum_{\mathbf{x}_i \neq \mathbf{x}_j} \rho(\mathbf{x}_i) G(\mathbf{x}_i, \mathbf{x}_j) \rho(\mathbf{x}_j)\right]$$
$$\times e^{\beta \mu n} \sum_{\mathbf{w} \in \mathbb{Z}^2} \exp\left(-\frac{L^2 \beta \epsilon_0}{2} |\bar{\mathbf{E}}_{\text{p}} + \frac{q}{L\epsilon_0} \mathbf{w}|^2\right), \tag{4.21}$$

where $\mu := \mu_{\pm 1}$ is the chemical potential for the introduction of an elementary charge, and we are now able to employ the origin-independent measures of the polarization $\bar{\mathbf{E}}_{\text{p}}$ and the winding $\bar{\mathbf{E}}_{\text{w}}$ components of the total harmonic mode $\bar{\mathbf{E}}$, as outlined in Section 3.2.

4.4 The Global Update

The winding component of the harmonic mode may also be independently sampled since an infinite number of winding fields describe the same charge configuration, and it is the charge configurations that the MR algorithm sets out to sample. For a system of elementary charges, these updates correspond to proposing a change in the harmonic mode given by

$$\bar{E}_{x/y} \mapsto \bar{E}_{x/y} + \frac{q}{L\epsilon_0} \omega, \tag{4.22}$$

where ω is some integer, as in Eq. (3.11). This final update is employed in the MR algorithm to improve efficiency [24].

A suitable ratio of the three updates described in this section therefore successfully samples the charge configurations of a Coulombic system. In Chapter 5, this model will be used to analyse the BKT transition by comparing winding-field (or topological-sector) fluctuations in the low- and high-temperature phases of the transition.

Chapter 5

Topological-sector Fluctuations at the BKT Transition

In the context of the two-dimensional lattice Coulomb gas on a torus, the BKT transition is a confinement – deconfinement phase transition with respect to the neutral charge pairs that make up the system. In the low-temperature phase, the charge pairs are tightly bound by their logarithmic Green's function and can never unbind; in the high-temperature phase, however, the entropic part of the free energy overcomes the confining energy of the system, resulting in deconfined charge. Eq. (4.21) therefore shows the relevance of the winding component of the harmonic mode in signalling the BKT transition: the two phases are characterized by non-fluctuating and fluctuating winding fields in the low- and high-temperature phases, respectively. As previously discussed, the winding field defines the topological sector of the system: in this chapter, we simulate the two-dimensional Coulomb gas using the MR algorithm to show that topological-sector fluctuations signal the high-temperature phase of the BKT transition.

For the standard BKT Coulomb gas of elementary charges (with the core-energy constant set to zero), the BKT transition occurs at $T_{\mathrm{BKT}} = 1.35$ (to 3 significant figures) [29] in the thermodynamic limit, which is scaled to higher temperatures in finite-size systems (see below). Fig. 5.1 shows the evolution of the (normalized) x-component of the harmonic mode of a system of linear size $L = 16$, simulated using local moves only (numerical simulation details are described in Appendix E). For the window of simulation time shown, zero topological-sector fluctuations are visible just below the BKT transition temperature $T_{\mathrm{BKT}} = 1.35$, but they become important at temperatures above T_{BKT}.

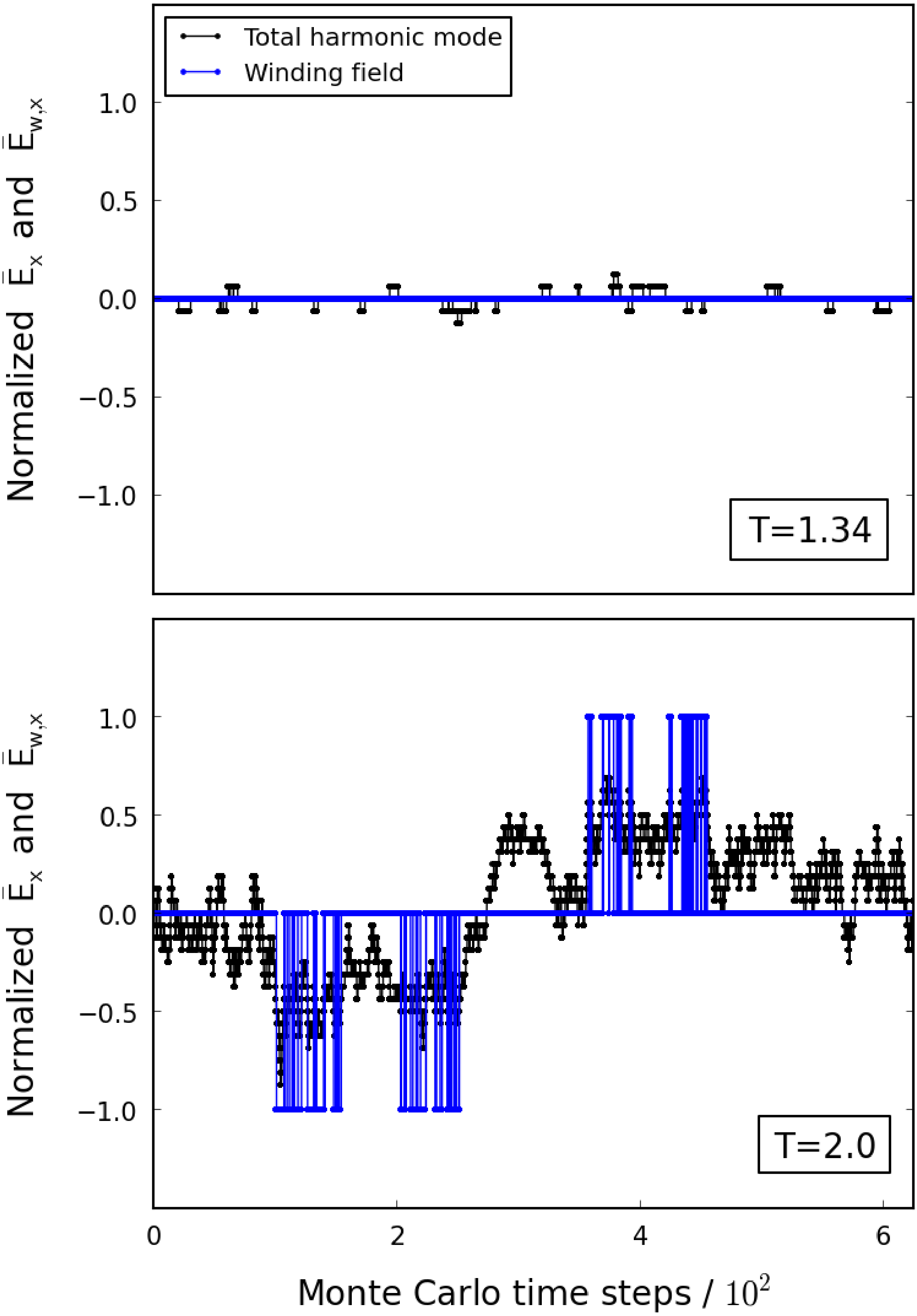

FIGURE 5.1: The x-component of the normalized total harmonic mode $L\bar{E}_x/2\pi$ (black) and winding field $L\bar{E}_{\mathrm{w},x}/2\pi$ (blue) versus Monte Carlo time for an $L \times L$ system of linear size $L = 16$ at $T = 1.34$ (top) and $T = 2.0$ (bottom). The system was simulated using the MR algorithm with local moves only. At the lower temperature, harmonic-mode fluctuations are finite but there are no topological-sector fluctuations, while at the higher temperature the winding-field component becomes finite, indicating topological-sector fluctuations.

In the thermodynamic limit, the difference in the behaviour of the harmonic mode seen in Fig. 5.1 is represented by the final exponent of Eq. (4.21) performing the transformation

$$-\frac{L^2\beta\epsilon_0}{2}|\bar{\mathbf{E}}_{\mathrm{p}}|^2 \mapsto -\frac{L^2\beta\epsilon_0}{2}|\bar{\mathbf{E}}_{\mathrm{p}} + \frac{q}{L\epsilon_0}\mathbf{w}|^2, \tag{5.1}$$

with $\mathbf{w}$ not strictly zero-valued in the high-temperature phase. The Coulombic partition function in the low-temperature phase is therefore given by

$$\begin{aligned} Z_{\mathrm{Coul.}}^{T<T_{\mathrm{BKT}}} = & \sum_{\{\rho(\mathbf{x})\in\{0,\pm q/a^2\}\}} \delta\left(\sum_{\mathbf{x}\in D}\rho(\mathbf{x})\right)\exp\left[-\frac{\beta a^4}{2\epsilon_0}\sum_{\mathbf{x}_i\neq\mathbf{x}_j}\rho(\mathbf{x}_i)G(\mathbf{x}_i,\mathbf{x}_j)\rho(\mathbf{x}_j)\right] \\ & \times e^{\beta\mu n}\exp\left(-\frac{L^2\beta\epsilon_0}{2}|\bar{\mathbf{E}}_{\mathrm{p}}|^2\right). \end{aligned} \tag{5.2}$$

5.1 Ergodicity Breaking

A convenient measure of topological-sector fluctuations in the electric field is the winding-field susceptibility χ_{w}:

$$\chi_{\mathrm{w}}(L,T) := \beta\epsilon_0 L^2\left(\langle\bar{\mathbf{E}}_{\mathrm{w}}^2\rangle - \langle\bar{\mathbf{E}}_{\mathrm{w}}\rangle^2\right). \tag{5.3}$$

As can be seen by combining Eqs. (4.21) and (5.3), limiting the Gibbs ensemble that contributes to $Z_{\mathrm{Coul.}}$ to configurations with zero charge results in Eq. (5.3) reducing to the winding-field susceptibility due to global moves only:

$$\begin{aligned} \chi_{\mathrm{w}}^{\mathrm{global}}(T) &= \beta\epsilon_0 L^2\left(\langle\bar{\mathbf{E}}_{\mathrm{w}}^2\rangle_{\mathrm{global}} - \langle\bar{\mathbf{E}}_{\mathrm{w}}\rangle_{\mathrm{global}}^2\right) && (5.4)\\ &= \beta\epsilon_0 L^2\frac{4q^2\exp\left(-\beta q^2/2\epsilon_0\right)/\epsilon_0^2L^2+\dots}{1+4\exp\left(-\beta q^2/2\epsilon_0\right)+\dots} && (5.5)\\ &\simeq \beta\epsilon_0 L^2\frac{4q^2\exp\left(-\beta q^2/2\epsilon_0\right)/\epsilon_0^2L^2}{1} && (5.6)\\ &= \frac{4\beta q^2}{\epsilon_0}\exp\left(-\beta q^2/2\epsilon_0\right), && (5.7) \end{aligned}$$

since $\langle\bar{\mathbf{E}}_{\mathrm{w}}\rangle = \mathbf{0}$, and where this approximation holds for $k_{\mathrm{B}}T \ll q^2/2\epsilon_0$. This expression is system-size independent and shows that an ergodic system would have small but finite topological-sector fluctuations at all temperatures.

Assuming local charge dynamics, a topological-sector fluctuation requires the separation of a charge pair over a distance greater than $L/2$ in either the x or the y direction, as seen in the condition placed upon the polarization component of the harmonic mode $\bar{\mathbf{E}}_{\mathrm{p}}$ (Eq. (3.15)). The energy barrier against such a configuration diverges logarithmically with the linear system size L [1–3]. As discussed in Section 2.1.2.2, entropy and charge screening make the free-energy barrier finite in the high-temperature phase. This allows charge pairs to unbind and trace closed paths around the torus, giving finite-valued winding fields, as observed in Fig. 5.1. In contrast, in the low-temperature phase, the probability of separation is strictly zero (a phase is defined in the thermodynamic limit). This results in an ergodicity breaking - a change in the phase space explored by the system - which is signalled by the strict suppression of topological-sector fluctuations in the electric field at $T < T_{\mathrm{BKT}}$. In the context of the Coulomb gas on a torus, the system is in an ergodic state if the same statistics are produced whether or not global dynamics are permitted to supplement the mandatory local dynamics. In order to explore this ergodicity breaking, we have therefore simulated the two-dimensional Coulomb gas, either with local field updates only, or with both local and global field updates [24, 30–34].

In the context of simulation, the system is ergodic if the sampling procedure both with the global update on and with the global update off produce the same statistics. To analyse the ergodicity of the system, we therefore define the susceptibility quotient $\chi_{\mathrm{w}}^{\mathrm{local}}/\chi_{\mathrm{w}}^{\mathrm{all}}$, where $\chi_{\mathrm{w}}^{\mathrm{local}}$ and $\chi_{\mathrm{w}}^{\mathrm{all}}$ are the winding-field susceptibilities as measured via the employment of local moves only and via the employment of both local and global moves, respectively. Fig. 5.2 shows the susceptibility quotient as a function of temperature for systems of linear size $L = 32$ and $L = 64$. The susceptibility quotient is zero in the regions $T < 1.075$ ($L = 32$) and $T < 1.2$ ($L = 64$), tends to unity in the region $T > 1.6$, and is a strongly fluctuating quantity between these temperatures. Simulations details (including the Monte Carlo timescale of the simulations) are outlined in Appendix E.

Fig. 5.2 clearly shows that ergodicity is broken in the vicinity of the BKT transition. For $T > 1.6$, $\chi_{\mathrm{w}}^{\mathrm{local}} = \chi_{\mathrm{w}}^{\mathrm{all}}$, indicating that the free-energy barrier for a topological-sector fluctuation via local charge dynamics is small. For $T < 1.075$ ($L = 32$) and $T < 1.2$ ($L = 64$), the quotient is zero, indicating that the energy barrier prevents topological-sector fluctuations via local dynamics. In between these low- and high-temperature regions there are strong fluctuations in the quotient because charge deconfinement via local dynamics represents increasingly rare events, an inevitable precursor to loss of ergodicity. In Section 5.2, this ergodicity breaking is shown to occur precisely at T_{BKT} in the thermodynamic limit.

Our analysis thus leads to a precise definition of topological order for the two-dimensional Coulomb gas through the ergodic freezing of the topological sector to its lowest absolute value. Two-dimensional systems with $U(1)$ symmetry are often associated with an absence of an ordering field at finite temperature [25]. Here we explicitly show that, in the case of the BKT transition, the ordering of a conventional order parameter is replaced by topological ordering through an ergodicity breaking between the topological sectors. The topological order is directly related to the confinement-deconfinement transition of the charges, the

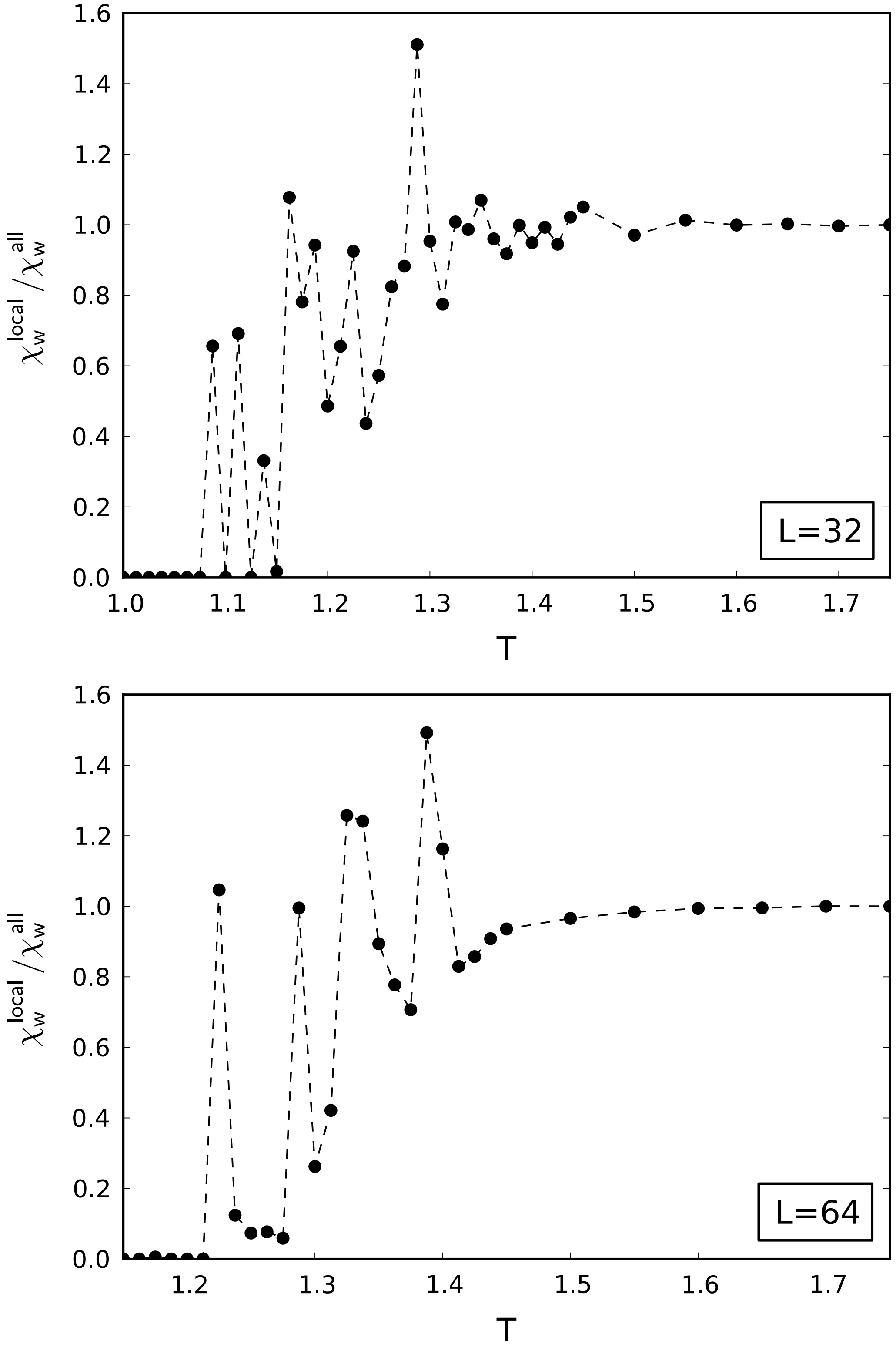

FIGURE 5.2: The susceptibility quotient $\chi_{\mathrm{w}}^{\mathrm{local}}/\chi_{\mathrm{w}}^{\mathrm{all}}$ versus temperature for an $L \times L$ Coulomb gas of linear size $L = 32$ (top) and $L = 64$ (bottom). In the regions $T < 1.075$ ($L = 32$) and $T < 1.2$ ($L = 64$), the quotient is zero, while for $T > 1.6$, the quotient approaches unity. This divergence between the results of the local-update and the all-updates simulations, accompanied by striking fluctuations in the intermediate region, signals ergodicity breaking as the system is cooled through the BKT transition. The line is a guide to the eye. Simulations details (including the Monte Carlo timescale of the simulations) are outlined in Appendix E.

local topological defects of the electric field. This type of ergodicity breaking is distinct from either the symmetry breaking that characterizes a standard phase transition, or that due to the rough free-energy landscape that develops at a spin-glass transition [27].

5.2 Finite-size Scaling

In order to explore the approach to the thermodynamic limit, the two-dimensional Coulomb gas was simulated by the Monte Carlo method as a function of system size, using the MR algorithm. The global update was employed in order to improve the statistics (numerical simulation details are described in Appendix E).

Fig. 5.3 shows the simulated winding-field susceptibility χ_{w} as a function of temperature for $L \times L$ Coulomb gases of linear sizes between $L = 8$ and $L = 64$. There is a marked increase in the winding-field susceptibility χ_{w} as the system passes through the BKT transition temperature $T_{\mathrm{BKT}} = 1.35$ [29] for all system sizes. Susceptibility curves for successive values of L intersect at temperatures above $T = 1.8$ and below $T = 1.5$. Between these two temperatures, the winding-field susceptibility increases for a given temperature as the linear system size L increases. These results are consistent with the finite-size scaling of the BKT transition temperature [19, 43]: as the system size decreases the effective transition temperature $T^*(L)$ increases.

Due to the logarithmic interaction potential, in the vicinity of T_{BKT}, the probability of a charge pair separating over a distance greater than $L/2$ increases with decreasing system size. This, combined with the finite-size transition temperature $T^*(L)$ also increasing with decreasing system size, results in the winding-field susceptibility curves for successive values of L intersecting in the vicinity of T_{BKT}. The inset in Fig. 5.3 shows that these low-temperature crossover points of the susceptibility curves are at $T = 1.45$, $T = 1.40$, and $T = 1.37$ (to three significant figures). The inset clearly shows that the crossover points tend towards a point of maximum curvature in the thermodynamic-limit susceptibility curve, from which topological-sector fluctuations increase dramatically. To extrapolate the data shown in Fig. 5.3 to the thermodynamic limit, we define the crossover temperature $T_{\mathrm{Cross}}(L)$ to be the lower temperature at which $\chi_{\mathrm{w}}(L) = \chi_{\mathrm{w}}(L/2)$.

Fig. 5.4 shows the crossover temperature T_{Cross} as a function of inverse system size $1/L$, along with a straight-line fit to the data. The thermodynamic-limit value of T_{Cross} corresponds to the y-intercept in the T_{Cross} versus $1/L$ plot. We find that $T_{\mathrm{Cross}}(L \to \infty) = 1.351(2)$, that is, it extrapolates to the BKT transition temperature [29]:

$$T_{\mathrm{Cross}}(L \to \infty) = T_{\mathrm{BKT}}. \tag{5.8}$$

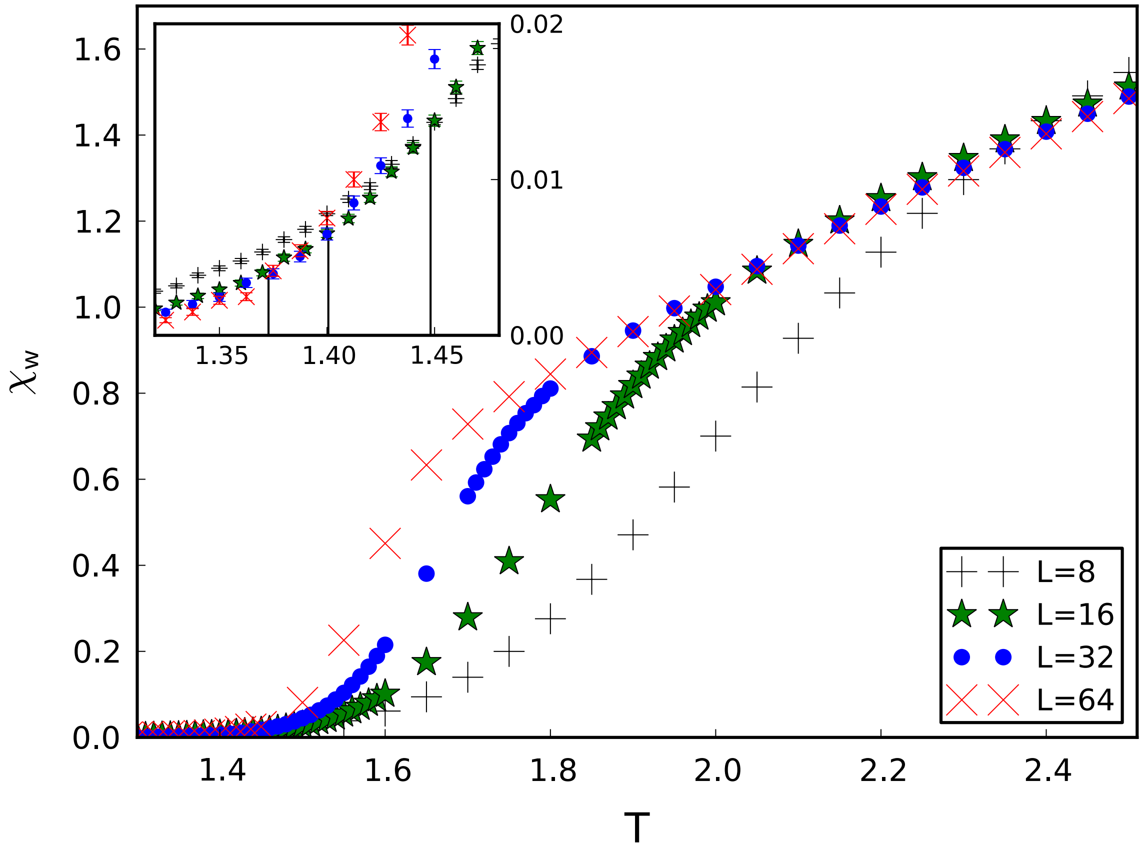

FIGURE 5.3: The winding-field susceptibility χ_w as a function of temperature for $L \times L$ Coulomb gases of linear size $L = 8$, 16, 32, and 64 (using local and global MR moves). The curves intersect at low and high temperature. Inset: An expanded plot of the data in the region of the low-temperature intersections (with error bars representing two standard deviations). The indicated crossover temperatures are given by $T_\mathrm{Cross}(L = 16) = 1.45$, $T_\mathrm{Cross}(L = 32) = 1.40$ and $T_\mathrm{Cross}(L = 64) = 1.37$ (to three significant figures), based on a data fit.

The point of maximum curvature in the thermodynamic-limit susceptibility curve therefore occurs at $T = T_\mathrm{BKT}$.

Similarly to the $\tilde{\Upsilon}_4$ scaling seen in the inset of Fig. 2.6, the scaling of the low-temperature crossover points T_Cross with inverse linear system size $1/L$ seen in Fig. 5.4 is in marked contrast to the scalings of the finite-size transition temperatures of the BKT transition [19, 43]. As seen in Section 2.5.2, the finite-size transition temperatures of the system can be fitted to $1/\ln^2(L)$ [19] scaling laws. $T_\mathrm{Cross.}$ is therefore neither $T^*(L)$ nor $T_C(L)$.

The magnitude of the winding-field susceptibility at the crossover points $\chi_\mathrm{w}^\mathrm{Cross}(L \to \infty)$ similarly extrapolates to $\sim 5 \times 10^{-4}$ in the thermodynamic limit, with an estimated error of the same order. This small number is not measurably different to the winding-field susceptibility due to global moves only, which, at T_BKT, evaluates to approximately 5×10^{-5} for all system sizes (see Eq. (5.7)). The inference is that topological-sector fluctuations due

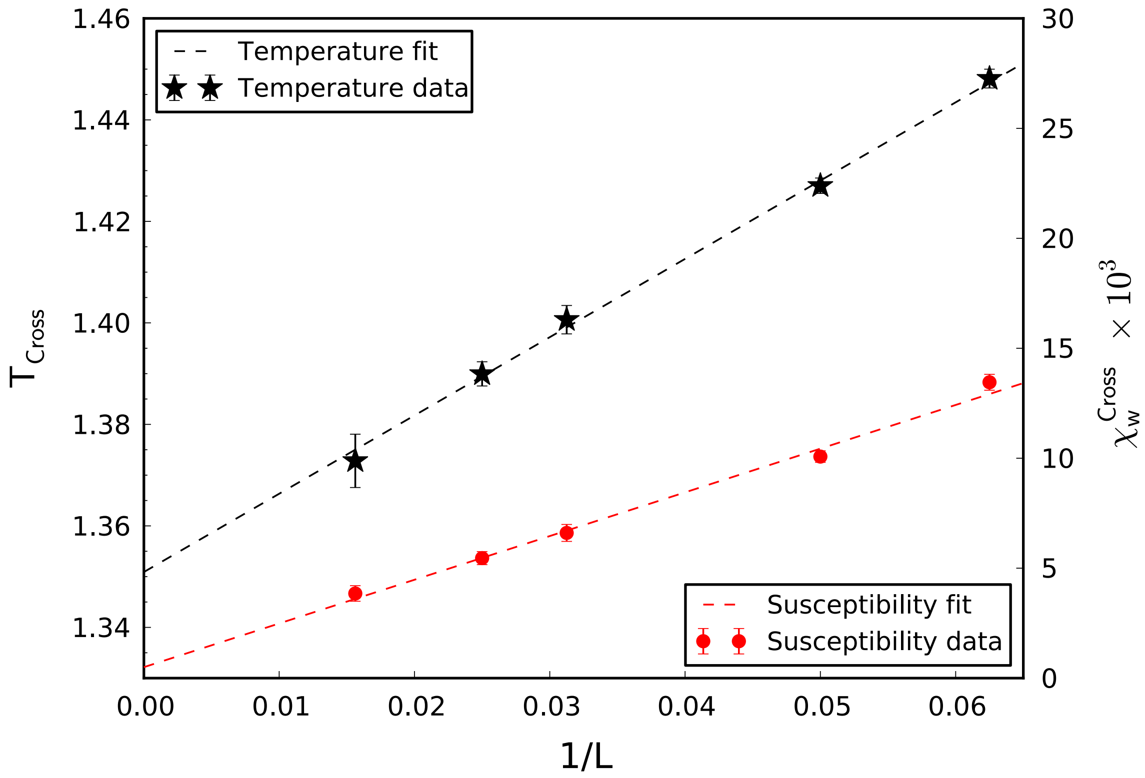

FIGURE 5.4: The crossover temperature T_{Cross} (black data) and crossover susceptibility $\chi_{\text{w}}^{\text{Cross}}$ (red data) as functions of inverse linear system size $1/L$, with error bars representing two standard deviations. Lines are weighted (with respect to the error bars) linear-regression fits to each data set, from which the y-intercept ($L \to \infty$) was calculated. $T_{\text{Cross}}(L \to \infty) = 1.351(2)$, equal to the BKT transition temperature T_{BKT} [29]. The crossover susceptibility $\chi_{\text{w}}^{\text{Cross}}(L \to \infty) \sim 5 \times 10^{-4}$ with an estimated error of the same order: there is no measurable difference between this quantity and the winding-field susceptibility due to global updates only at $T = 1.351$.

to local moves only turn on precisely at the universal point $T_{\text{Cross}}(L \to \infty) = T_{\text{BKT}}$ in the thermodynamic limit. This confirms that topological-sector fluctuations due to local moves signal charge deconfinement and the high-temperature phase of the BKT transition: in this phase, it follows that the harmonic-mode of the electric field can no longer be described by the polarization of the system alone.

This signalling of the high-temperature phase of the transition occurs at the temperature at which the system experiences the famous universal (and discontinuous) jump in the inverse effective electric permittivity $\epsilon_{\text{eff.}}^{-1}$ in the thermodynamic limit [4, 22, 38, 39]. This quantity is related to the harmonic-mode susceptibility by Eq. (3.32), from which it follows that $\chi_{\bar{\mathbf{E}}}$ makes a jump of order unity at T_{BKT}. As shown in Fig. 5.5, the ratio $(\chi_{\bar{\mathbf{E}}} - \chi_{\text{p}})/\chi_{\bar{\mathbf{E}}}$ is less than 5×10^{-2} for all $T \leq 1.6$ for systems of linear size $L = 8$ to 64, where

$$\chi_{\text{p}}(L, T) := \beta \epsilon_0 L^2 \left(\langle \bar{\mathbf{E}}_{\text{p}}^2 \rangle - \langle \bar{\mathbf{E}}_{\text{p}} \rangle^2 \right) \tag{5.9}$$

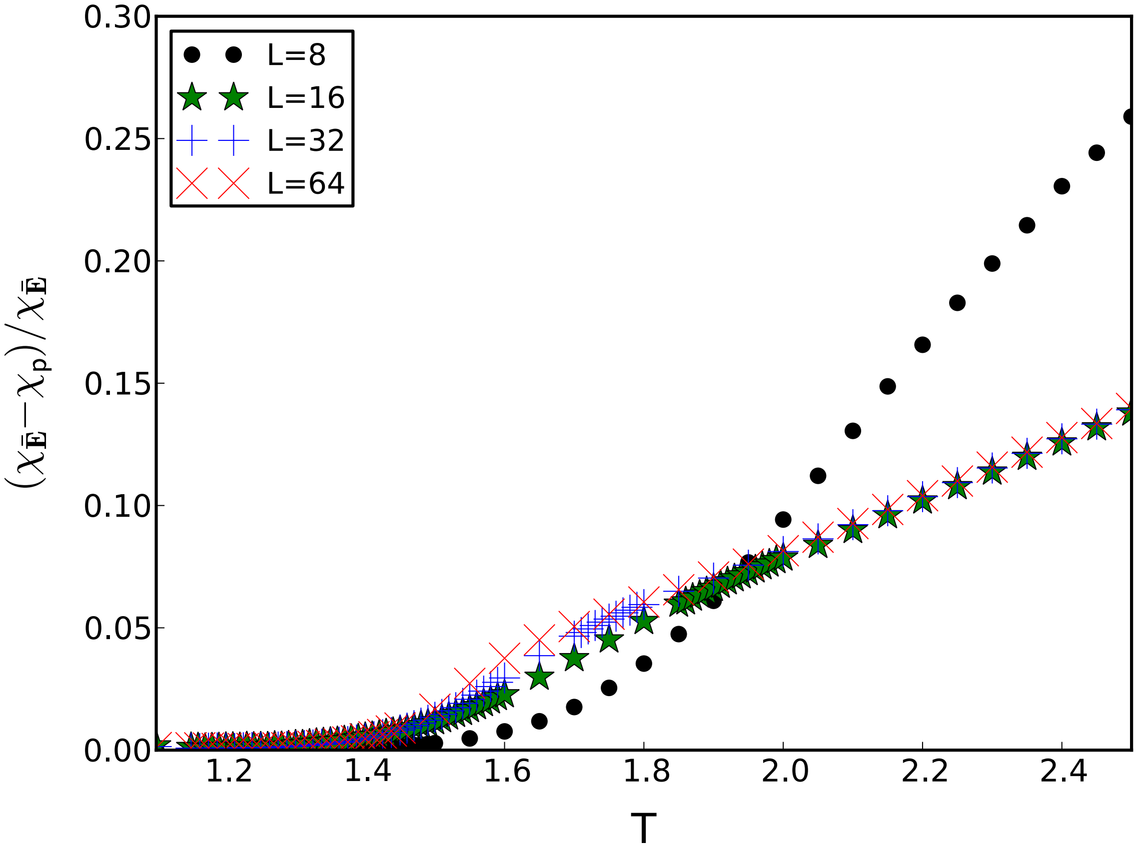

FIGURE 5.5: The ratio $(\chi_{\bar{\mathbf{E}}} - \chi_{\mathrm{p}})/\chi_{\bar{\mathbf{E}}}$ as a function of temperature for systems of linear size $L = 8$, 16, 32 and 64. We see that the contribution from topological-sector fluctuations to the universal jump in the harmonic-mode susceptibility $\chi_{\bar{\mathbf{E}}}$ is less than 5×10^{-2} for all system sizes at $T \leq 1.6$.

is the polarization susceptibility, showing that the contribution to the universal jump from topological-sector fluctuations is small. This is due to the near cancellation of $\langle \bar{\mathbf{E}}_{\mathrm{w}}^2 \rangle$ and the coupling term $2\langle \bar{\mathbf{E}}_{\mathrm{p}} \cdot \bar{\mathbf{E}}_{\mathrm{w}} \rangle$, which reflects the strong correlations between the polarization and winding components of the harmonic mode at the transition.

This chapter has shown that topological-sector fluctuations in the two-dimensional Coulomb gas on a torus due to local dynamics only signal the high-temperature phase of the BKT transition, but that these fluctuations only make a small contribution to the discontinuous jump in the effective electric permittivity. As the system passes from the high- to the low-temperature phase of the BKT transition, the phase space of the electric field explored by a system restricted to local dynamics decreases dramatically, and the system moves into a non-ergodic sector of the phase space of the electric field precisely at T_{BKT}. This displays the ergodicity-breaking nature of the BKT transition: again, this type of ergodicity breaking is distinct from either the symmetry breaking that characterizes a standard phase transition, or that due to the rough free-energy landscape that develops at a spin-glass transition [27].

Chapter 6

Emergent Electrostatics in XY-type Spin Models

In this chapter, the equivalence between the Villain model and the two-dimensional MR electrostatic model in the GCE is shown. An emergent-field description of XY-type spin models is introduced. It is then shown that the auxiliary field of the MR electrostatic model corresponds to the spin-wave field of the Villain model, and that topological-sector fluctuations in the emergent field correspond to twist fluctuations in the spin field of the XY models.

6.1 Continuum Formulation

Before moving to the continuum formulation, the lattice vector field $\boldsymbol{\Delta}\theta$ (the same notation is used as that in Chapter 4) is defined component-wise to be

$$[\boldsymbol{\Delta}\theta]_i\left(\mathbf{x}+\frac{a}{2}\mathbf{e}_i\right) := \frac{\varphi(\mathbf{x}+a\mathbf{e}_i)-\varphi(\mathbf{x})+qs(\mathbf{x}+a\mathbf{e}_i,\mathbf{x})}{a}, \tag{6.1}$$

for all XY-type spin models. In the continuum formulation, $\boldsymbol{\Delta}\theta$ becomes $\boldsymbol{\nabla}\theta$.

In order to gain an intuitive understanding of the XY model and its emergent electric field, we return to the continuum approximation of the model given by Eq. (2.63).

6.1.1 Spin-field Representation

In this subsection, we pause to review the standard analysis of the continuum, harmonic XY model presented by BKT [2, 3]. As seen in Fig. 2.3, any closed contour must adhere to

$$\oint_{\partial\Gamma} [\boldsymbol{\nabla}\theta(\mathbf{x})] \cdot d\mathbf{l} = 2\pi p, \tag{6.2}$$

where $p = 0, \pm 1$ and $\partial\Gamma$ is some closed path within the system. Upon transforming to the emergent-field representation, the above expression will become an emergent Gauss' law.

The spin-difference field $\boldsymbol{\nabla}\theta$ splits into two parts: its minimum-energy configuration (MEC) $\boldsymbol{\nabla}\bar{\theta}$ and fluctuations around these MECs $\boldsymbol{\nabla}\psi$ such that

$$\boldsymbol{\nabla}\theta(\mathbf{x}) = \boldsymbol{\nabla}\bar{\theta}(\mathbf{x}) + \boldsymbol{\nabla}\psi(\mathbf{x}). \tag{6.3}$$

These are called the vortex and spin-wave fields and are governed by the path integrals

$$\oint_{\partial\Gamma} \left[\boldsymbol{\nabla}\bar{\theta}(\mathbf{x})\right] \cdot d\mathbf{l} = 2\pi p \tag{6.4}$$

and

$$\oint_{\partial\Gamma} [\boldsymbol{\nabla}\psi(\mathbf{x})] \cdot d\mathbf{l} = 0. \tag{6.5}$$

The vortex field will be shown to map on to the irrotational component of the electric field of the MR electrostatic model, and the spin-wave field to the auxiliary field.

The vortex and spin-wave components of the spin-difference field energetically decouple. This is seen by considering Eq. (6.4) for a single vortex centred on the origin: this generates

$$\boldsymbol{\nabla}\bar{\theta}(r,\phi) = \boldsymbol{\nabla}\theta_{\text{Harm.}} + \frac{2\pi p}{r}\mathbf{e}_{\phi} \tag{6.6}$$

for any $r > r_0$ (with r_0 a lattice cut-off), and where $\boldsymbol{\nabla}\theta_{\text{Harm.}}$ is the harmonic component of the spin-difference field. We apply the principle of superposition to the above equation and write, for a system consisting of n vortices,

$$\boldsymbol{\nabla}\bar{\theta}(\mathbf{x}) = \boldsymbol{\nabla}\bar{\theta}_{\text{Harm.}} + \sum_{i=1}^{n} \frac{2\pi p_i}{|\mathbf{x} - \mathbf{x}_i|}\mathbf{e}_{\phi,i} \tag{6.7}$$

where $\mathbf{e}_{\phi,i}$ is the angular unit vector with respect to a coordinate system centred on vortex p_i (which exists at $\mathbf{x}_i$). For a single vortex p_i the following cross term sums to zero:

$$I_i := \int_{\Omega} \frac{2\pi p_i}{|\mathbf{x} - \mathbf{x}_i|}\mathbf{e}_{\phi_i} \cdot [\boldsymbol{\nabla}\psi(\mathbf{x})]\, d^2x$$

$$
\begin{aligned}
&= \int_{r_0}^{L} \int_0^{2\pi} \frac{2\pi p_i}{|\mathbf{x} - \mathbf{x}_i|} \left[\boldsymbol{\nabla}\psi(\mathbf{x})\right]_{\phi_i} r_i dr_i d\phi_i \\
&= 2\pi p_i \int_{r_0}^{L} \frac{1}{|\mathbf{x} - \mathbf{x}_i|} \left[\int_0^{2\pi} \left[\boldsymbol{\nabla}\psi(\mathbf{x})\right]_{\phi_i} r_i d\phi_i\right] dr_i \\
&= 2\pi p_i \int_{r_0}^{L} \frac{1}{|\mathbf{x} - \mathbf{x}_i|} \left[\oint_{\gamma_{r_i}} \left[\boldsymbol{\nabla}\psi(\mathbf{x})\right] \cdot d\mathbf{l}(\mathbf{x})\right] dr_i \qquad (6.8) \\
&= 0, \qquad (6.9)
\end{aligned}
$$

since the spin-wave contour integral vanishes for all paths. This shows that the non-harmonic part of the vortex field energetically decouples from the spin-wave field. Since the harmonic mode straightforwardly decouples from the rest of the spin-difference field, the continuum Hamiltonian becomes [2, 3]

$$
H_{\text{Cont.}} = \frac{J}{2} \int_\Omega |\boldsymbol{\nabla}\bar{\theta}(\mathbf{x})|^2 d^2x + \frac{J}{2} \int_\Omega |\boldsymbol{\nabla}\psi(\mathbf{x})|^2 d^2x, \qquad (6.10)
$$

where the total vortex field has been recombined.

6.1.2 Emergent-field Representation

The (continuum) emergent electric field of XY-type spin models can now be defined. The field defined by Binney *et al.* [60] is extended to include the spin-wave part of the spin-difference field:

$$
\mathbf{E}(\mathbf{x}) := J \left[\boldsymbol{\nabla}\theta(\mathbf{x})\right] \times \mathbf{e}_z. \qquad (6.11)
$$

The divergence of this field is given by

$$
\begin{aligned}
\boldsymbol{\nabla} \cdot \mathbf{E}(\mathbf{x}) &= \boldsymbol{\nabla} \cdot \left[J \left(\boldsymbol{\nabla}\theta(\mathbf{x})\right) \times \mathbf{e}_z\right] \\
&= J\partial_i \left[\epsilon_{ijk}(\boldsymbol{\nabla}\theta(\mathbf{x}))_j (\mathbf{e}_z)_k\right] \\
&= J\epsilon_{ijk}\partial_i \left[(\partial_j\theta(\mathbf{x}))(\mathbf{e}_z)_k\right] \\
&= J\epsilon_{ijk}(\partial_i\partial_j\theta(\mathbf{x}))(\mathbf{e}_z)_k \\
&= J\epsilon_{ijz}\partial_i\partial_j\theta(\mathbf{x}) \\
&= J \left[\boldsymbol{\nabla} \times \boldsymbol{\nabla}\theta(\mathbf{x})\right]_z . \qquad (6.12)
\end{aligned}
$$

Integrating over a subset Γ of the system then gives

$$
\begin{aligned}
\int_\Gamma \boldsymbol{\nabla} \cdot \mathbf{E}(\mathbf{x}) d^2x &= \int_\Gamma J \left[\boldsymbol{\nabla} \times \boldsymbol{\nabla}\theta(\mathbf{x})\right]_z d^2x \qquad (6.13) \\
&= J \int_\Gamma \left[\boldsymbol{\nabla} \times \boldsymbol{\nabla}\theta(\mathbf{x})\right] \cdot d\mathbf{a}(\mathbf{x}) \qquad (6.14)
\end{aligned}
$$

$$= J \oint_{\partial\Gamma} [\boldsymbol{\nabla}\theta(\mathbf{x})] \cdot d\mathbf{l}(\mathbf{x}) \tag{6.15}$$

$$= JQ_{\Gamma}, \tag{6.16}$$

where $d\mathbf{a}$ is an infinitesimal area element pointing in the positive z direction, $d\mathbf{l}$ is an infinitesimal element of the boundary enclosing Γ and $Q_{\Gamma} \in 2\pi\mathbb{Z}$ is the emergent charge enclosed within Γ. This generates the emergent Gauss' law

$$\boldsymbol{\nabla} \cdot \mathbf{E}(\mathbf{x}) = J\rho(\mathbf{x}), \tag{6.17}$$

where ρ is the density of the emergent electric charge. The topological defects in the spin-difference field have been transformed into topological defects in the emergent field: they are of precisely the same form as electric charges in the two-dimensional continuum Coulomb gas.

Using Helmholtz' theorem, any vector field can be split into its divergence-full, rotational and harmonic components:

$$\mathbf{E}(\mathbf{x}) = -\boldsymbol{\nabla}\phi(\mathbf{x}) + \boldsymbol{\nabla} \times \mathbf{Q}(\mathbf{x}) + \bar{\mathbf{E}}, \tag{6.18}$$

where ϕ and $\mathbf{Q}$ are smooth scalar and vector fields, respectively, and $\bar{\mathbf{E}} := \int_{\Omega} d^2x \mathbf{E}(\mathbf{x})/L^2$ is the harmonic mode of the emergent electric field. This generates an emergent Poisson's equation:

$$\boldsymbol{\nabla}^2\phi(\mathbf{x}) = -J\rho(\mathbf{x}). \tag{6.19}$$

We have that $|\mathbf{E}(\mathbf{x})| = |\boldsymbol{\nabla}\theta(\mathbf{x})| \cdot |\mathbf{e}_z| = |\boldsymbol{\nabla}\theta(\mathbf{x})|$, hence

$$H_{\text{Cont.}} = \frac{1}{2J} \int_{\Omega} |\mathbf{E}(\mathbf{x})|^2 d^2x, \tag{6.20}$$

the continuum Hamiltonian in the emergent-field representation. Appendix C shows that the irrotational and rotational parts of the above expression decouple (on a lattice, but the continuum analogue follows easily), hence

$$H_{\text{Cont.}} = \frac{1}{2J} \int_{\Omega} | - \boldsymbol{\nabla}\phi(\mathbf{x}) + \bar{\mathbf{E}}|^2 d^2x + \frac{1}{2J} \int_{\Omega} |\boldsymbol{\nabla} \times \mathbf{Q}(\mathbf{x})|^2 d^2x, \tag{6.21}$$

where the irrotational modes have been recombined to identify

$$J \left[\boldsymbol{\nabla}\bar{\theta}(\mathbf{x})\right] \times \mathbf{e}_z \equiv -\boldsymbol{\nabla}\phi(\mathbf{x}) + \bar{\mathbf{E}} \tag{6.22}$$

and

$$J\left[\boldsymbol{\nabla}\psi(\mathbf{x})\right] \times \mathbf{e}_z \equiv \boldsymbol{\nabla} \times \mathbf{Q}(\mathbf{x}). \tag{6.23}$$

This shows the emergent electrostatics of the continuum XY model. Identifying the Hamiltonian in the emergent-field representation with the internal energy of the electric fields of the two-dimensional continuum Coulomb gas amounts to asserting that the exchange coupling is an emergent inverse electric permittivity of free space: $J = 1/\epsilon_0$.

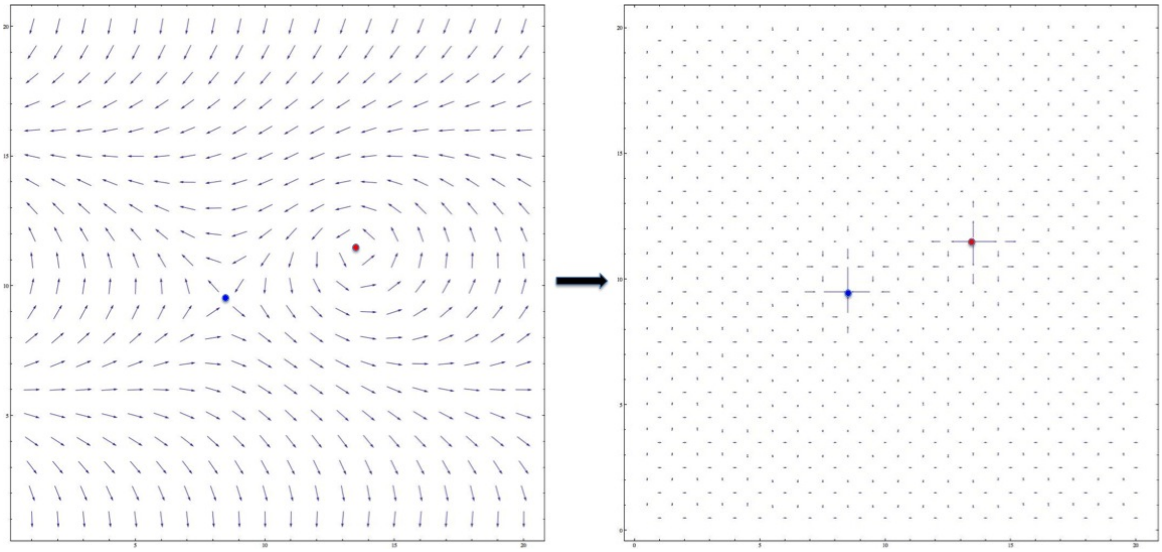

FIGURE 6.1: The lattice mapping between the spin configuration shown in Fig. 2.3 and the emergent-field representation. The red circle represents a positively charged topological defect; the blue circle represents a negatively charged topological defect

Although the lattice mapping is not of quite the same form as the continuum formulation outlined here, it is informative to display what will turn out to be the lattice mapping between the spin configuration shown in Fig. 2.3 and its emergent-field representation. This mapping, illustrated in Fig. 6.1, is addressed in the next section.

6.2 Lattice Mapping

Based on this intuitive understanding of the emergent physics of the continuum model, the mapping between the lattice ferromagnetic film and the lattice Coulomb gas is now presented.

6.2.1 The Villain Model

The Villain model explicitly samples modular variables, rather than defining them by the spin variables to which they couple: the s variables mimic the modular symmetry of the XY model and exist on the bonds between each lattice site. The partition function is given by Eq. (2.69), which is an almost identical partition function to that of the two-dimensional MR model of electrostatics in the microscopic-variable representation (Eq. (4.7)), with the only difference being that the Villain model has its core energies set to zero for all emergent-charge species: upon setting $q = 2\pi$, $\epsilon_0 = 1/J$ and $\epsilon_c(m) = 0 \forall m \in \mathbb{Z}$, the partition functions are equivalent (for an MR electrostatic model applied to multi-valued, dimensionless charges in the GCE).

The mapping between the two models is now straightforward. We define the emergent electric field $\mathbf{E}$ on a lattice:

$$\mathbf{E}(\mathbf{x}) := J \begin{pmatrix} [\mathbf{\Delta}\theta]_y(\mathbf{x} + \frac{a}{2}\mathbf{e}_x) \\ \\ -[\mathbf{\Delta}\theta]_x(\mathbf{x} + \frac{a}{2}\mathbf{e}_y) \end{pmatrix}. \tag{6.24}$$

With $\epsilon_0 = 1/J$, $q = 2\pi$ and $\epsilon_c(m) = 0 \, \forall m \in \mathbb{Z}$, it follows that the emergent field of the Villain model is of the same form as the electric field of the two-dimensional MR electrostatic model. These emergent charges are topological defects in the emergent electric field, but not in the spin-difference field $\varphi(\mathbf{x} + a\mathbf{e}_i) - \varphi(\mathbf{x})$: the φ variables do not define the modular variables of the model, hence the topological defects are not defined by the φ variables.

In Chapter 4, the microscopic mechanics of the MR electrostatic model and Gauss' law in terms of the microscopic-variable representation were presented. The same arguments hold here, hence the microscopic mechanics are identical (topological-defect hops are equivalent, and spin-wave updates in the Villain model are equivalent to auxiliary-field updates in the MR model) and the Villain model admits an emergent Gauss' law:

$$\hat{\mathbf{\nabla}} \cdot \mathbf{E}(\mathbf{x}) = J\rho(\mathbf{x}), \tag{6.25}$$

where $\rho(\mathbf{x}) := 2\pi m(\mathbf{x})/a^2$ is the emergent-charge density, and the integer $m(\mathbf{x})$ denotes the value of the emergent charge at $\mathbf{x}$ in units of 2π. The emergent field $\mathbf{E}$ is Helmholtz decomposed into the same form as Eq. (4.2) by defining emergent analogues of the Poisson, auxiliary and harmonic components of the electric field of the MR electrostatic model. As in Chapter 4, the partition function then splits into its Coulombic and auxiliary-field components:

$$Z = Z_{\text{Coul.}} Z_{\text{Rot.}}. \tag{6.26}$$

With $\bar{X} := 2\pi\mathbb{Z}/a^2$, the Coulombic component is given by

$$\begin{aligned} Z_{\text{Coul.}} := \sum_{\{\rho(\mathbf{x})\in\bar{X}\}} \delta\left(\sum_{\mathbf{x}\in D}\rho(\mathbf{x})\right)\exp\left[-\frac{a^4\beta J}{2}\sum_{\mathbf{x}_i\neq\mathbf{x}_j}\rho(\mathbf{x}_i)G(\mathbf{x}_i,\mathbf{x}_j)\rho(\mathbf{x}_j)\right] \\ \times e^{\beta\sum_{m\in\mathbb{Z}}\mu_m n_m}\sum_{\mathbf{w}_0\in\mathbb{Z}^2}\exp\left(-\frac{\beta J}{2}|L\mathbf{P}-2\pi\mathbf{w}_0|^2\right), \end{aligned} \tag{6.27}$$

where n_m is the number of emergent charges $2\pi m$,

$$\mu_m := -2\pi^2 JG(\mathbf{0})m^2 \tag{6.28}$$

is the the chemical potential for the introduction of an emergent charge $2\pi m$ (since the emergent core-energy constants are all zero),

$$\mathbf{P} := \frac{1}{N}\sum_{\mathbf{x}\in D}\mathbf{x}\rho(\mathbf{x}) \tag{6.29}$$

is the origin-dependent emergent polarization vector for the system, and

$$\mathbf{w}_0 := \frac{a}{2\pi J}\left(\sum_{y=a}^{L}E_x\left(\frac{a}{2},y\right),\sum_{x=a}^{L}E_y\left(x,\frac{a}{2}\right)\right) \tag{6.30}$$

is the origin-dependent emergent winding field. The auxiliary-field component is given by

$$Z_{\text{Rot.}} := \int\mathcal{D}\tilde{\mathbf{e}}\prod_{\mathbf{x}\in D}\left[\delta\left(\hat{\boldsymbol{\nabla}}\cdot\tilde{\mathbf{e}}(\mathbf{x})\right)\right]\delta\left(\sum_{\mathbf{x}\in D}\tilde{\mathbf{e}}(\mathbf{x})\right)\exp\left[-\frac{\beta a^2}{2J}\sum_{\mathbf{x}\in D}|\tilde{\mathbf{e}}(\mathbf{x})|^2\right], \tag{6.31}$$

where the field

$$\tilde{\mathbf{e}}(\mathbf{x}) := \mathbf{E}(\mathbf{x}) + \tilde{\boldsymbol{\nabla}}\phi(\mathbf{x}) - \bar{\mathbf{E}} \tag{6.32}$$

is similarly defined.

For all XY-type spin models, we define $\boldsymbol{\Delta}\bar{\theta}$ to be the field that describes the MECs of the system, and the spin-wave field $\boldsymbol{\Delta}\psi$, which describes fluctuations around the MECs, to be the remainder of the total field $\boldsymbol{\Delta}\theta$ in the spin-field representation:

$$\boldsymbol{\Delta}\theta(\mathbf{x}) = \boldsymbol{\Delta}\bar{\theta}(\mathbf{x}) + \boldsymbol{\Delta}\psi(\mathbf{x}). \tag{6.33}$$

The transformation of the field $\boldsymbol{\Delta}\bar{\theta}$ to the emergent-field representation then corresponds to the irrotational components of the emergent field, and the equivalent transformation of the field $\boldsymbol{\Delta}\psi$ corresponds to the rotational components of the emergent field:

$$-\tilde{\boldsymbol{\nabla}}\phi(\mathbf{x}) + \bar{\mathbf{E}} \equiv J \begin{pmatrix} [\boldsymbol{\Delta}\bar{\theta}]_y(\mathbf{x} + \frac{a}{2}\mathbf{e}_x) \\ \\ -[\boldsymbol{\Delta}\bar{\theta}]_x(\mathbf{x} + \frac{a}{2}\mathbf{e}_y) \end{pmatrix}, \tag{6.34}$$

and

$$\tilde{\mathbf{E}}(\mathbf{x}) \equiv J \begin{pmatrix} [\boldsymbol{\Delta}\psi]_y(\mathbf{x} + \frac{a}{2}\mathbf{e}_x) \\ \\ -[\boldsymbol{\Delta}\psi]_x(\mathbf{x} + \frac{a}{2}\mathbf{e}_y) \end{pmatrix}. \tag{6.35}$$

We thus confirm the emergence of electric charges described by a $U(1)$ gauge field in the Villain model by showing the absolute equivalence between this model and the two-dimensional MR electrostatic model applied to dimensionless charges in the GCE (with all core-energy constants set to zero). Given the definitions of the helicity moduli Υ of the magnetic systems and the effective electric permittivity $\epsilon_{\text{eff.}}$ of the Coulomb gas (Eqs. (2.110) and (3.19)), it follows from the emergent electrostatics of the Villain model ($J = \epsilon_0^{-1}$) that the finite-size helicity modulus of the Villain model is precisely the inverse effective electric permittivity of the two-dimensional lattice Coulomb gas [22]:

$$\tilde{\Upsilon}(L,T) = \epsilon_{\text{eff.}}^{-1}(L,T). \tag{6.36}$$

As for the two-dimensional Coulomb gas, a harmonic-mode susceptibility $\chi_{\bar{\mathbf{E}}}$, which is a function of the emergent charge-charge correlations, is defined for the emergent field (from Eq. (3.31)), and it follows that

$$\tilde{\Upsilon}(L,T) = J\left(1 - \chi_{\bar{\mathbf{E}}}(L,T)/2\right) = \epsilon_0^{-1}\left(1 - \chi_{\bar{\mathbf{E}}}(L,T)/2\right) = \epsilon_{\text{eff.}}^{-1}(L,T). \tag{6.37}$$

As analogously discussed in Section 3.32, the helicity modulus of the Villain model is therefore intimately related to the emergent charge-charge correlations. It is a signature of the emergent MR physics of the system, so that a zero-valued helicity modulus signals emergent Coulombic conductivity.

6.2.2 The 2dHXY Model

The partition function of the HXY model is given by

$$Z_{\text{HXY}} = \int \bar{\mathcal{D}}\varphi \exp\left[-\frac{\beta J}{2} \sum_{\langle \mathbf{x},\mathbf{x}'\rangle} |\varphi(\mathbf{x}) - \varphi(\mathbf{x}') + 2\pi s(\mathbf{x},\mathbf{x}')|^2\right], \tag{6.38}$$

where the s variables are now defined via the associated spin difference: $s(\mathbf{x}, \mathbf{x}') \in \{0, \pm 1\}$ is chosen such that $\varphi(\mathbf{x}) - \varphi(\mathbf{x}') + 2\pi s(\mathbf{x}, \mathbf{x}') \in (-\pi, \pi]$. This enforces the modular periodicity required in XY-type spin models, but the spin variables now define the modular variables. Topological defects are therefore defects in the spin-difference field $\varphi(\mathbf{x} + a\mathbf{e}_i) - \varphi(\mathbf{x})$ (and in the emergent electric field $\mathbf{E}$).

The emergent electric field is defined as in Eq. (6.24), which produces an emergent Gauss' law of the same form as Eq. (6.25). Again, this emergent field is Helmholtz decomposed into the same form as Eq. (4.2) so that the Hamiltonian can be written in its emergent-field representation:

$$H_{\text{HXY}} = \frac{a^4 J}{2} \sum_{\mathbf{x}_i, \mathbf{x}_j \in D} \rho(\mathbf{x}_i) G(\mathbf{x}_i, \mathbf{x}_j) \rho(\mathbf{x}_j) + \frac{a^2}{2J} \sum_{\mathbf{x} \in D} |\tilde{\mathbf{E}}(\mathbf{x})|^2 + \frac{L^2}{2J} |\bar{\mathbf{E}}|^2. \tag{6.39}$$

Geometrically, emergent charges given by $m(\mathbf{x}) \neq 0, \pm 1$ are not permitted for any emergent-charge lattice site: this enforces a core-energy configuration $\{\epsilon_c(m = 0, \pm 1) = 0, \epsilon_c(m \neq 0, \pm 1) = \infty\}$ that corresponds to a system of elementary emergent charges. The polarization and winding components of the harmonic mode of the emergent field of an elementary-charge system can be computed via the modulo approach outlined in Section 3.2: $\bar{\mathbf{E}} = \bar{\mathbf{E}}_{\text{p}} + \bar{\mathbf{E}}_{\text{w}}$, where

$$\bar{E}_{\text{p},x/y} \in \left(-\frac{\pi J}{L}, \frac{\pi J}{L} \right], \tag{6.40}$$

and

$$\bar{\mathbf{E}}_{\text{w}} = \frac{2\pi J}{L} \mathbf{w}. \tag{6.41}$$

Here, the origin-independent winding field $\mathbf{w}$ defines the topological sector of the emergent electric field and is chosen such that Eq. (6.40) holds. The Hamiltonian given by Eq. (6.39) then becomes

$$H_{\text{HXY}} = -\mu n + \frac{a^4 J}{2} \sum_{\mathbf{x}_i \neq \mathbf{x}_j} \rho(\mathbf{x}_i) G(\mathbf{x}_i, \mathbf{x}_j) \rho(\mathbf{x}_j) + \frac{a^2}{2J} \sum_{\mathbf{x} \in D} |\tilde{\mathbf{E}}(\mathbf{x})|^2 + \frac{L^2}{2J} |\bar{\mathbf{E}}_{\text{p}} + \frac{2\pi J}{L} \mathbf{w}|^2, \tag{6.42}$$

where $\mu := \mu_1$ is the chemical potential for the introduction of an elementary emergent charge (defined in Eq. (6.28)), and n is the number of emergent charges. It follows that the HXY Hamiltonian corresponds to the internal energy of an emergent electric field:

$$H_{\text{HXY}} = U = U_{\text{Self}} + U_{\text{Int.}} + U_{\text{Rot.}} + U_{\text{Harm.}}, \tag{6.43}$$

where $U_{\text{Self}} := -\mu n$ (since $U_{\text{Core}} = 0$), $U_{\text{Int.}} := a^4 J \sum_{\mathbf{x}_i \neq \mathbf{x}_j} \rho(\mathbf{x}_i) G(\mathbf{x}_i, \mathbf{x}_j) \rho(\mathbf{x}_j)/2$, $U_{\text{Rot.}} := a^2 \sum_{\mathbf{x} \in D} |\tilde{\mathbf{E}}(\mathbf{x})|^2/2J$, and $U_{\text{Harm.}} := L^2 |\bar{\mathbf{E}}_{\text{p}} + 2\pi J \mathbf{w}/L|^2/2J$.

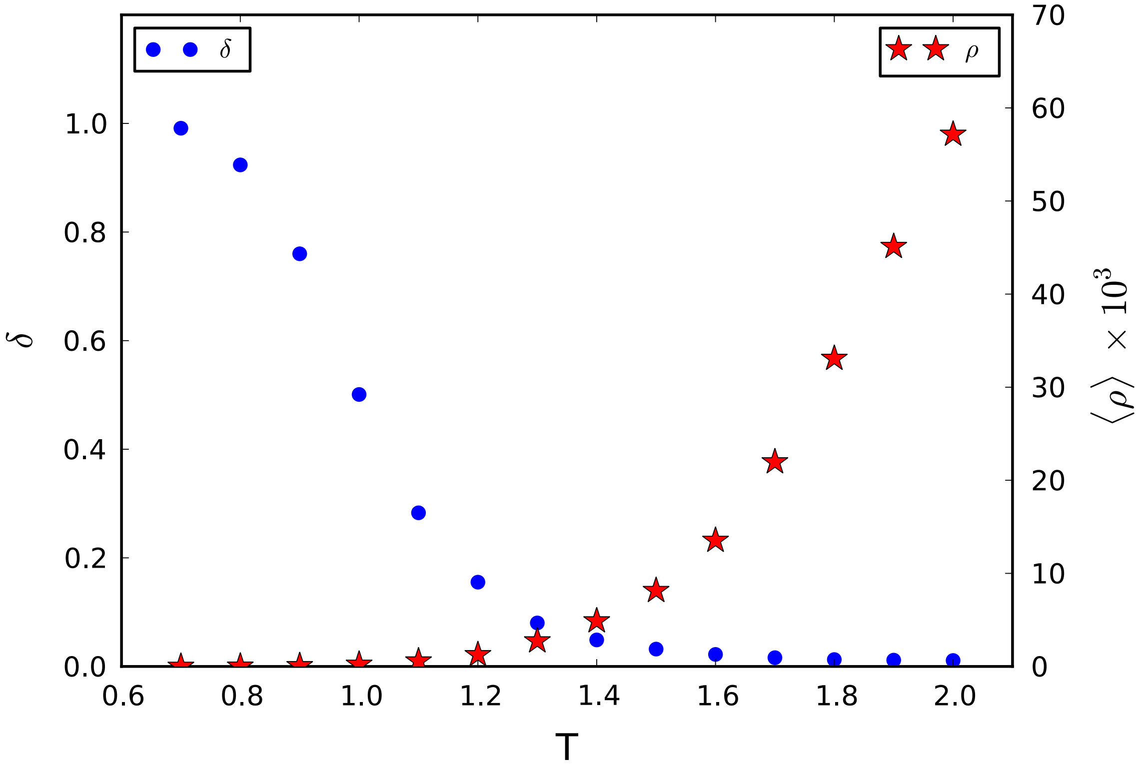

FIGURE 6.2: The normalized field difference δ (Eq. (6.44)) and the thermal average of the emergent-charge density ρ as functions of temperature for an HXY system of linear size $L = 32$. The emergent-charge density is vanishingly small at low temperature, so that the normalized difference tends to $\delta(T \to 0) = \langle|\hat{\mathbf{E}}^{\text{Q}}|\rangle / \langle|\hat{\mathbf{E}}^{\text{Q}}|\rangle = 1$. At high temperature, however, the emergent-charge density becomes relevant, and the normalized difference tends to zero, indicating that the linear solver correctly calculates the emergent field of the quenched system. 10000 quench sweeps were performed before each measurement.

To confirm that the rotational and irrotational components of the emergent field energetically decouple as in Eq. (6.39), the normalized difference δ is defined:

$$\delta(T) := \frac{\langle|\hat{\mathbf{E}}^{\text{Q}} - \hat{\mathbf{E}}^{\text{LS}}|\rangle}{\langle|\hat{\mathbf{E}}^{\text{Q}} + \hat{\mathbf{E}}^{\text{LS}}|\rangle}, \tag{6.44}$$

where $\hat{\mathbf{E}}^{\text{Q}}$ and $\hat{\mathbf{E}}^{\text{LS}}$ are the irrotational components of the emergent field of the system as found by quenching the system and by applying a linear solver to the emergent-charge configuration to solve the Green's function (and then adding the harmonic component of the internal energy of the field), respectively. Fig. 6.2 shows the normalized difference δ and the thermal average of the emergent-charge density ρ as functions of temperature for an HXY system of linear size $L = 32$. The emergent-charge density is vanishingly small at low temperature, so that the normalized difference tends to $\delta(T \to 0) = \langle|\hat{\mathbf{E}}^{\text{Q}}|\rangle / \langle|\hat{\mathbf{E}}^{\text{Q}}|\rangle = 1$. At high temperature, however, the emergent-charge density becomes relevant, and the

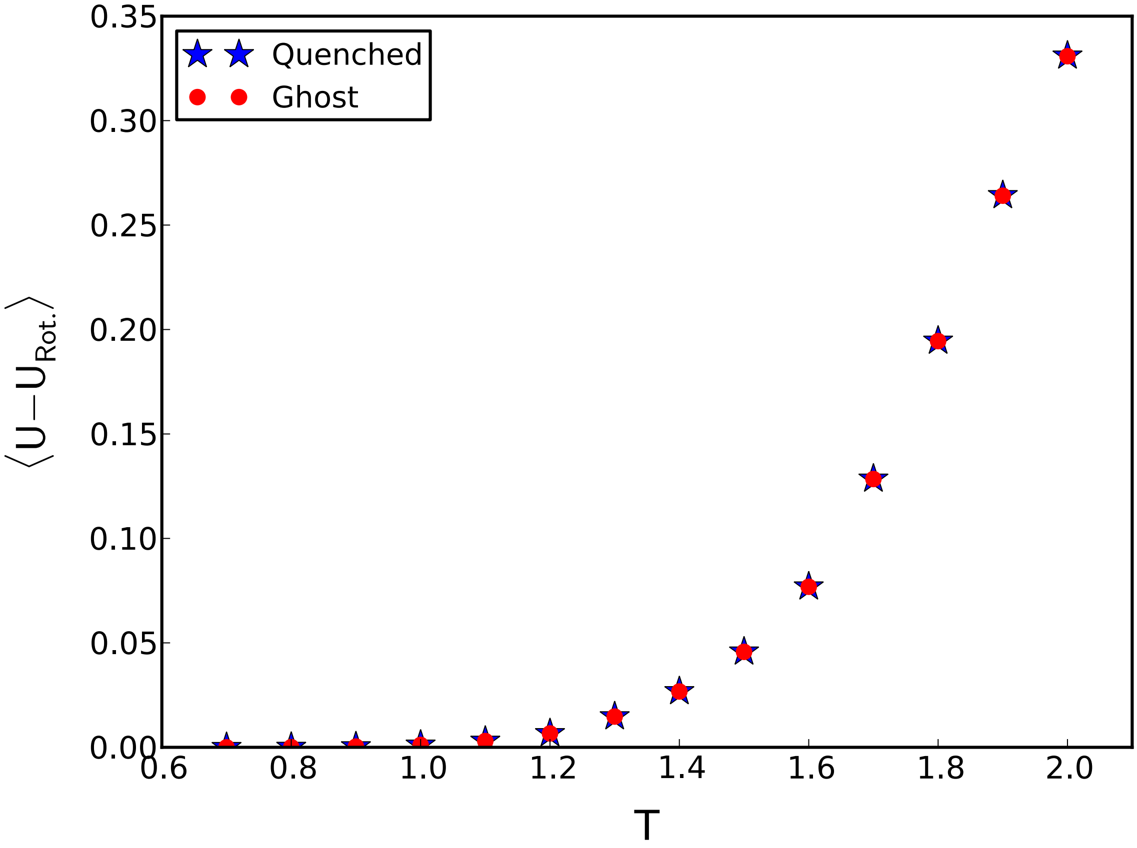

FIGURE 6.3: The thermal average of the internal energy of the irrotational components of the emergent field of the HXY model for a system of linear size $L = 32$ as a function of temperature T as computed by both measuring the energy of the quenched spin system (blue stars) and by employing the linear solver (red circles) ($J = 1$). Fig. 6.3 shows good agreement between the two methods. 10000 quench sweeps were performed before each measurement.

normalized difference tends to zero, indicating that the linear solver correctly calculates the emergent field of the quenched system.

Further to this, Fig. 6.3 shows the thermal average of the internal energy of the irrotational components of the emergent field of the HXY model for a system of linear size $L = 32$ as a function of temperature T as computed by both measuring the energy of the quenched spin system (blue stars) and by employing the linear solver (red circles). Fig. 6.3 shows good agreement between the two methods. The results in Figs. 6.2 and 6.3 confirm the energetic decoupling of the emergent field of the HXY model in Eq. (6.39).

The confirmed field decomposition given by Eq. (6.42) is illustrated in Figs. 6.7 - 6.14, which depict the Helmholtz decomposition of a snapshot of an HXY simulation: Fig. 6.7 shows a snapshot of a 20×20 HXY simulation at $T = 2$ in the spin-field representation; Fig. 6.8 shows Fig. 6.7 transformed to the emergent-field representation; Figs. 6.9 and 6.10 show the polarization and winding components of the total emergent field, respectively; Fig.

6.11 shows the Poisson component of the total field as found via the employment of a linear solver; Fig. 6.12 shows the auxiliary-field component of the total field, found by taking the fields in Figs. 6.9 - 6.11 from the total field; Fig. 6.13 shows the total irrotational component of the total field, found by summing the fields shown in Figs. 6.9 - 6.11; Fig. 6.14 shows the irrotational component, found by quenching the system. The observed agreement between Figs. 6.13 and 6.14 reflects the energetic decoupling of the emergent field of the HXY model for this snapshot.

In the emergent-field representation, the partition function is given by

$$\begin{aligned} Z_{\mathrm{HXY}} = \int \bar{\mathcal{D}}\tilde{\mathbf{e}}\, \delta\left(\sum_{\mathbf{x}\in D} \rho(\mathbf{x})\right) \exp\left[-\frac{a^4\beta J}{2} \sum_{\mathbf{x}_i \neq \mathbf{x}_j} \rho(\mathbf{x}_i) G(\mathbf{x}_i, \mathbf{x}_j) \rho(\mathbf{x}_j)\right] e^{\beta\mu n} \\ \times \exp\left(-\frac{L^2\beta}{2J} |\bar{\mathbf{E}}_{\mathrm{p}} + \frac{2\pi J}{L}\mathbf{w}|^2\right) \prod_{\mathbf{x}\in D} \left[\delta\left(\hat{\boldsymbol{\nabla}} \cdot \tilde{\mathbf{e}}(\mathbf{x})\right)\right] \\ \times \delta\left(\sum_{\mathbf{x}\in D} \tilde{\mathbf{e}}(\mathbf{x})\right) \exp\left[-\frac{a^2\beta}{2J} \sum_{\mathbf{x}\in D} |\tilde{\mathbf{e}}(\mathbf{x})|^2\right], \end{aligned} \tag{6.45}$$

which is derived using a similar method to that used for the Villain model. Here, the divergent core-energy constants enforced by the geometry of the model result in zero contribution to the partition function from non-elementary emergent charges, and the measure $\int \bar{\mathcal{D}}\tilde{\mathbf{e}}$ is defined via

$$\begin{aligned} \int \bar{\mathcal{D}}\tilde{\mathbf{e}} := \prod_{\mathbf{x}\in D} \left[\int_{-\pi-\hat{E}_x(\mathbf{x}+a\mathbf{e}_x/2)}^{\pi-\hat{E}_x(\mathbf{x}+a\mathbf{e}_x/2)} d\tilde{e}_x(\mathbf{x}+a\mathbf{e}_x/2) \int_{-\pi-\hat{E}_y(\mathbf{x}+a\mathbf{e}_y/2)}^{\pi-\hat{E}_y(\mathbf{x}+a\mathbf{e}_y/2)} d\tilde{e}_y(\mathbf{x}+a\mathbf{e}_y/2)\right] \\ \times \sum_{\{\rho(\mathbf{x})\in\{0,\pm 2\pi/a^2\}\}} \sum_{\mathbf{w}\in\mathbb{Z}^2}, \end{aligned} \tag{6.46}$$

where $\hat{\mathbf{E}}$ is the irrotational component of the emergent electric field. The exponents related to the irrotational component of the emergent field cannot be taken outside of the functional integral over the rotational component of the emergent field: the $(-\pi, \pi]$ restriction that constrains the emergent field results in the available configurations of its rotational component being a function of each emergent-charge configuration. Hence, while the rotational and irrotational components of the emergent field energetically decouple, the partition function is not separable into Coulombic and auxiliary components: the HXY model is not a precise emergent MR electrostatic model. At lower temperatures, the partition function approximately decouples because emergent-charge density is low, resulting in approximate emergent MR electrostatics; at higher temperatures, however, increased emergent-charge density restricts the available auxiliary-field configurations such that approximate emergent MR electrostatics breaks down. The $(-\pi, \pi]$ restriction is lifted in the MR electrostatic and

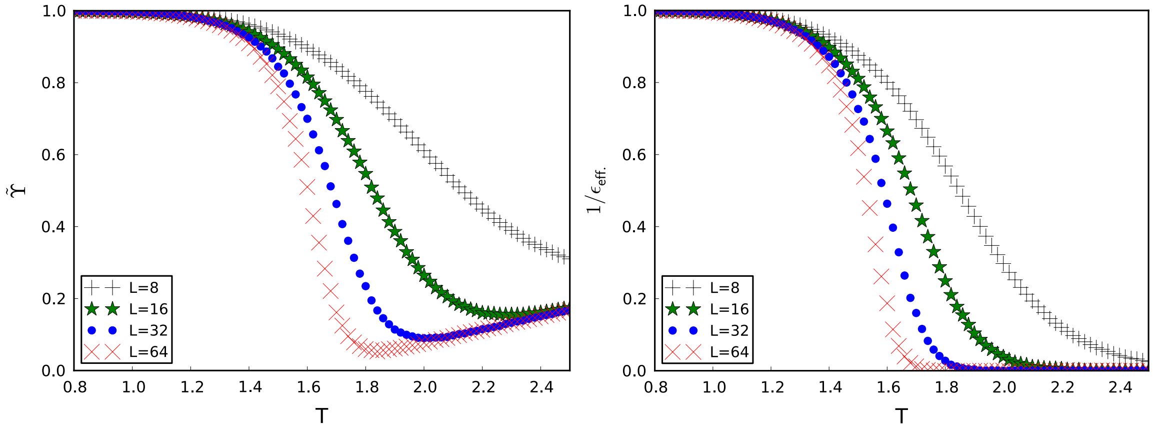

FIGURE 6.4: The finite-size helicity modulus $\tilde{\Upsilon}$ of the HXY model (left) and the inverse effective electric permitivity $\epsilon_{\mathrm{eff.}}^{-1}$ of the two-dimensional Coulomb gas (right) as functions of temperature for systems of linear size $L = 8$, 16, 32 and 64 ($\epsilon_0 = J = 1$). At higher temperatures, the finite-size helicity modulus begins to increase with increasing temperature, thus signalling a breakdown of effective Coulombic physics above the temperature at which the finite-size helicity modulus stops monotonically decreasing. Below this breakdown, the HXY model behaves as an effective Coulomb gas with a temperature-dependent effective electric permittivity. Finally, the finite-size helicity modulus does not reach zero for the system sizes shown: the emergent effective electric permittivity therefore never diverges (for $L = 64$ and below) and the system does not behave as an effective Coulombic conductor at high temperature.

Villain models, since at least one set of microscopic variables is permitted to explore all possible values, resulting in electrostatic Coulombic physics at all temperatures.

In the emergent-field representation, the finite-size helicity modulus of the HXY model is given by

$$\tilde{\Upsilon}(L,T) = J\left(1 - \frac{1}{2}\chi_{\bar{\mathbf{E}}}(L,T)\right), \tag{6.47}$$

as was the case for the Villain model. Again, this expression is intimately related to the emergent charge-charge correlations. It is therefore a measure of the emergent MR physics of the system, as well as its emergent Coulombic conductivity: in this case, emergent Coulombic conductivity corresponds to the emergent charges being able to rearrange to completely cancel the effect of an externally applied global twist in the spin field, which would result in a zero-valued helicity modulus.

Fig. 6.4 shows the helicity modulus $\tilde{\Upsilon}$ of the HXY model (left) and the inverse effective electric permittivity $\epsilon_{\mathrm{eff.}}^{-1}$ of the two-dimensional Coulomb gas (right) as functions of temperature for systems of linear size $L = 8$ to 64. At lower temperatures, the helicity modulus displays the same monotonic behaviour as the inverse effective electric permittivity; above $T = 1.8$, however, the helicity modulus transitions into a monotonically increasing regime, never reaching zero.

The first observation shows that the HXY model statistically behaves as an effective Coulomb gas with a temperature-dependent effective electric permittivity in the low-temperature region: one can pick a temperature of the HXY model and compare the helicity modulus of that temperature with the inverse effective electric permittivity of the Coulombic system to find the effective Coulombic temperature of the magnetic system. The second observation shows that the effective Coulombic physics breaks down in the high-temperature region of monotonically increasing behaviour: this confirms the breakdown of effective emergent MR electrostatics at high temperatures predicted by the non-decoupling of the partition function given by Eq. (6.45). Finally, a diverging effective electric permittivity is the key signature of conductivity in Coulombic systems, hence, the observation that the helicity modulus does not reach zero for the system sizes presented shows that the system does not behave as an effective emergent Coulombic conductor for systems of linear size $L = 64$ and below. This is a result of the emergent charges being constrained by the spin waves in such a way that, statistically, they cannot rearrange to completely cancel the effect of an externally applied global twist in the spin field. The absence of this signature of emergent Coulombic conductance is due to the entropy of the spins being lower for emergent-charge configurations that are able to cancel the global twists than for those that cannot.

6.2.3 The 2dXY Model

The partition function of the XY model is given by

$$Z_{\mathrm{XY}} = \int \bar{\mathcal{D}}\varphi \exp\left[\beta J \sum_{\langle \mathbf{x},\mathbf{x}' \rangle} \cos(\varphi(\mathbf{x}) - \varphi(\mathbf{x}'))\right], \tag{6.48}$$

whose exponent can be expanded to quadratic order for small spin differences, as shown in Section 2.3.2. Notice that the modular symmetry is enforced via the same mechanism as that of the HXY model, but implicitly by the cosine function, in this case. Again, the emergent electric field is defined as in Eq. (6.24), resulting in an emergent Gauss' law equivalent to Eq. (6.25). The emergent electric charges of the XY model are topological defects in both the spin-difference field $\varphi(\mathbf{x} + a\mathbf{e}_i) - \varphi(\mathbf{x})$ and the emergent electric field $\mathbf{E}$.

The anharmonic terms in the Hamiltonian of the XY model result in a partition function that is not separable into emergent Coulombic and auxiliary-field components at any temperature. The XY model is therefore not a precise emergent MR electrostatic model. The helicity modulus, however, measures the response of the system to an externally applied global twist in the spin field, and is therefore a measure of the ability of the emergent charges to cancel the twist. Fig. 6.5 shows the helicity modulus $\tilde{\Upsilon}$ of the XY model as a

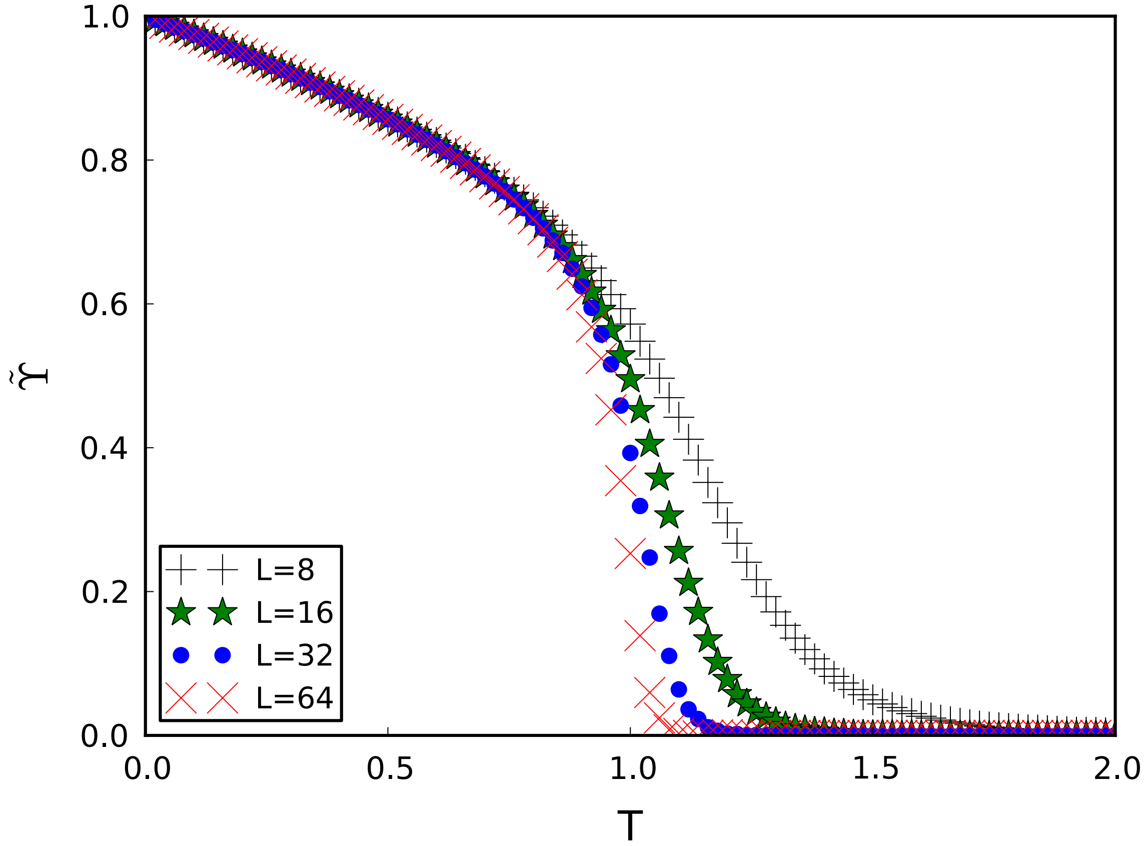

Figure 6.5: The finite-size helicity modulus $\tilde{\Upsilon}$ of the XY model as a function of temperature for systems of linear size $L = 8$, 16, 32 and 64 ($J = 1$). The helicity modulus is a monotonically decreasing function of temperature, reaching zero in the high-temperature phase of the BKT transition. In this phase, the XY model therefore behaves as an emergent conductor.

function of temperature for systems of linear size $L = 8$ to 64. The helicity modulus is a monotonically decreasing function of temperature, reaching zero at higher temperatures.

Although the XY model is not precisely an emergent Coulomb gas, the connection between the two systems is a very close one [3, 4, 39]. The definitions of the helicity modulus of the XY model (Eq. (2.110)) and the inverse effective electric permittivity of the Coulomb gas (Eq. (3.19)) are with respect to analogous perturbations in their (emergent) electric-field representations, leading to analogous monotonic behaviour in the helicity modulus of the XY model as that observed in the inverse effective electric permittivity of the Coulomb gas. This indicates that the XY model admits emergent electrostatics to a good approximation, a standard result of the literature [3, 4, 39]. In addition, RG calculations [4, 9, 39] show that these systems are in the same universality class at the BKT transition. In the high-temperature phase, the emergent charges of the XY model are able to rearrange to completely cancel the effect of an externally applied global twist in the spin field, signalling emergent conductance. Compared to the HXY model, the anharmonic terms in the Hamiltonian reduce the energy of such emergent-charge configurations so that their reduced spin entropy cannot increase the free-energy barrier to their formation to prohibitive values.

6.2.4 Spin-update Mechanics of the XY Models

The mechanics of the spin updates of the XY models (that is, the HXY and XY models) are now considered. Spin-wave updates are entirely equivalent to spin-wave updates in the Villain model; an emergent-charge update is, however, a two-step process, and is the result of a particular type of spin update. As shown in Fig. 6.6, if a spin update results in the difference between the value of the spin and the value of an adjacent spin leaving the set $(-\pi, \pi]$, the consequential modular update causes the emergent charge to hop across to the relevant adjacent charge site. This two-step process is equivalent to the superposition of a charge-hop and an auxiliary-field update in the MR electrostatic model, and is due to the emergent charges being topological defects in the spin-difference field $\varphi(\mathbf{x} + a\mathbf{e}_i) - \varphi(\mathbf{x})$.

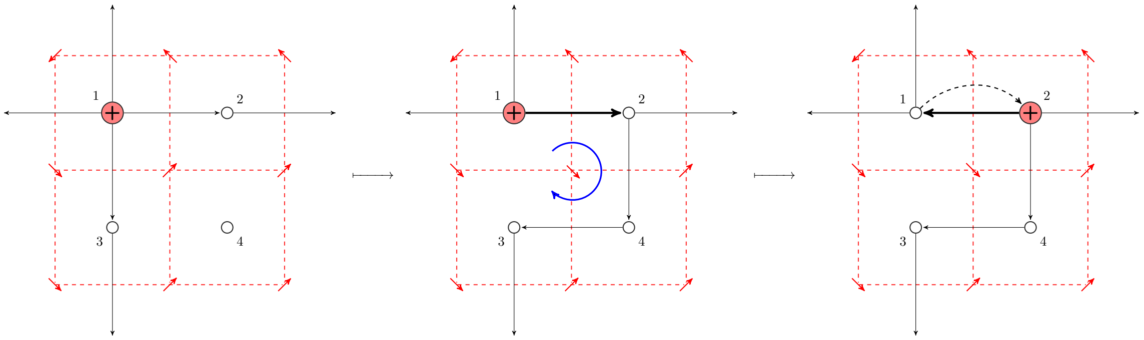

Figure 6.6: A vortex-hop update in the XY models: The spin at the centre of the diagram has its value decreased by an amount $\pi/2 + \delta$ (where we consider the small, positive δ to ensure that the relevant spin difference leaves the set $(-\pi, \pi]$). Initially, we observe a spin update of the same form as that of the Villain model. This is followed by an intrinsic modular-symmetry update: the emergent field experiences the equivalent of an MR charge-hop update, with $E_{12} + \pi J/2 + \delta J \mapsto E_{12} + \pi J/2 + \delta J - 2\pi J$.

6.2.5 Global Twists in the Spin Representation of the XY Models

As shown in Chapter 5, fluctuations in the winding component of the electric field of the two-dimensional Coulomb gas signal the high-temperature phase of the BKT transition. In the Villain model, such fluctuations arise via the same mechanism as that of the MR electrostatic model; in the XY models, however, the subtle difference with respect to the mechanics of the emergent-charge updates causes global twists in the spin field to map on to emergent winding fields.

Fig. 6.15 shows an emergent-charge pair, which has been created out of the vacuum but with an idealized spin configuration, in an HXY or XY system. The pair unbind, wind around the torus in the x direction, and, finally, annihilate one another in Figs. 6.16 – 6.18. The remnant MEC due to this sequence of events is shown in Fig. 6.19: this spin configuration is equivalent to a global twist in the y direction of the spin system. This spin configuration is mapped on to the emergent-field representation in Fig. 6.20 thus showing the equivalence between global twists in the spin representation and non-trivial topological sectors in the emergent-field representation.

Since the XY models admit an emergent electric field of the form of the lattice electric fields of the MR electrostatic model, the twists in the spin representations seen here correspond to the winding of electrical charges around the torus in the Coulomb gas. The topological-sector fluctuations observed in the Coulomb gas in the high-temperature phase of the BKT transition (Chapter 5) therefore correspond to twist fluctuations in the spin field of the XY models. This elucidation of the equivalence between twist fluctuations in the spin-field representation and topological-sector fluctuations in the emergent-field representation shows the utility of representing the XY models with the quasi-MR electrostatic model presented here: the result of Chapter 5 is now seen to have relevance to real magnetic systems. The topological-sector fluctuations of Chapter 5 could be observable in ultrathin ferromagnetic metallic films [61], magnetic Langmuir-Blodgett films [62, 63], or ferromagnetic films with a 'washer' geometry (PBCs in one direction).

6.3 The Harmonic Model

It is instructive to consider the purely harmonic planar-spin model, the Villain and HXY models with the modular periodicity removed. From this discussion, it is now clear as to why no BKT transition occurs in this spin model: the lack of modular periodicity results in the model having no update analogous to the charge-hop updates of the MR electrostatic model, so that the irrotational component of the emergent electric field returns zero for all field bonds at all temperatures.

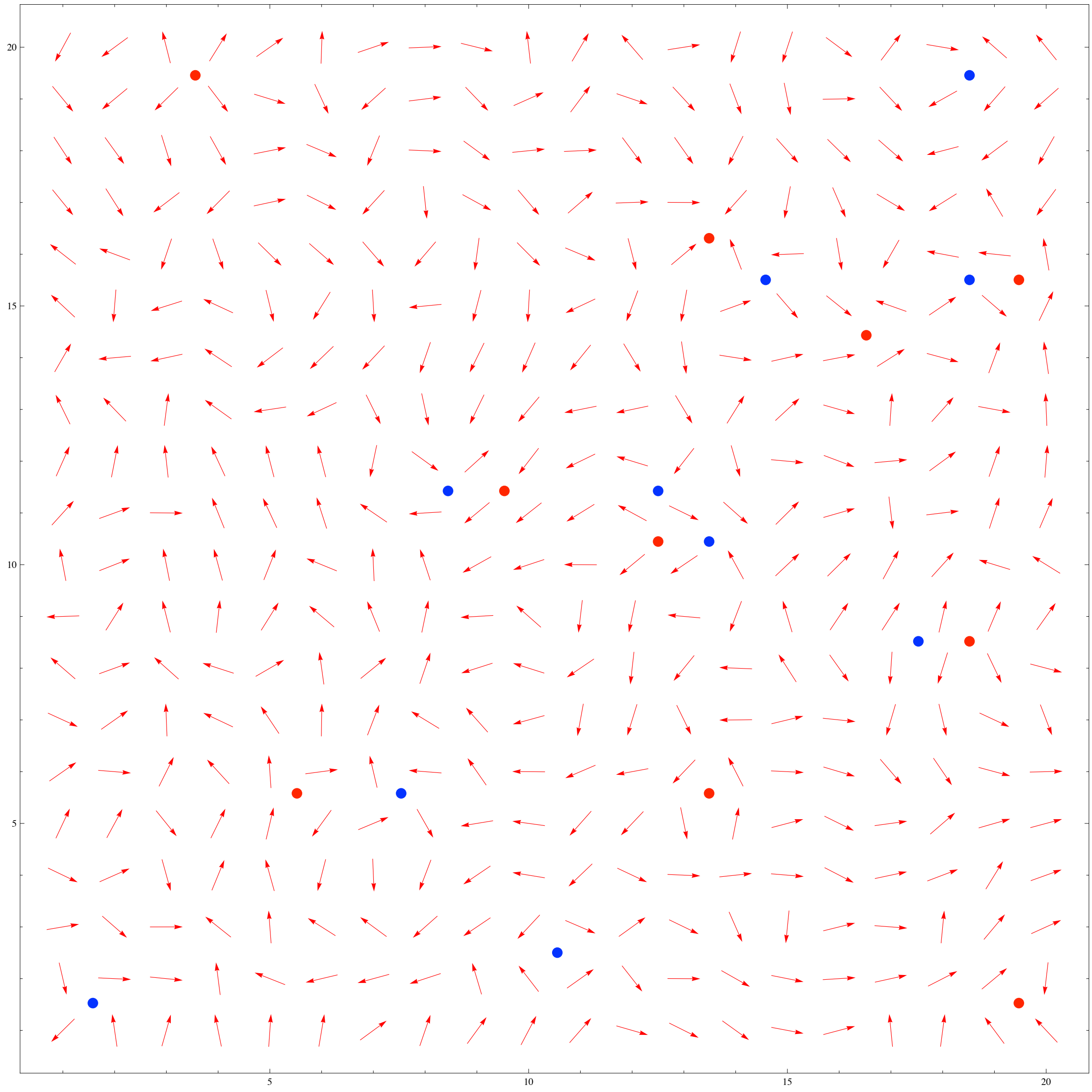

FIGURE 6.7: The spin representation of a snapshot of a 20×20 HXY simulation at $T = 2J/k_{\mathrm{B}}$. Red circles are positive emergent charges; blue circles are negative emergent charges.

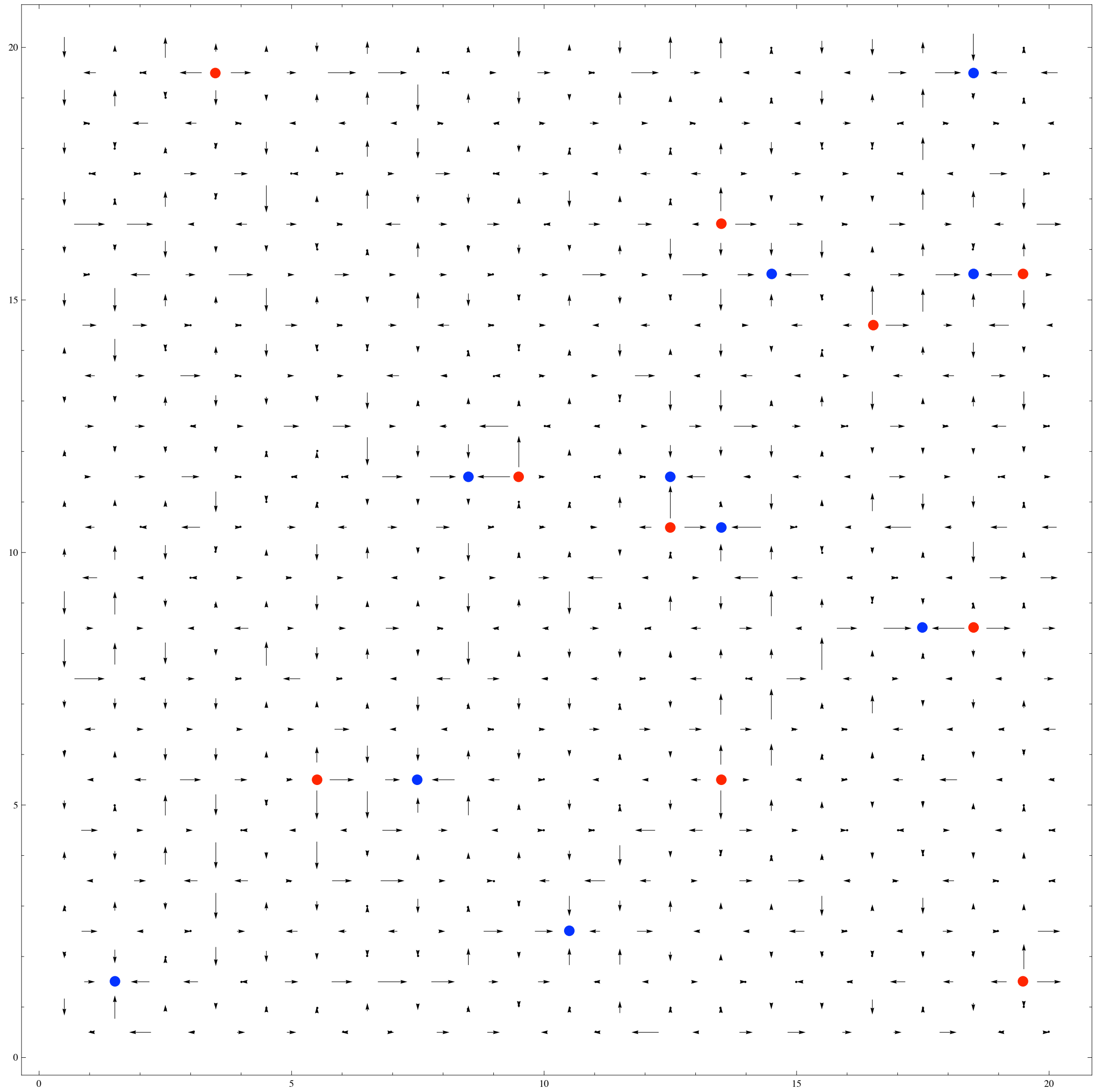

FIGURE 6.8: The emergent-field representation of Fig. 6.7. The absolute values of the field lines are relative within each figure. Red circles are positive emergent charges; blue circles are negative emergent charges.

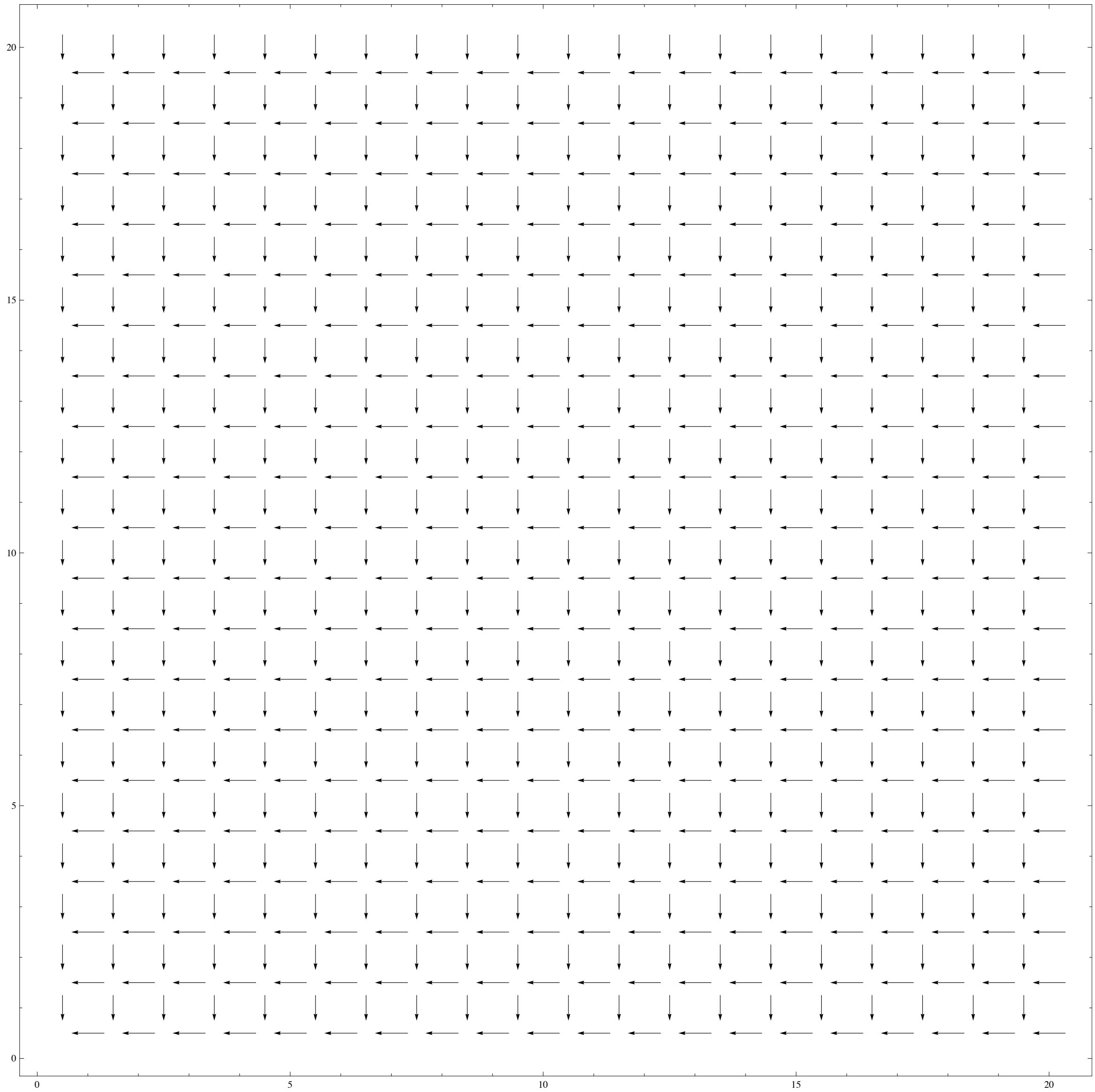

FIGURE 6.9: The polarization component of $\bar{\mathbf{E}}$ of the field configuration in Fig. 6.8, given by $\bar{\mathbf{E}}_{\mathrm{p}} = -2\pi(9,\, 7)/L$. The absolute values of the field lines are relative within each figure.

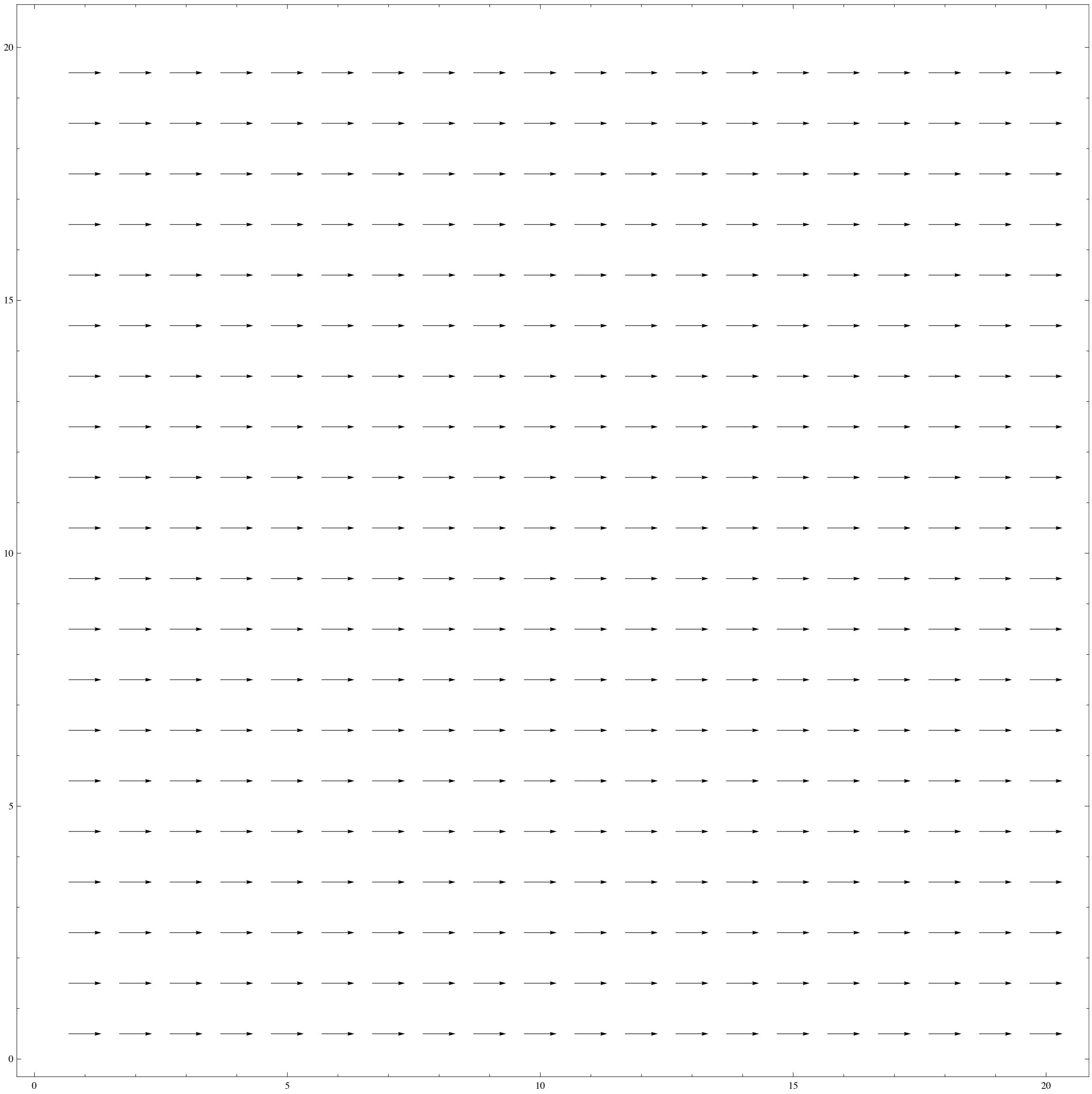

FIGURE 6.10: The winding-field component of $\bar{\mathbf{E}}$ of the field configuration in Fig. 6.8. The system's topological sector is given by $\mathbf{w} = (1,\, 0)$. The absolute values of the field lines are relative within each figure.

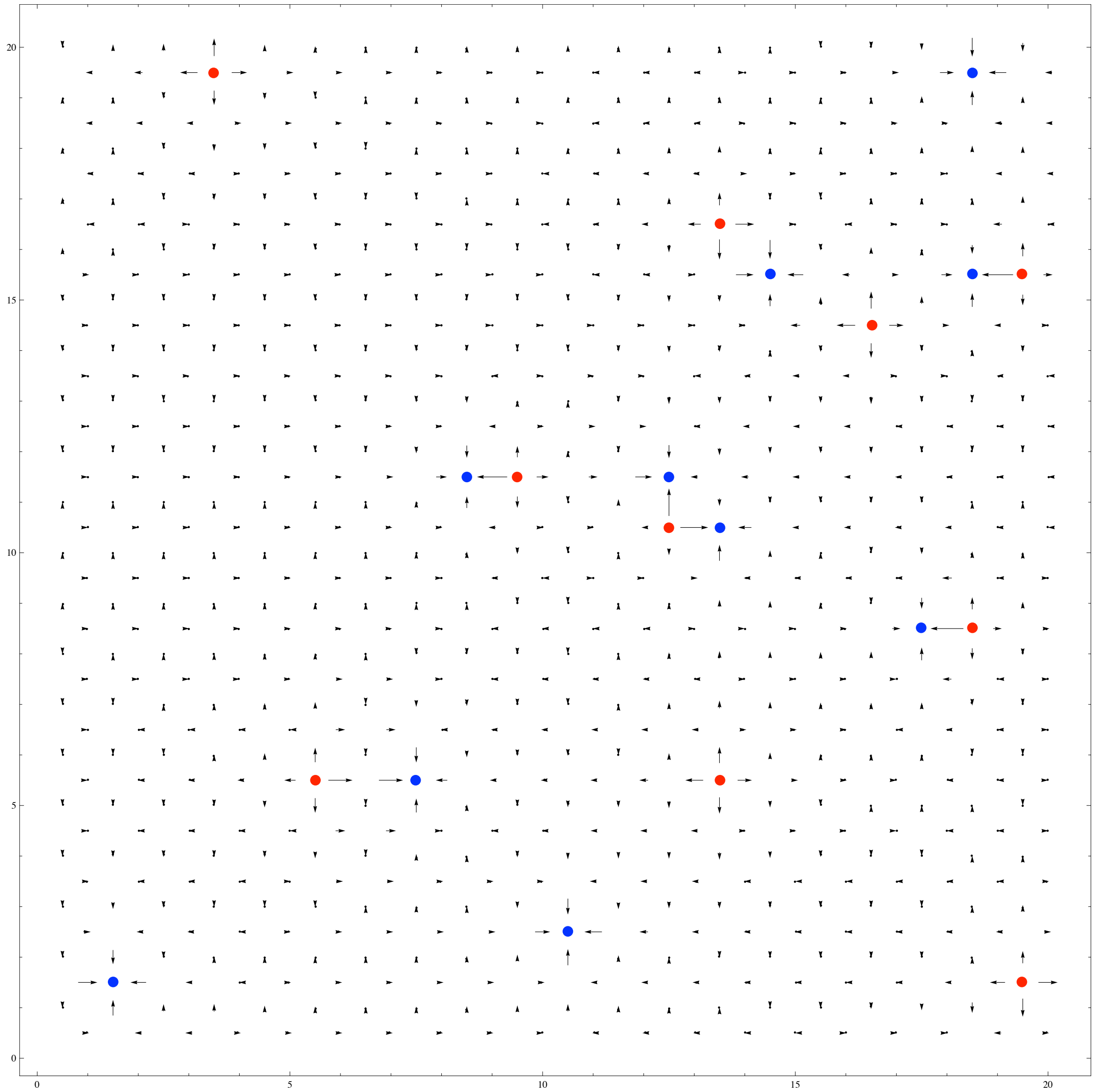

FIGURE 6.11: The Poisson component $-\tilde{\boldsymbol{\nabla}}\phi$ of the field configuration in Fig. 6.8 as found via the employment of a linear solver. The absolute values of the field lines are relative within each figure. Red circles are positive emergent charges; blue circles are negative emergent charges.

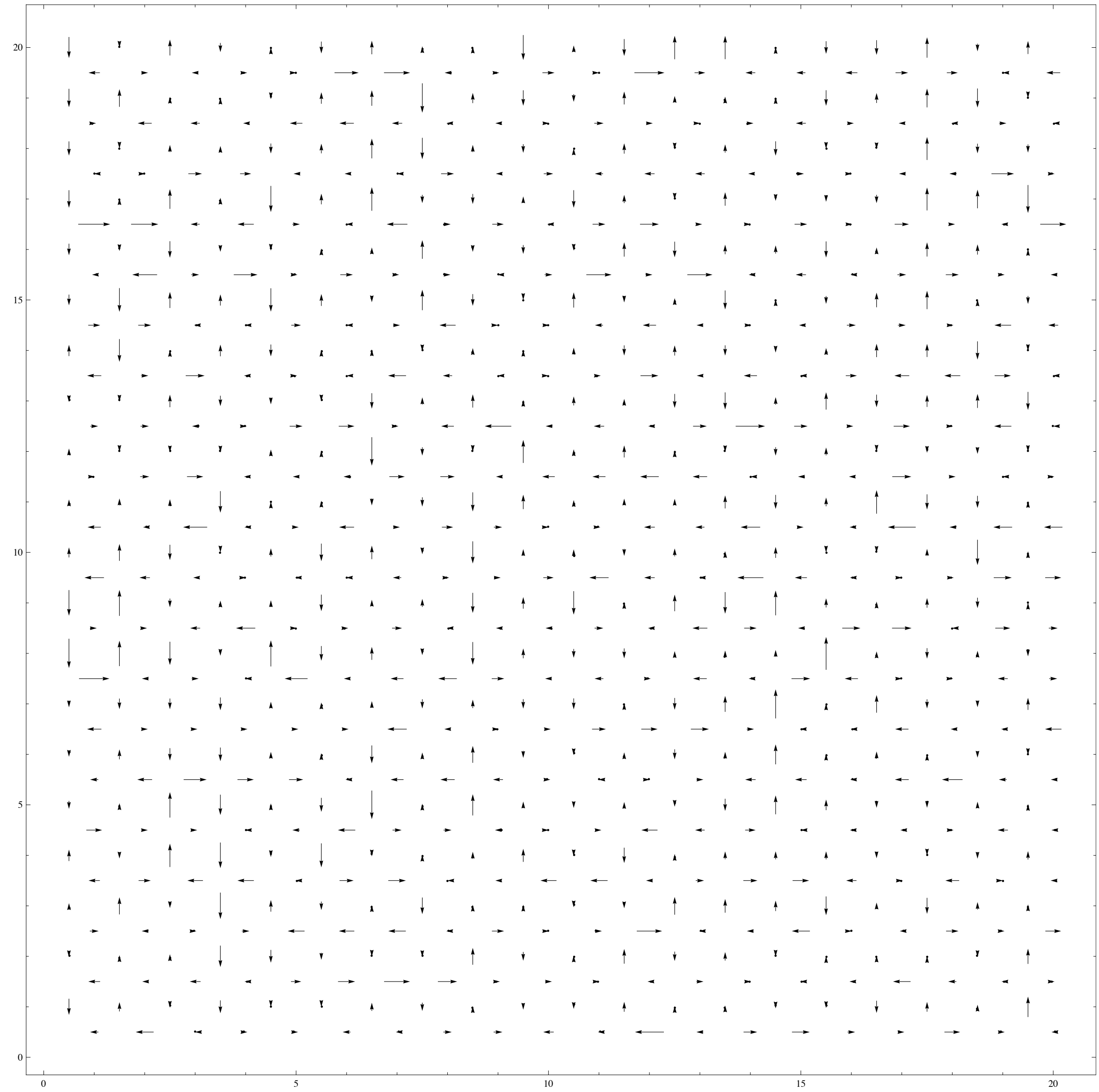

FIGURE 6.12: The auxiliary-field component $\tilde{\mathbf{E}}$ of the total field configuration in Fig. 6.8. The absolute values of the field lines are relative within each figure.

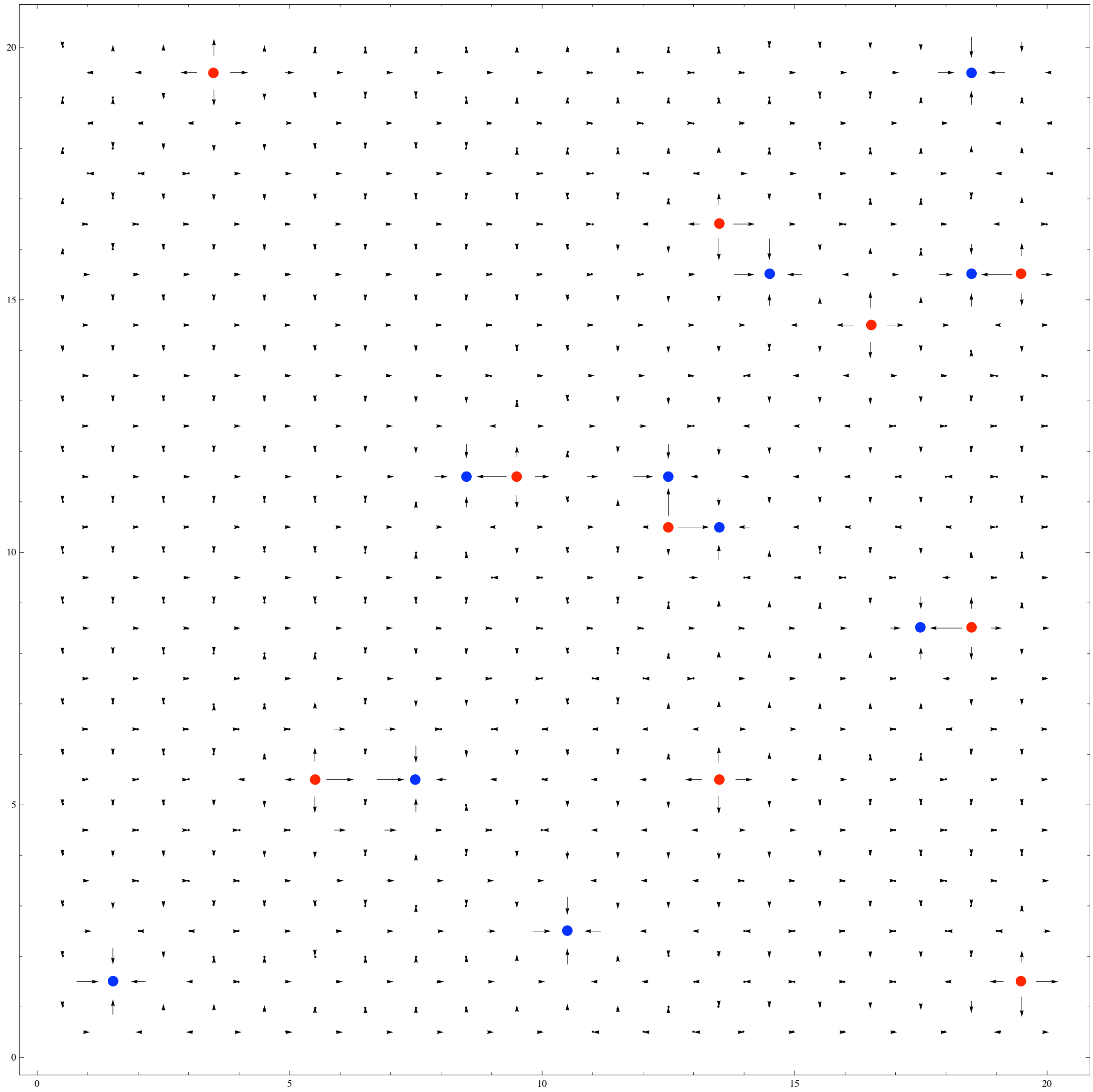

FIGURE 6.13: The electrostatic component $\bar{\mathbf{E}} - \tilde{\boldsymbol{\nabla}}\phi$ of the field configuration in Fig. 6.8, found by applying the linear solver to the topological-defect configuration in Fig. 6.8 (and adding the harmonic mode of the emergent field in Figs. 6.9 and 6.10). The absolute values of the field lines are relative within each figure. Red circles are positive emergent charges; blue circles are negative emergent charges.

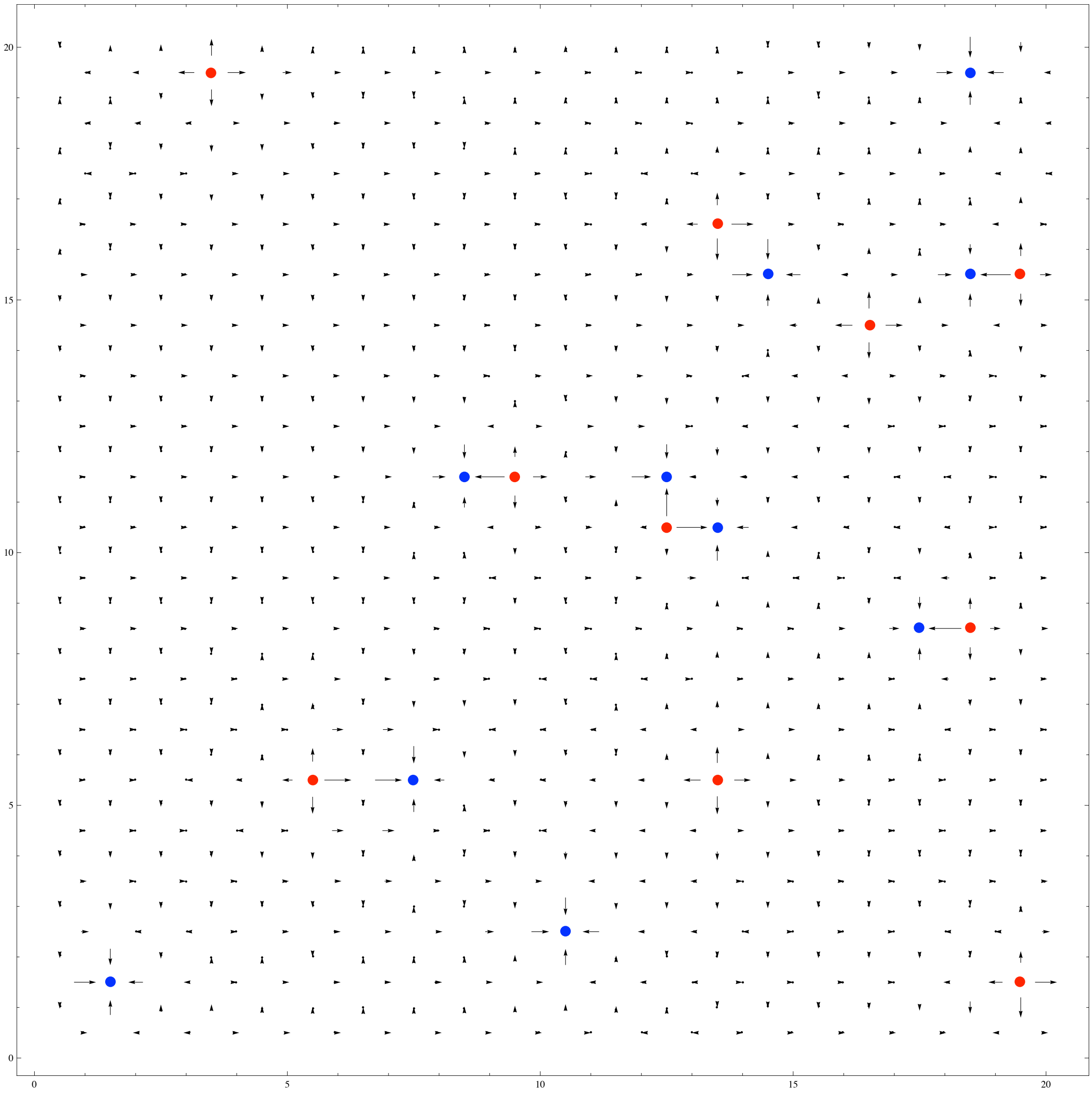

FIGURE 6.14: The electrostatic component $\bar{\mathbf{E}} - \tilde{\boldsymbol{\nabla}}\phi$ of the field configuration in Fig. 6.8, found by quenching the HXY system. The absolute values of the field lines are relative within each figure. Red circles are positive emergent charges; blue circles are negative emergent charges.

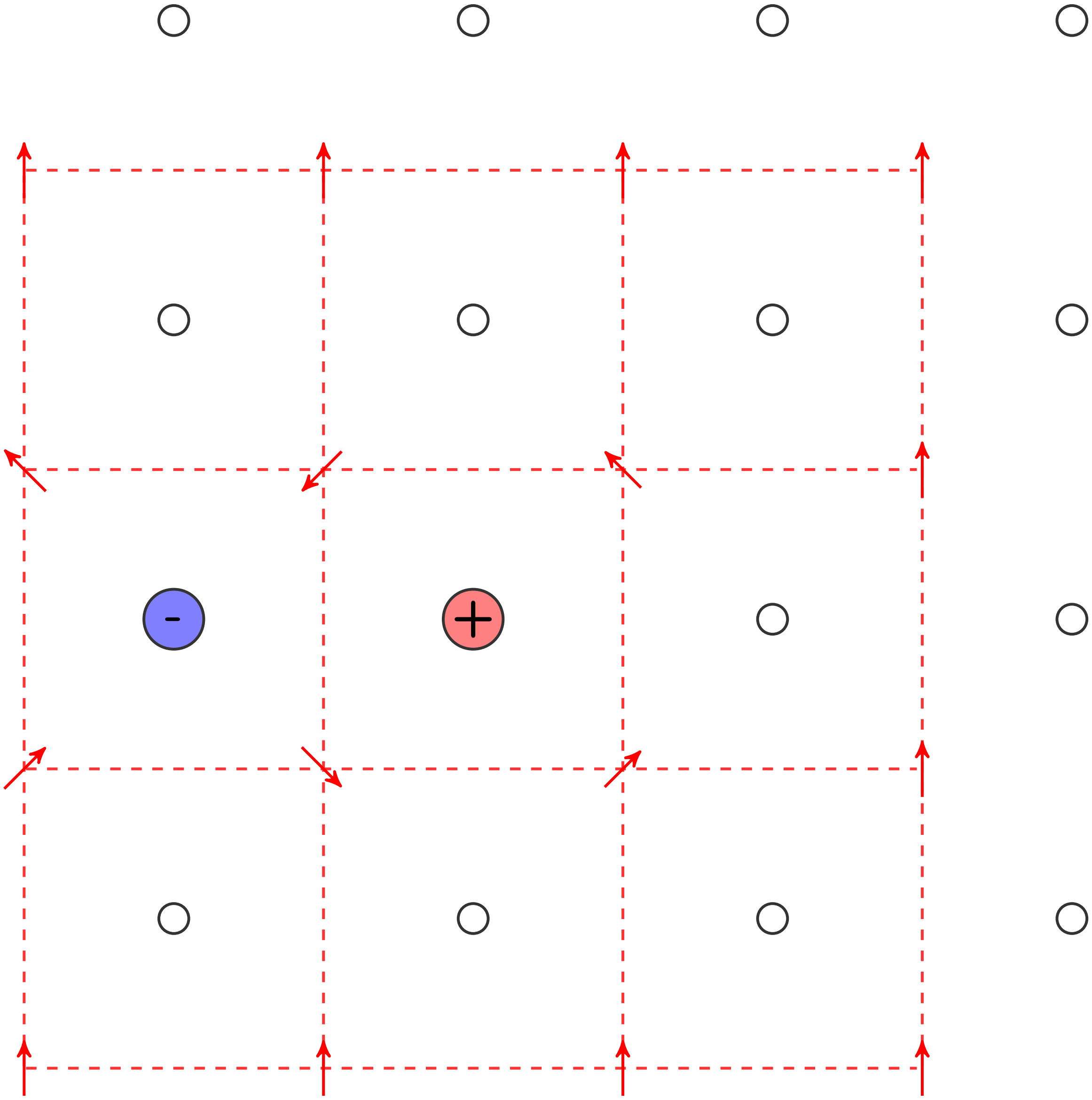

FIGURE 6.15: An emergent-charge pair in the XY models with an idealized spin configuration.

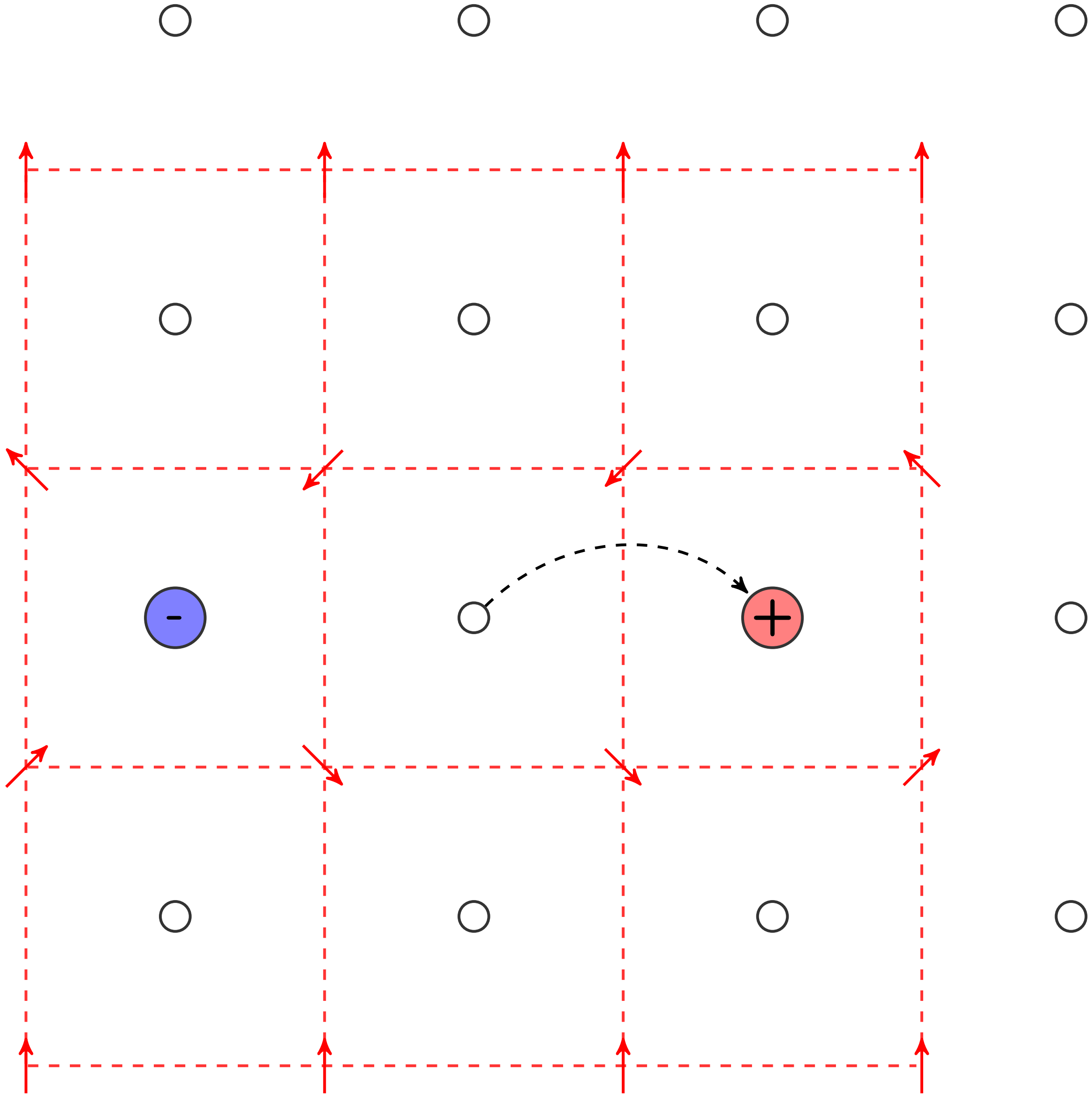

Figure 6.16: The positive emergent charge has hopped to the right.

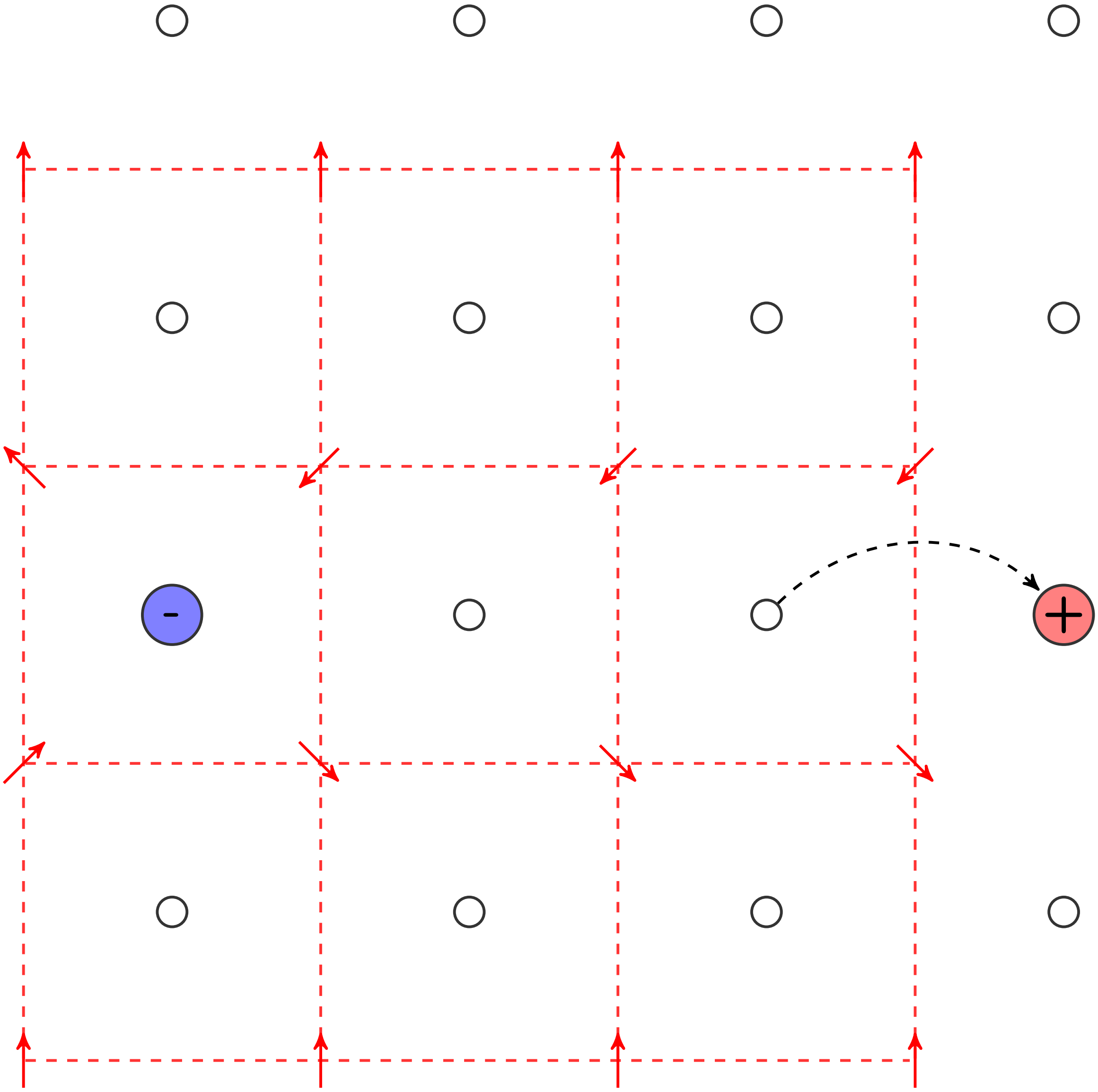

Figure 6.17: The emergent charge has hopped to the right again.

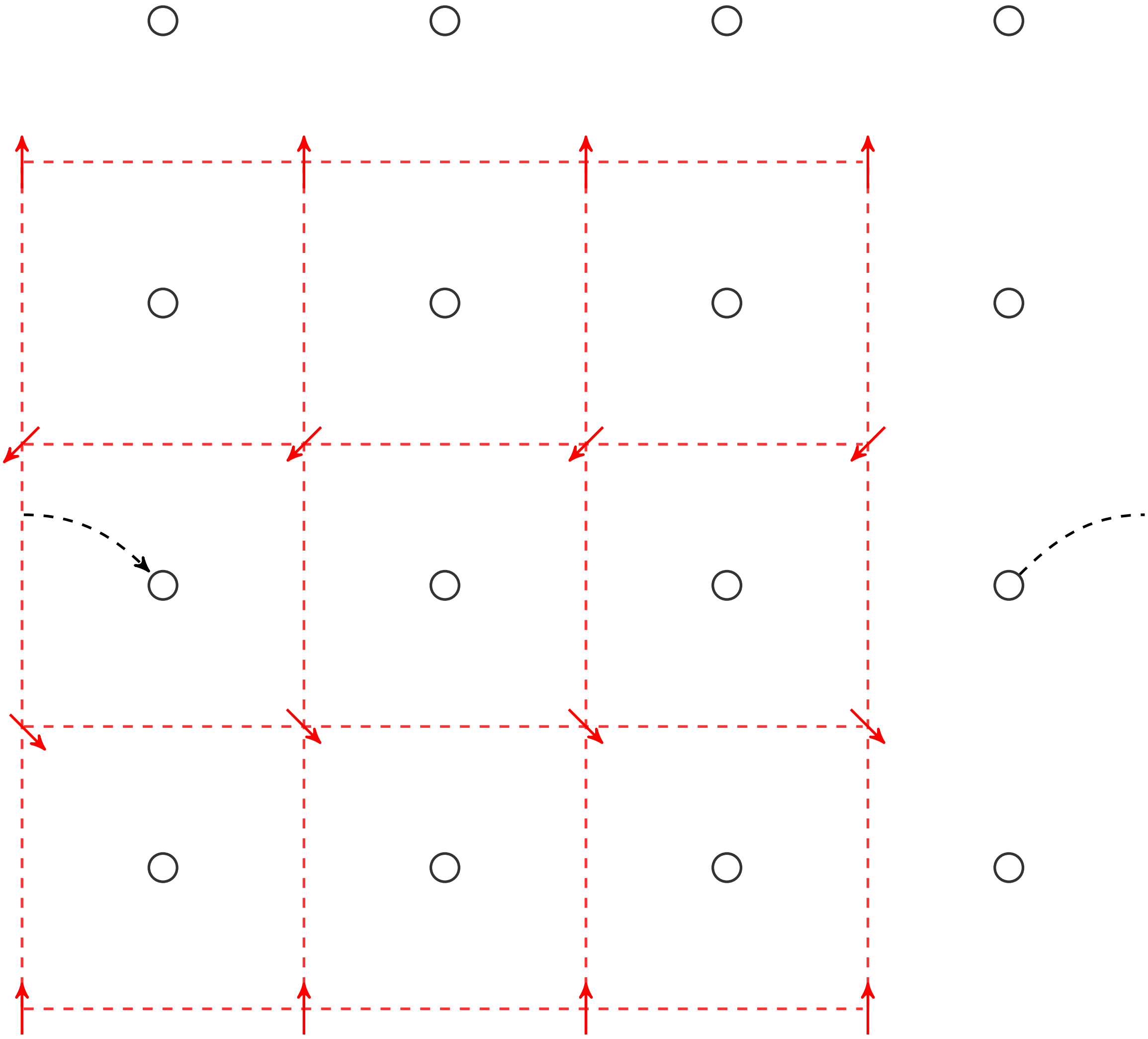

FIGURE 6.18: The emergent charges have annihilated.

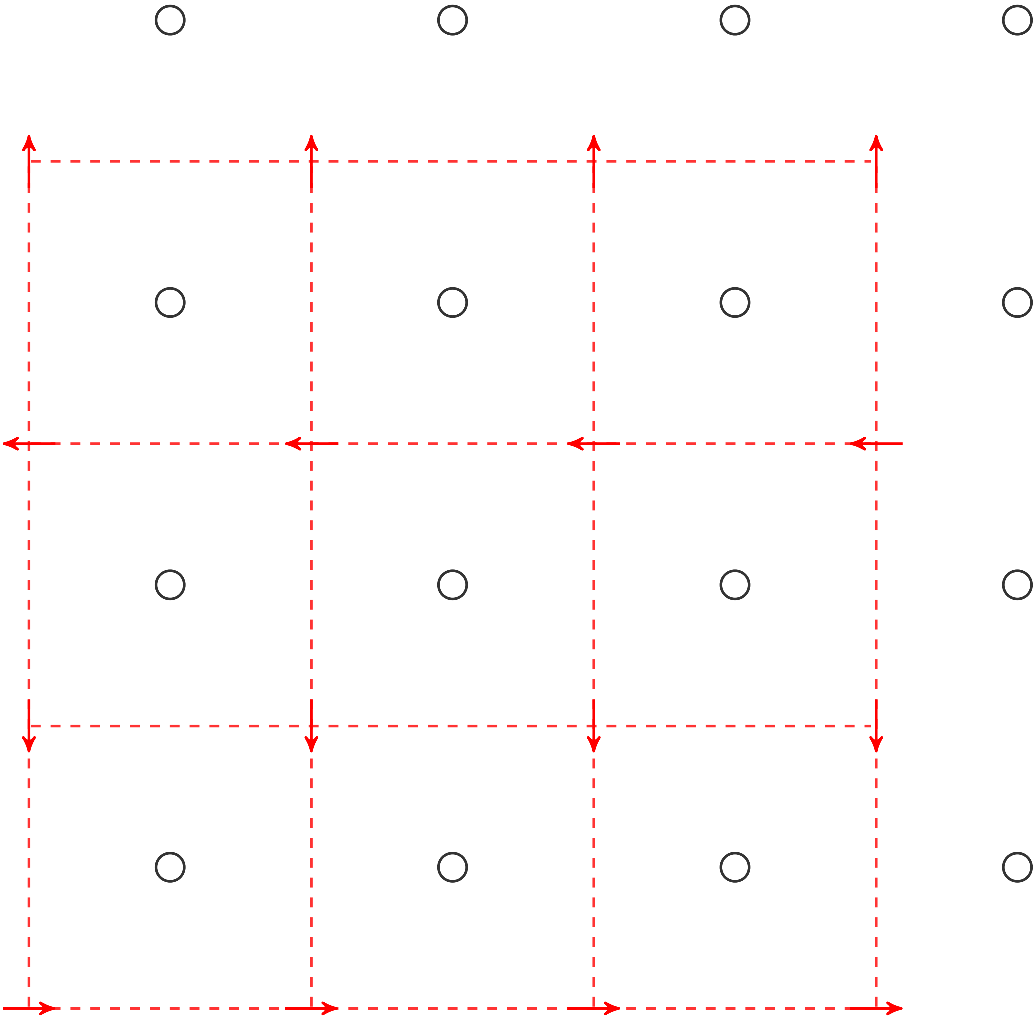

FIGURE 6.19: The MEC corresponding to Fig. 6.18.

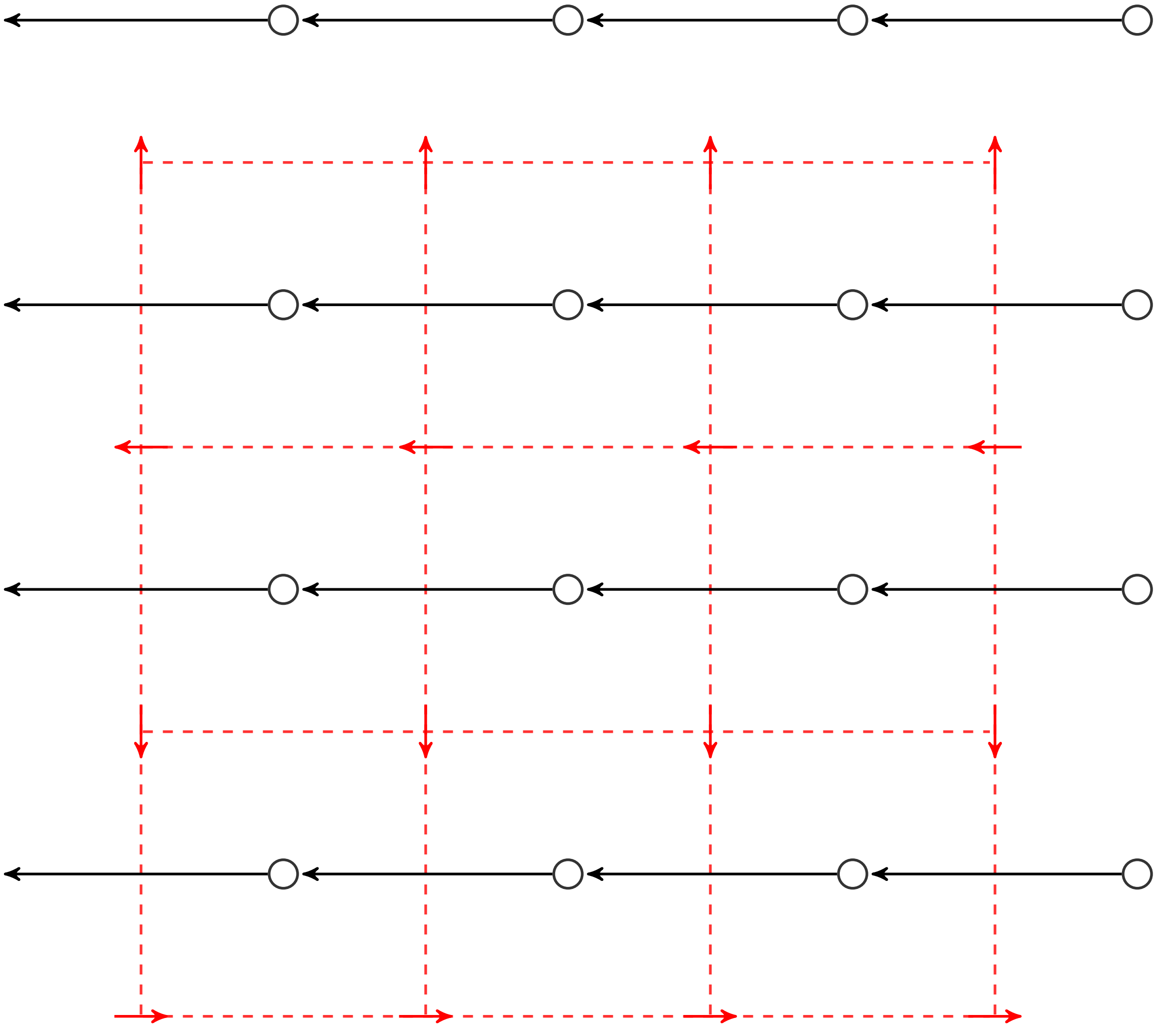

Figure 6.20: Fig. 6.19 with the emergent field shown in black.

Chapter 7

Bramwell-Holdsworth Theory in General BKT Systems

This thesis has been based around the emergent electrostatics of XY-type spin models. In this chapter, a final link between the harmonic-mode susceptibility of the Coulombic system and the magnetization of the magnetic system is presented. From this, it follows that BH theory applies to the non-magnetic system, and is in fact measurable in superfluid ^{4}He films.

7.1 Effective Spin Stiffness

To begin, instead of employing the BH ansatz (Eq. (2.135)), the partition function of the XY-type spin model in question is identified with the effective partition function that was defined in Eq. (2.115). This makes intuitive sense since the object $(\tilde{K}_{\text{eff.}}(L,T) - K(T))$ describes the deviation of the the finite-size system from harmonic spin-wave behaviour. Following the same method as that in Section 2.3.5, the magnetization of the system is then given by

$$\langle m \rangle = \left(\frac{1}{cN} \right)^{1/8\pi \tilde{K}_{\text{eff.}}(L,T)} \tag{7.1}$$

for all temperatures. The BH ansatz amounts to asserting that replacing $\tilde{K}_{\text{eff.}}$ with $K_{\text{eff.}}$ in the exponent of the above expression for $T \leq T^*(L)$ should be a limitingly good approximation in the thermodynamic limit; however, numerical and experimental evidence (see Section 2.5) suggests that this is approximately true at finite system size. We recall that these two objects are related by Eq. (2.116):

$$K_{\text{eff.}}(T) := \lim_{L\to\infty}\left[\tilde{K}_{\text{eff.}}(L,T)\right]. \tag{7.2}$$

Analysis is restricted to the Villain model, since this system is analytically tractable. Eq. (7.1) results from performing a spin-wave analysis on the effective partition function $Z_{\text{eff.}}$ (Eq. (2.115)), which is valid since the identification $Z \equiv Z_{\text{eff.}}$ is made (throughout, all partition functions and thermal averages are for the Villain model). A similar analysis is now performed on the left-hand side of the identification $Z \equiv Z_{\text{eff.}}$.

The Hamiltonian of the Villain model is expanded to give

$$\beta H = \frac{\beta J}{2}\sum_{\mathbf{x},\mathbf{x}'}\varphi(\mathbf{x})\tilde{G}(\mathbf{x},\mathbf{x}')\varphi(\mathbf{x}') + 2\pi\beta J\sum_{\mathbf{x}}\theta(\mathbf{x})\Delta s(\mathbf{x}) + 2\pi^2\beta J\sum_{\langle\mathbf{x},\mathbf{x}'\rangle}s(\mathbf{x},\mathbf{x}')^2, \tag{7.3}$$

where $\Delta s(\mathbf{x}) := \sum_{i\in\{x,y\}}\Delta s_i(\mathbf{x})$, with $\Delta s_i(\mathbf{x}) := s_i(\mathbf{x}+a\mathbf{e}_i/2) - s_i(\mathbf{x}-a\mathbf{e}_i/2)$ and $s_i(\mathbf{x}+a\mathbf{e}_i/2) := s(\mathbf{x},\mathbf{x}')$. Following a similar method to that used in Section 2.3.5, the partition function can then be written as

$$Z = \sum_{\{s(\mathbf{x},\mathbf{x}')\in\mathbb{Z}\}}\int\bar{\mathcal{D}}\varphi\exp\left(-\frac{1}{2}\boldsymbol{\varphi}^T\mathbf{A}\boldsymbol{\varphi} - \mathbf{j}^T\boldsymbol{\varphi}\right)\exp\left(-2\pi^2\beta J\sum_{\langle\mathbf{x},\mathbf{x}'\rangle}s(\mathbf{x},\mathbf{x}')^2\right), \tag{7.4}$$

where

$$\mathbf{j} := 2\pi\beta J\begin{pmatrix}\Delta s(\mathbf{x}_1)\\ \vdots \\ \Delta s(\mathbf{x}_N)\end{pmatrix} \tag{7.5}$$

is the modular current. The thermal average of any scalar function f can now be expressed as

$$\begin{aligned}\langle f(\boldsymbol{\varphi})\rangle :=& \frac{1}{Z}\sum_{\{s(\mathbf{x},\mathbf{x}')\}}\int\bar{\mathcal{D}}\varphi f(\boldsymbol{\varphi})\exp\left(-\beta H\right) && (7.6)\\ =& \frac{1}{Z}\sum_{\{s(\mathbf{x},\mathbf{x}')\}}\int\bar{\mathcal{D}}\varphi f(\boldsymbol{\varphi})\exp\left(-\frac{1}{2}\boldsymbol{\varphi}^T\mathbf{A}\boldsymbol{\varphi} - \mathbf{j}^T\boldsymbol{\varphi}\right)\exp\left(-2\pi^2\beta J\sum_{\langle\mathbf{x},\mathbf{x}'\rangle}s(\mathbf{x},\mathbf{x}')^2\right) && (7.7)\\ =& \frac{1}{Z}\sum_{\{s(\mathbf{x},\mathbf{x}')\}}\int\bar{\mathcal{D}}\varphi f\left(-\frac{\delta}{\delta\mathbf{b}}\right)\exp\left(-\frac{1}{2}\boldsymbol{\varphi}^T\mathbf{A}\boldsymbol{\varphi}\right)\exp\left[-(\mathbf{j}^T+\mathbf{b}^T)\boldsymbol{\varphi}\right] \\ & \times\exp\left(-2\pi^2\beta J\sum_{\langle\mathbf{x},\mathbf{x}'\rangle}s^2_{\mathbf{x},\mathbf{x}'}\right)\Bigg|_{\mathbf{b}=\mathbf{0}} && (7.8)\end{aligned}$$

$$
\begin{aligned}
=&\frac{(2\pi)^{N/2}}{Z\sqrt{\det \mathbf{A}}}\sum_{\{s(\mathbf{x},\mathbf{x}')\}} f\left(-\frac{\delta}{\delta \mathbf{b}}\right)\exp\left[\frac{1}{2}(\mathbf{j}^T+\mathbf{b}^T)\mathbf{A}^{-1}(\mathbf{j}+\mathbf{b})\right]\\
&\times\exp\left(-2\pi^2\beta J\sum_{\langle\mathbf{x},\mathbf{x}'\rangle}s(\mathbf{x},\mathbf{x}')^2\right)\Bigg|_{\mathbf{b}=\mathbf{0}}. \qquad (7.9)
\end{aligned}
$$

We define $\partial_i := \partial/\partial b_i$, and compute

$$
\begin{aligned}
\partial_\mu\partial_\nu\exp\left[\frac{1}{2}(j_\alpha+b_\alpha)A^{-1}_{\alpha\beta}(j_\beta+b_\beta)\right]\Bigg|_{\mathbf{b}=\mathbf{0}} =&\frac{1}{2}\left(A^{-1}_{\mu\nu}+A^{-1}_{\nu\mu}\right)\exp\left(\frac{1}{2}j_\rho A^{-1}_{\rho\sigma}j_\sigma\right)\\
&+\frac{1}{4}\left(A^{-1}_{\mu\alpha}+A^{-1}_{\alpha\mu}\right)\left(A^{-1}_{\nu\beta}+A^{-1}_{\beta\nu}\right)j_\alpha j_\beta\\
&\times\exp\left(\frac{1}{2}j_\rho A^{-1}_{\rho\sigma}j_\sigma\right), \qquad (7.10)
\end{aligned}
$$

where implicit summations over repeated Greek indices are taken. Hence,

$$
\begin{aligned}
\langle\varphi_\mu\varphi_\nu\rangle =&\frac{1}{Z}\sum_{\{s(\mathbf{x},\mathbf{x}')\in\mathbb{Z}\}}\left[\frac{1}{2}\left(A^{-1}_{\mu\nu}+A^{-1}_{\nu\mu}\right)+\frac{1}{4}\left(A^{-1}_{\mu\alpha}+A^{-1}_{\alpha\mu}\right)\left(A^{-1}_{\nu\beta}+A^{-1}_{\beta\nu}\right)j_\alpha j_\beta\right]\\
&\times\int\bar{\mathcal{D}}\varphi\exp\left(-\beta H\right), \qquad (7.11)
\end{aligned}
$$

which simplifies to

$$
\langle\varphi_\mu\varphi_\nu\rangle =\frac{1}{2}\left(A^{-1}_{\mu\nu}+A^{-1}_{\nu\mu}\right)+\frac{1}{4}\langle\left(A^{-1}_{\mu\alpha}+A^{-1}_{\alpha\mu}\right)\left(A^{-1}_{\nu\beta}+A^{-1}_{\beta\nu}\right)j_\alpha j_\beta\rangle_s, \qquad (7.12)
$$

where $\langle\dots\rangle_s$ denotes a quasi-thermal average over the modular s variables.

To connect with the magnetization of the system, the object

$$
\langle\varphi_0^2\rangle = A^{-1}_{00}+\frac{1}{4}\langle\left(A^{-1}_{0\alpha}+A^{-1}_{\alpha 0}\right)\left(A^{-1}_{0\beta}+A^{-1}_{\beta 0}\right)j_\alpha j_\beta\rangle_s, \qquad (7.13)
$$

is computed. In Section 2.3.5, it was shown that

$$
A^{-1}_{ij}=\frac{1}{K}G(\mathbf{x}_i,\mathbf{x}_j). \qquad (7.14)
$$

Combining the above two equations with Eq. (2.73), the magnetization of the system is then given by

$$
\langle m\rangle = \left(\frac{1}{cN}\right)^{1/8\pi K}\exp\left[-\frac{\pi^2}{2}\langle\left[\sum_{\mathbf{x}\in D'}\left(G(\mathbf{x})+G(-\mathbf{x})\right)\Delta s(\mathbf{x})\right]^2\rangle_s\right] \qquad (7.15)
$$

(using $\langle \varphi_0^2 \rangle = \langle \psi_0^2 \rangle$, as shown in Appendix B), which, when combined with Eq. (7.1), generates

$$\tilde{K}_{\text{eff.}}^{-1}(L,T) = K^{-1} + \frac{4\pi^3}{\ln(cN)} \langle \left[\sum_{\mathbf{x}\in D'} \left(G(\mathbf{x}) + G(-\mathbf{x}) \right) \Delta s(\mathbf{x}) \right]^2 \rangle_s . \tag{7.16}$$

This equation describes the deviation of the finite-size effective spin stiffness $\tilde{K}_{\text{eff.}}$ of the Villain model from its spin-wave behaviour. As in Section 2.3.5, the Abel-Plana formula was used.

Eq. (7.11) relates the the spin-spin correlation with a quasi-thermal average: this is not a true thermal average. However, for weak coupling between the spin φ and modular s variables, which corresponds to low topological-defect density, the total Boltzmann weighting for the coupling between spin and modular variables is small. In this weak-coupling regime, we can therefore approximate Eq. (7.11) by moving the expression in the square parentheses back inside the functional integral over spin variables $\int \mathcal{D}\varphi$:

$$\langle \varphi_\mu \varphi_\nu \rangle \simeq \frac{1}{Z} \sum_{\{s(\mathbf{x},\mathbf{x}')\in\mathbb{Z}\}} \int \bar{\mathcal{D}}\varphi \left[\frac{1}{2} \left(A^{-1}_{\mu\nu} + A^{-1}_{\nu\mu} \right) + \frac{1}{4} \left(A^{-1}_{\mu\alpha} + A^{-1}_{\alpha\mu} \right) \left(A^{-1}_{\nu\beta} + A^{-1}_{\beta\nu} \right) j_\alpha j_\beta \right] e^{-\beta H} . \tag{7.17}$$

We therefore approximate

$$\langle \varphi_0^2 \rangle \simeq A^{-1}_{00} + \frac{1}{4} \langle \left(A^{-1}_{0\alpha} + A^{-1}_{\alpha 0} \right) \left(A^{-1}_{0\beta} + A^{-1}_{\beta 0} \right) j_\alpha j_\beta \rangle \tag{7.18}$$

for low topological-defect density. Defining

$$\bar{G}_{x/y}(\mathbf{x} + a\mathbf{e}_{x/y}/2) := G(\mathbf{x}) + G(-\mathbf{x}) - G(\mathbf{x} + a\mathbf{e}_{x/y}) - G(-\mathbf{x} - a\mathbf{e}_{x/y}), \tag{7.19}$$

this approximation is written in the more compact form:

$$\langle \varphi_0^2 \rangle \simeq \frac{1}{K} G(\mathbf{0}) + \pi^2 \langle \left[\sum_{\mathbf{x}\in D'} \bar{\mathbf{G}}(\mathbf{x}) \cdot \mathbf{s}(\mathbf{x}) \right]^2 \rangle . \tag{7.20}$$

The magnetization is then approximated by

$$\langle m \rangle \simeq \left(\frac{1}{cN} \right)^{1/8\pi K} \exp \left(-\frac{\pi^2}{2} \langle \left[\sum_{\mathbf{x}\in D'} \bar{\mathbf{G}}(\mathbf{x}) \cdot \mathbf{s}(\mathbf{x}) \right]^2 \rangle \right) , \tag{7.21}$$

for low topological-defect density. This is an approximate correction to the spin-wave expression of the magnetization of the Villain model for low topological-defect density, but in terms of true thermal averages.

We are able to simplify the thermal average in the exponent of the above equation by employing the weak-coupling argument: $\langle s_x(\mathbf{x}+a\mathbf{e}_x/2)s_y(\mathbf{x}'+a\mathbf{e}_y/2)\rangle$, $\langle s_x(\mathbf{x}+a\mathbf{e}_x/2)s_x(\mathbf{x}'+a\mathbf{e}_x/2)\rangle$, and $\langle s_y(\mathbf{x}+a\mathbf{e}_y/2)s_y(\mathbf{x}'+a\mathbf{e}_y/2)\rangle$ are all small compared with $\langle s_x^2(\mathbf{x}+a\mathbf{e}_x/2)\rangle$ and $\langle s_y^2(\mathbf{x}+a\mathbf{e}_y/2)\rangle$ in the weak-coupling regime, where the second and third expressions are for $\mathbf{x}\neq\mathbf{x}'$. It follows that

$$\begin{aligned}\langle\left[\sum_{\mathbf{x}\in D'}\bar{\mathbf{G}}(\mathbf{x})\cdot\mathbf{s}(\mathbf{x})\right]^2\rangle \simeq &\sum_{\mathbf{x}\in D'}\bar{G}_x^2(\mathbf{x}+a\mathbf{e}_x/2)\langle s_x^2(\mathbf{x}+a\mathbf{e}_x/2)\rangle\\ &+\sum_{\mathbf{x}\in D'}\bar{G}_y^2(\mathbf{x}+a\mathbf{e}_y/2)\langle s_y^2(\mathbf{x}+a\mathbf{e}_y/2)\rangle \qquad (7.22)\\ =&\langle s_x^2\rangle\sum_{\mathbf{x}\in D'}\bar{G}_x^2(\mathbf{x}+a\mathbf{e}_x/2)+\langle s_y^2\rangle\sum_{\mathbf{x}\in D'}\bar{G}_y^2(\mathbf{x}+a\mathbf{e}_y/2) \qquad (7.23)\end{aligned}$$

for low topological-defect density. This can be further simplified:

$$\begin{aligned}\sum_{\mathbf{x}\in D'}\bar{G}_x^2(\mathbf{x}+a\mathbf{e}_x/2)=&\sum_{\mathbf{x}\in D'}\sum_{\mathbf{k},\mathbf{k}'\neq\mathbf{0}}\gamma_{\mathbf{k}}\gamma_{\mathbf{k}'}e^{i\mathbf{x}\cdot(\mathbf{k}+\mathbf{k}')}(1-e^{iak_x})(1-e^{iak'_x})\\ &+\sum_{\mathbf{x}\in D'}\sum_{\mathbf{k},\mathbf{k}'\neq\mathbf{0}}\gamma_{\mathbf{k}}\gamma_{\mathbf{k}'}e^{i\mathbf{x}\cdot(\mathbf{k}-\mathbf{k}')}(1-e^{iak_x})(1-e^{-iak'_x})\\ &+\sum_{\mathbf{x}\in D'}\sum_{\mathbf{k},\mathbf{k}'\neq\mathbf{0}}\gamma_{\mathbf{k}}\gamma_{\mathbf{k}'}e^{-i\mathbf{x}\cdot(\mathbf{k}-\mathbf{k}')}(1-e^{-iak_x})(1-e^{iak'_x})\\ &+\sum_{\mathbf{x}\in D'}\sum_{\mathbf{k},\mathbf{k}'\neq\mathbf{0}}\gamma_{\mathbf{k}}\gamma_{\mathbf{k}'}e^{-i\mathbf{x}\cdot(\mathbf{k}+\mathbf{k}')}(1-e^{-iak_x})(1-e^{-iak'_x})\\ =&2G(\mathbf{0}), \qquad (7.24)\end{aligned}$$

and similarly in the y-component. Hence,

$$\langle\left[\sum_{\mathbf{x}\in D'}\bar{\mathbf{G}}(\mathbf{x})\cdot\mathbf{s}(\mathbf{x})\right]^2\rangle \simeq\frac{1}{2\pi}\ln(cN)\left(\langle s_x^2\rangle+\langle s_y^2\rangle\right) \qquad (7.25)$$

for low topological-defect density, where we have again used the Abel-Plana formula. The inverse finite-size effective spin stiffness $\tilde{K}_{\text{eff.}}^{-1}$ is then approximated by

$$\tilde{K}_{\text{eff.}}^{-1}(L,T)\simeq K^{-1}+2\pi^2\left(\langle s_x^2\rangle+\langle s_y^2\rangle\right) \qquad (7.26)$$

for low topological-defect density.

7.2 Connection with José *et al.*

It is worth pausing here to check the relationship between this result and the RG equations of José *et al.* [4]. The factor

$$\sum_{\mathbf{x}\in D'} \mathbf{x}^2 \langle m(\mathbf{0}) m(\mathbf{x})\rangle \tag{7.27}$$

in Eq. (4.34) of José *et al.* [4] can be related to our expression by considering the definition of the m values in José *et al.* [4]. They are given by $m(\mathbf{x}) = \Delta s(\mathbf{x})$ in our notation. Using the same weak-coupling arguments for the non-$\langle s_x^2\rangle$-like terms, we approximate

$$\sum_{\mathbf{x}\in D'} \mathbf{x}^2 \langle m(\mathbf{0}) m(\mathbf{x})\rangle \simeq -a^2 \left(\langle s_x^2(a\mathbf{e}_x/2)\rangle + \langle s_y^2(a\mathbf{e}_y/2)\rangle + \langle s_x^2(3a\mathbf{e}_x/2)\rangle + \langle s_y^2(3a\mathbf{e}_y/2)\rangle\right). \tag{7.28}$$

Eq. (4.34) of José *et al.* [4] then becomes

$$K_{\text{eff.}}^{-1} \simeq K^{-1} + 2\pi^2 \left(\langle s_x^2\rangle + \langle s_y^2\rangle\right) \tag{7.29}$$

in the weak-coupling regime (a factor of 2 comes from the erratum of José *et al.* [40]), which is the same as our expression for $\tilde{K}_{\text{eff.}}^{-1}$. Note that our connection with the finite-size effective spin stiffness allows for a connection to be made with the finite-size magnetization before the thermodynamic limit is taken.

7.3 Harmonic-mode Susceptibility

To relate our quantity to the harmonic-mode susceptibility, we switch to the emergent-field representation. In Chapter 6, we showed that the Villain model admits an emergent electric field $\mathbf{E}$: the effective spin stiffness can be expressed in terms of the harmonic-mode susceptibility of the emergent field $\chi_{\bar{\mathbf{E}}}$. The definition of $\bar{\mathbf{E}}$ results in

$$\bar{E}_x = \frac{2\pi J}{Na} \sum_{\mathbf{x}\in D'} s_x(\mathbf{x} + a\mathbf{e}_x/2), \tag{7.30}$$

and similarly in y. Hence,

$$\langle \bar{E}_x^2\rangle = \frac{4\pi^2 J^2}{N^2 a^2} \langle \left[\sum_{\mathbf{x}\in D'} s_x(\mathbf{x} + a\mathbf{e}_x/2)\right]^2 \rangle \tag{7.31}$$

$$= \frac{4\pi^2 J^2}{N^2 a^2} \langle \sum_{\mathbf{x}\in D'} s_x^2(\mathbf{x} + a\mathbf{e}_x/2) + \sum_{\mathbf{x}\neq\mathbf{x}'} s_x(\mathbf{x} + a\mathbf{e}_x/2) s_x(\mathbf{x}' + a\mathbf{e}_x/2)\rangle \tag{7.32}$$

$$\simeq \frac{4\pi^2 J^2}{N^2 a^2} N \langle s_x^2 \rangle \tag{7.33}$$

for low topological-defect density, and similarly in the y-component. It then follows that

$$\langle \bar{\mathbf{E}}^2 \rangle = \langle \bar{E}_x^2 + \bar{E}_y^2 \rangle \simeq \frac{4\pi^2 J^2}{N^2 a^2} N \langle s_x^2 + s_y^2 \rangle, \tag{7.34}$$

and hence that

$$\begin{aligned}
\tilde{K}_{\text{eff.}}^{-1}(L,T) \simeq & K^{-1}(T) + 2\pi^2 \frac{N a^2}{4\pi^2 J^2} \langle \bar{\mathbf{E}}^2 \rangle & (7.35)\\
= & K^{-1}(T) + \frac{L^2}{2J^2} \langle \bar{\mathbf{E}}^2 \rangle & (7.36)\\
= & K^{-1}(T) + \frac{1}{2} K^{-1}(T) \frac{\beta L^2}{J} \langle \bar{\mathbf{E}}^2 \rangle & (7.37)\\
= & K^{-1}(T) + \frac{1}{2} K^{-1}(T) \chi_{\bar{\mathbf{E}}}(L,T) & (7.38)\\
= & K^{-1}(T) \left(1 + \frac{1}{2} \chi_{\bar{\mathbf{E}}}(L,T)\right) & (7.39)
\end{aligned}$$

for low topological-defect density. Combining this with Eq. (7.1), we have that

$$\langle m \rangle \simeq \left(\frac{1}{cN}\right)^{(1+\chi_{\bar{\mathbf{E}}}(L,T)/2)/8\pi K(T)} \tag{7.40}$$

for low topological-defect density.

7.4 The Helicity Modulus

The connection with the finite-size helicity modulus $\tilde{\Upsilon}$ is made in this section. Eq. (7.39) becomes an equality in the limit of vanishing $\chi_{\bar{\mathbf{E}}}$, since all approximations used in this chapter become equalities in this limit. It follows that the perturbation $K^{-1}(T) \mapsto K^{-1}(T)\left(1 + \chi_{\bar{\mathbf{E}}}(L,T)/2\right)$ describes the change in the inverse effective spin stiffness due to an infinitesimally small increase in the value of $\chi_{\bar{\mathbf{E}}}$ from zero. In the following, we apply a Dyson-like self-consistent approach to applying this perturbation an infinite number of times. It follows that

$$\left(K^{-1}\right)'(L,T) = K^{-1}(T) + K^{-1}(T) \frac{1}{2} \chi_{\bar{\mathbf{E}}}(L,T) \tag{7.41}$$

is the first perturbation of the inverse spin stiffness. On the right-hand side of the above equation, repeating this perturbation to the inverse spin stiffness that has not already been perturbed (i.e., the right-hand inverse spin stiffness), it follows that

$$\left(K^{-1}\right)''(L,T) = K^{-1}(T) + \left(K^{-1}\right)'(L,T)\frac{1}{2}\chi_{\bar{\mathbf{E}}}(L,T) \tag{7.42}$$

$$= K^{-1}(T)\left(1 + \frac{1}{2}\chi_{\bar{\mathbf{E}}}(L,T) + \frac{1}{4}\chi_{\bar{\mathbf{E}}}^{2}(L,T)\right) \tag{7.43}$$

is the second perturbation of the inverse spin stiffness. Repeating this perturbation an infinite number of times, we find the inverse finite-size effective spin stiffness:

$$\tilde{K}_{\text{eff.}}^{-1}(L,T) \equiv \left(K^{-1}\right)^{\infty}(L,T) \tag{7.44}$$

$$= K^{-1}(T)\left(1 + \frac{1}{2}\chi_{\bar{\mathbf{E}}}(L,T) + \frac{1}{4}\chi_{\bar{\mathbf{E}}}^{2}(L,T) + \frac{1}{8}\chi_{\bar{\mathbf{E}}}^{3}(L,T) + \dots\right) \tag{7.45}$$

$$= K^{-1}(T)\left(1 - \frac{1}{2}\chi_{\bar{\mathbf{E}}}(L,T)\right)^{-1}, \tag{7.46}$$

where the symbol ∞ denotes an infinite number of perturbations. Taking the reciprocal of the above equation, it follows that

$$\tilde{K}_{\text{eff.}}(L,T) = K(T)\left(1 - \frac{1}{2}\chi_{\bar{\mathbf{E}}}(L,T)\right) = \beta\tilde{\Upsilon}(L,T), \tag{7.47}$$

which relates the finite-size effective spin stiffness to the finite-size helicity modulus in the limit of small $\chi_{\bar{\mathbf{E}}}$. We expect this expression to be a good approximation at any temperature at which topological defects are bound, and to therefore remain a good approximation up to the finite-size transition temperature $T^{*}(L)$, where topological defects begin to unbind.

Combining Eqs. (7.1) and (7.47), it follows that

$$\langle m \rangle = \left(\frac{1}{cN}\right)^{1/8\pi\beta\tilde{\Upsilon}(L,T)} \tag{7.48}$$

in the limit of small $\chi_{\bar{\mathbf{E}}}$. Again, we expect this expression to remain a good approximation up to the temperature $T = T^{*}(L)$. As the behaviour of the helicity modulus at the BKT transition is universal in XY-type spin models, it follows that Eqs. (7.47) and (7.48) should apply to all XY-type spin models. Fig. 7.1 shows Eq. (7.48) analytically continued into the high-temperature regime in which it breaks down. The data sets are for elementary-charge Coulomb gases of linear sizes $L = 32$, 64 and 128, where we have recalled Eq. (6.36):

$$\epsilon_{\text{eff.}}^{-1}(L,T) \equiv \tilde{\Upsilon}(L,T), \tag{7.49}$$

which is a result of the equivalence between the MR electrostatic and Villain models.

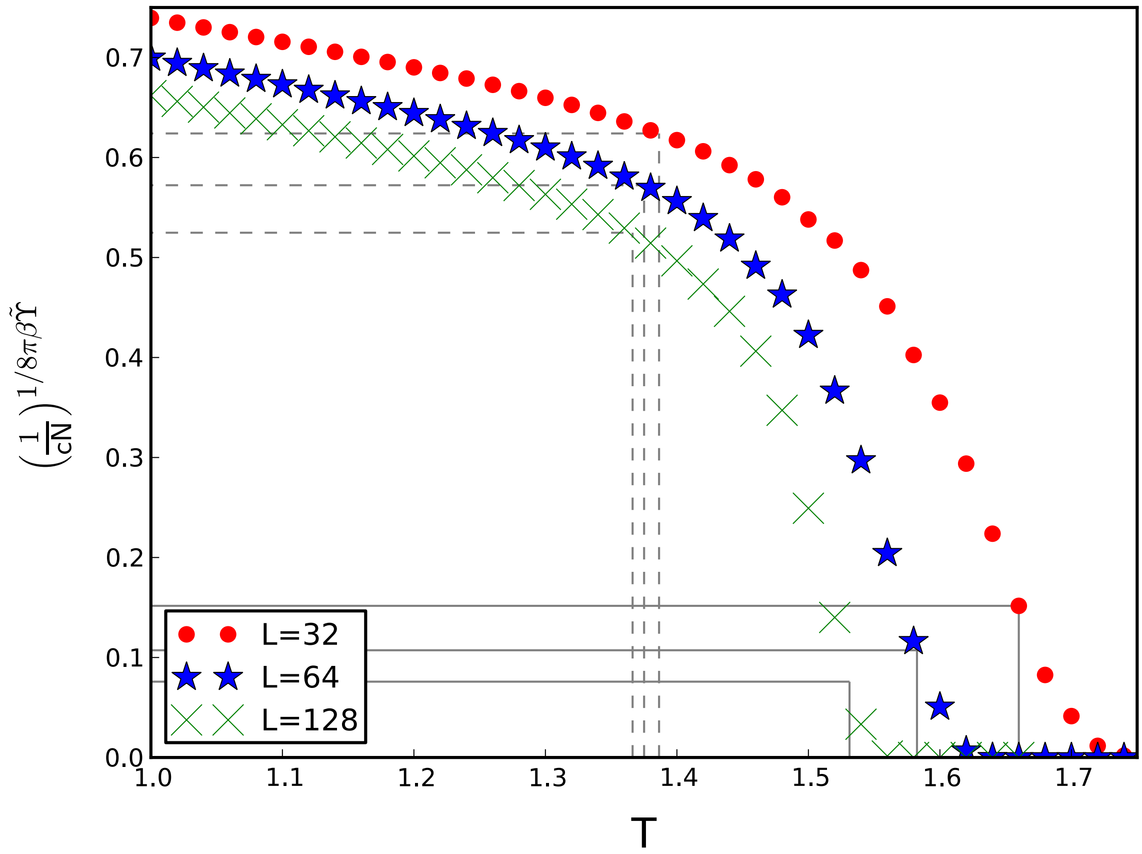

Figure 7.1: Eq. (7.48) (analytically continued into the high-temperature regime in which it breaks down for the modest system sizes shown) as a function of T for two-dimensional Coulomb gases of elementary charges (with the core-energy constant set to zero). The data sets are for systems of linear system size $L = 32$ (red dots), 64 (blue stars), and 128 (green crosses). Dashed / solid vertical grey lines meet each curve at $T = \tilde{T}^*(L)$ / $T = \tilde{T}_C(L)$.

This analysis is seen to be consistent with Eq. (2.117) of BKT theory when the thermodynamic limit of Eq. (7.47) is taken for $T \leq T_{\mathrm{BKT}}$:

$$K_{\mathrm{eff.}}(T) = \lim_{L\to\infty}\left[\tilde{K}_{\mathrm{eff.}}(L,T)\right] = \beta \lim_{L\to\infty}\left[\tilde{\Upsilon}(L,T)\right] = \beta\Upsilon(T). \tag{7.50}$$

7.5 Preliminary Applications

The relationship between the magnetization and the finite-size helicity modulus seen in Eq. (7.48) suggests that the signature of BH theory - the unique value of the effective critical exponent - outlined in Section 2.5 should be measurable through the helicity modulus of the XY-type spin model in question. This section comprises of a preliminary study of the relationship between the helicity modulus and BH theory.

7.5.1 Finite-size Transition Temperatures: Revision

In finite-size BKT systems, the two transition temperatures are the upper ($T_{\mathrm{C}}(L)$) and lower ($T^*(L)$) bounds of the temperature range over which the transition occurs. In BH theory, the effective critical exponent is measured with respect to the reduced temperature $t(L) := T_{\mathrm{C}}(L) - T$ at the lower bound of the transition. This lower bound is the temperature at which

$$\tilde{K}_{\mathrm{eff.}}(L, T) = 2/\pi. \tag{7.51}$$

In the vicinity of this temperature, few topological defects are unbound, hence Eq. (7.48) is a good approximation. For a measurement of the signature of BH theory via the helicity modulus to be considered rigorous, the finite-size transition temperatures must be measured through the finite-size helicity modulus. We define $\tilde{T}^*(L)$ to be the lower bound of the transition as measured via the finite-size helicity modulus:

$$\beta\tilde{\Upsilon}(L, T) = 2/\pi \tag{7.52}$$

at $T = \tilde{T}^*(L)$. Since Eq. (7.48) is a good approximation in the vicinity of the lower bound of the transition, it follows that $\tilde{T}^*(L) \simeq T^*(L)$. The vertical dashed grey lines in Fig. 7.1 meet each curve at the $\tilde{T}^*(L)$ of the corresponding system size.

Topological defects deconfine at temperatures above the lower bound so that, for modest system sizes, Eq. (7.48) completely breaks down: defining an upper bound of the transition with respect to the finite-size helicity modulus will give a markedly different value to the true $T_{\mathrm{C}}(L)$ of BH theory. For very large systems, however, the $\beta\tilde{\Upsilon}$ and effective spin-stiffness curves converge, as seen in Eq. (2.117). The upper bound of the transition as measured through the finite-size helicity modulus will therefore converge on the true $T_{\mathrm{C}}(L)$ in the asymptotic regime of very large system size (as will $\tilde{T}^*(L)$ on $T^*(L)$): the signature of BH theory is expected to measurable through the helicity modulus in the limit of very large system size. We test the appearance of this signature on modestly sized Coulombic systems, before extending into the asymptotic regime in the final subsection, where we apply BH theory to superfluid ^{4}He data, which corresponds to an extremely large Coulombic system. It must be kept in mind that any signature measured through the finite-size helicity modulus at modest system size is only to be taken as an indicator of this signature being truly measurable in the asymptotic regime.

To proceed, a pragmatic revision of the upper bound (with respect to the finite-size helicity modulus) is the temperature at which the analytically continued curve of Eq. (7.48) has decreased to the fourth power of its value at $T = \tilde{T}^*(L)$: the upper bound $\tilde{T}_{\mathrm{C}}(L)$ is therefore defined to be the point at which

$$\beta\tilde{\Upsilon}(L,T) = 1/2\pi. \tag{7.53}$$

The vertical solid grey lines in Fig. 7.1 meet each curve at the $\tilde{T}_{\mathrm{C}}(L)$ of the corresponding system size, which is seen to be a good, pragmatic estimate of the upper bound of the transition. The reduced temperature with respect to the finite-size helicity modulus $\tilde{t}(L)$ is now defined via

$$\tilde{t}(L) := \tilde{T}_C(L) - T. \tag{7.54}$$

Considering Eqs. (2.128) and (2.131), these new definitions of the bounds of the finite-size transition range necessarily result in a floating, system-size dependent $\tilde{T}_{\mathrm{BKT}}(L)$: this object has no physical significance at modest system sizes. It does, however, scale like $1/\ln(L)$ to $T_{\mathrm{BKT}} = 1.35$ (to three significant figures) in the thermodynamic limit, recovering consistency with the asymptotic regime.

7.5.2 The Critical Exponent

The connection with BH theory now follows. Combining the approximation of Eq. (7.48) at $T = \tilde{T}^*(L)$ with standard BH theory, we predict that

$$\frac{3\pi^2}{128} \simeq \frac{\ln(1/cN)}{8\pi} \frac{\partial\left(k_{\mathrm{B}}T/\tilde{\Upsilon}(L,T)\right)}{\partial\ln(\tilde{t}(L))}\Bigg|_{T=\tilde{T}^*(L)} . \tag{7.55}$$

for large but modestly sized Coulomb / Villain systems. We stress again that any agreement with this prediction should only be taken as an indication of the signature of BH theory being measurable through the finite-size helicity modulus in the asymptotic regime, where $\tilde{T}_{\mathrm{C}}(L)$ converges on $T_{\mathrm{C}}(L)$ so that the temperatures of the above equation can be replaced by their non-tilde counterparts.

Fig. 7.2 shows $\ln(1/cN)/8\pi\beta\tilde{\Upsilon}(L,T)$ versus $\ln(\tilde{t}(L))$ for two-dimensional Coulomb gases of elementary charges (with the core-energy constant set to zero). The data sets are for systems of linear size $L = 32$, 64 and 128. Tangents with gradients of $3\pi^2/128$ are compared with each data set, and vertical lines show each $\tilde{T}^*(L)$. We observe excellent comparisons between the data and the tangents at $T = \tilde{T}^*(L)$ for all system sizes, as predicted by Eq. (7.55). This result, combined with the scaling of the floating $\tilde{T}_{\mathrm{BKT}}(L)$ to T_{BKT} (as $1/\ln(L)$) into the asymptotic regime, indicates that the effective critical exponent of BH theory should be measurable through the finite-size helicity modulus in the limit of very large but finite

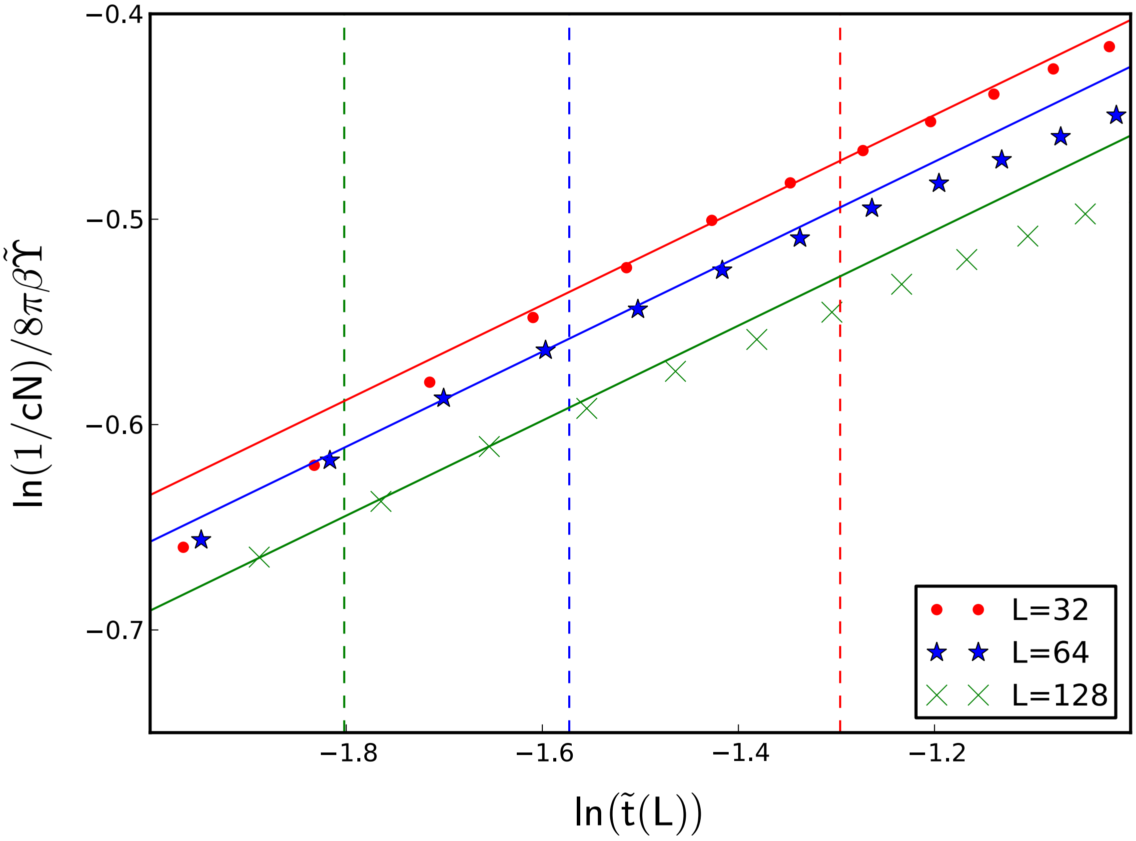

FIGURE 7.2: $\ln(1/cN)/8\pi\beta\tilde{\Upsilon}(L,T)$ versus $\ln(\tilde{t}(L))$ for two-dimensional Coulomb gases of elementary charges (with the core-energy constant set to zero). The data sets are for systems of linear system sizes $L = 32$ (red dots), 64 (blue stars), and 128 (green crosses). Straight lines with gradients of $3\pi^2/128$ are superimposed on each data set at $\tilde{t}(L) = \tilde{T}_C(L) - \tilde{T}^*(L)$, which is represented by the red ($L = 32$), blue ($L = 64$), and green ($L = 128$) vertical dashed lines.

system size. The requirement of an asymptotically large system is not a drawback of the theory, as the thermodynamic limit of Eq. (2.108) is approached so slowly that any real BKT system would be asymptotically large but finite [19].

7.5.3 Superfluid Films

Superfluid ^{4}He films are described by the two-dimensional Coulomb gas [9–12] with

$$\tilde{\Upsilon}(L,T) = \frac{m^2}{\hbar^2}\rho_{\rm s}(L,T), \tag{7.56}$$

where m is the mass of ^{4}He, $\hbar$ is the reduced Planck's constant, and $\rho_{\rm s}$ is the superfluid density. The data presented in the work of Bishop and Reppy [11, 12] corresponds to a superfluid film of linear size $L = e^{12}$, an extremely large but finite effective Coulomb gas for which

$$\tilde{K}_{\text{eff.}}(L,T) \simeq \beta\tilde{\Upsilon}(L,T) \tag{7.57}$$

at $T = \tilde{T}_{\text{C}}(L) \simeq T_{\text{C}}(L)$. We therefore combine Eqs. (7.48) and (7.56) to transform data digitized from Bishop and Reppy [11, 12] into an effective magnetization given by

$$\langle m \rangle = \left(\frac{1}{cN}\right)^{\hbar^2/8\pi\beta m^2 \rho_{\text{s}}(L,T)} \tag{7.58}$$

in the asymptotic regime corresponding to the Bishop-Reppy experiment [11, 12], which has been set as an equality since $\tilde{K}_{\text{eff.}}(L,T)$ has effectively converged on $\beta\tilde{\Upsilon}(L,T)$ at $T = \tilde{T}_{\text{C}}(L) \simeq T_{\text{C}}(L)$. From this, we expect to measure an effective critical exponent of $\tilde{\beta} = 3\pi^2/128$ at $T = T^*(L)$, which corresponds to measuring the signature of BH theory through the finite-size helicity modulus of an asymptotically large Coulomb gas. Since the system is in the asymptotic regime, we drop the tilde from $\tilde{T}^*(L)$ and $\tilde{T}_{\text{C}}(L)$, as these temperatures have effectively converged on their true counterparts of Section 2.5.

The Bishop-Reppy experiment [11, 12] consists of a ^{4}He film adsorbed on a sheet of Mylar that has been wrapped into a coil. A sinusoidal driving frequency ω is applied to the Mylar coil in the direction of its long axis. This generates a frequency-dependent analogue of the electric permittivity of the Coulomb gas $\epsilon(\omega, T)$ [10]. Bishop and Reppy then measured the reduced shift in the period of oscillation of the Mylar coil $\Delta P/P$, as well as the superfluid dissipation Q^{-1} of the ^{4}He film. This reduced shift in the period of oscillation is due to the ^{4}He film decoupling from the Mylar coil as its superfluid density increases at low temperature. By defining

$$p(\omega,T) := \frac{2\Delta P(\omega,T)}{P(T)} \tag{7.59}$$

and

$$q(\omega,T) := Q^{-1}(\omega,T), \tag{7.60}$$

it follows from Eqs. (A4) and (A5) of Bishop and Reppy [12] that

$$p(\omega,T) = C\text{Re}\left[\epsilon^{-1}(\omega,T)\right] \tag{7.61}$$

and

$$q(\omega,T) = C\text{Im}\left[-\epsilon^{-1}(\omega,T)\right], \tag{7.62}$$

where C is a constant given in the paper.

Upon setting $\epsilon'(\omega, T)$ and $\epsilon''(\omega, T)$ to be the real and imaginary parts of $\epsilon(\omega, T)$, respectively, it follows from Eq. (9) of Ambegaokar *et al.* (AHNS) [10] that

$$\epsilon'(\omega, T) = \epsilon(r = L(\omega), T) \tag{7.63}$$

and

$$\epsilon''(\omega, T) = \frac{\pi}{4} \left. \frac{\partial \epsilon(r, T)}{\partial \ln r} \right|_{r=L(\omega)}, \tag{7.64}$$

where the dynamic length scale $L(\omega) := \sqrt{14D/a^2\omega}$ (defined in anticipation that it will correspond to an effective linear system size of the Coulomb gas) is taken from Bishop and Reppy [12], and, from José *et al.* [4], $\epsilon(r, T)$ is the static, distant-dependent analogue of the permittivity that includes the effect of screening only from topological-defect pairs whose separation distance $d \leq r$ (it is standard to use the same notation for the static and dynamic permittivities). Combining Eqs. (7.61) to (7.64), it then follows that

$$\epsilon^{-1}(L(\omega), T) = \frac{p(\omega, T)}{C} \left(1 + \left(\frac{q(\omega, T)}{p(\omega, T)} \right)^2 \right), \tag{7.65}$$

which, when combined with Eqs. (6.36) and (7.56), can be rewritten as

$$\rho_s(L(\omega), T) = \frac{\hbar^2 J}{Cm^2} p(\omega, T) \left(1 + \left(\frac{q(\omega, T)}{p(\omega, T)} \right)^2 \right). \tag{7.66}$$

This is set as an equality since Eq. (7.57) converges on an equality at $T = T_{\mathrm{C}}(L)$ in the asymptotic regime of the Bishop-Reppy experiment. Substituting the above expression into Eq. (7.58) provides a route to testing the applicability of BH theory to the superfluid film. Although not stated explicitly, it appears that Bishop and Reppy set $J = 2T^*(L)/\pi$ in our notation.

Fig. 7.3 shows the signature of BH theory to be hidden in the experimental data of Bishop and Reppy [11, 12]. We extract the superfluid density from the digitized data using Eq. (7.66) and transform this into the effective magnetization given by Eq. (7.58). We plot this quantity as a function of T (left) and reduced temperature $t(L) := T_{\mathrm{C}}(L) - T$ (right), where the right-hand plot is on a log-log scale, and T in units of K. The data presented has no fitted parameters: $T^*(L) = 1.2043\,K$, $T_{\mathrm{C}}(L) = 1.215\,K$, and $L = e^{12}$ are all taken as quoted in Bishop and Reppy [11, 12]. Inserting $\tilde{\beta} = 3\pi^2/128$ at $T = T^*(L)$ into Eq. (2.133), it

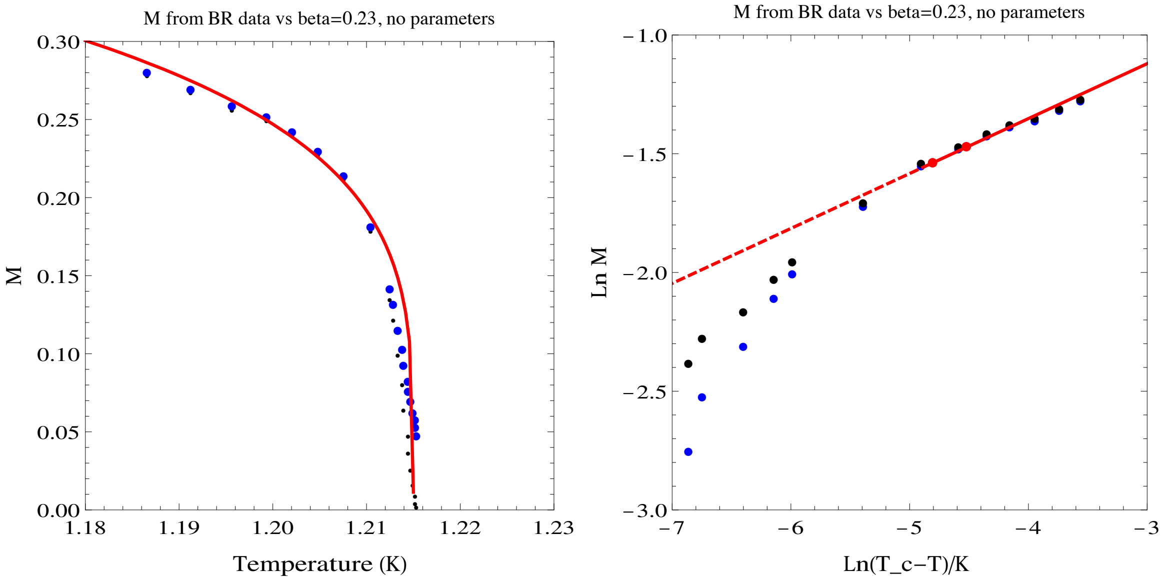

FIGURE 7.3: Digitized Bishop-Reppy superfluid data transformed into an effective finite-size magnetization (left) and on a log-log scale (right), with BH $\tilde{\beta} = 3\pi^2/128$ curves superimposed in red. $T^*(L)$ (left-hand red circle) and $T_{\rm BKT}$ (right-hand red circle) are marked on the right-hand plot. In the region of the dashed line, BH theory is not expected to describe the data. There are no fitted parameters: all parameters are taken from the work of Bishop and Reppy [11, 12]. The black data is the total superfluid density, as given by the full AHNS theory; the blue data corresponds to setting $q(\omega, T) = 0$, which is only permitted near $T = T^*(L)$ and below: this subtlety is outlined in Appendix D.

follows that

$$\left(\frac{1}{cN}\right)^{1/16} = \text{const.}\,(T_{\rm C}(L) - T^*(L))^{3\pi^2/128}\,. \tag{7.67}$$

From this, BH theory then predicts that

$$\langle m \rangle = \left(\frac{1}{cN}\right)^{1/16} (T_{\rm C}(L) - T^*(L))^{-3\pi^2/128}\,(T_{\rm C}(L) - T)^{3\pi^2/128} \tag{7.68}$$

at $T = T^*(L)$. We superimpose this curve in red on both plots in Fig. 7.3, again, with no fitted parameters, showing agreement between the curves and the data at $T = T^*(L)$: BH theory is shown to apply to real, thin-film superfluids, and its signature is in fact hidden in the data of the seminal work of Bishop and Reppy [11, 12].

Further to showing that BH theory applies to the superfluid film, the analysis presented in this subsection also offered an asymptotically large effective Coulomb gas on which to test the validity of measuring the signature of BH theory through the effective electric permittivity / helicity modulus of the Coulomb gas / Villain model. This final subsection has shown that, for sufficiently large systems, the analysis leading to Eq. (7.55) holds: it is inferred that BH theory applies to general BKT systems, and its signature can be measured through the finite-size helicity modulus of sufficiently large but finite-size systems.

Chapter 8

Conclusions

In conclusion, we have investigated two important properties of the BKT transition: the signalling of the high-temperature phase by topological-sector fluctuations and the applicability of BH theory to general BKT systems. This was performed in parallel with the helpful mapping between the MR electrostatic model applied to the two-dimensional Coulomb gas and Villain's approximation to the XY model of magnetism.

We simulated the two-dimensional lattice Coulomb gas on a torus using the MR algorithm with both local and global updates employed to relate topological-sector fluctuations in the electric field to the BKT phase transition. Topological-sector fluctuations in the electric field switch on precisely at the BKT transition temperature. Our analysis showed that, in the case of the BKT transition, the ordering of a conventional order parameter is replaced by topological ordering through an ergodicity breaking between the topological sectors. The topological order is directly related to the confinement-deconfinement transition of the charges, the local topological defects of the electric field. This type of ergodicity breaking is distinct from either the symmetry breaking that characterizes a standard phase transition, or that due to the rough free-energy landscape that develops at a spin-glass transition [27].

The topological-sector fluctuations are very clearly revealed in the lattice electric field description of the two-dimensional Coulomb gas, but we expect them to be equally relevant to any system that has a BKT transition. In suitable systems, the winding-field susceptibility that signals the onset of topological-sector fluctuations will contribute to experimentally measurable responses of the system. A promising system on which to measure these topological-sector fluctuations is the one-dimensional quantum lattice Bose gas. When the system is placed on a ring, its angular momentum is no longer a good quantum number. The angular momentum can therefore fluctuate quantum mechanically, and the system should undergo a dramatic increase in these fluctuations as it passes through the superfluid

– Mott insulator quantum phase transition [64, 65]. This dramatic increase in the fluctuations corresponds to finite-valued global topological defects in the quantum system, and therefore, via the Feynman path-integral mapping, to topological-sector fluctuations in the two-dimensional classical lattice Coulomb gas on a torus. Murray *et al.* measured the angular momentum of ring-shaped Bose-Einstein condensates via the vortex-density profile of the system [66]. Our measure of the BKT transition could therefore correspond to equivalent, experimentally measurable topological-sector fluctuations in the cold-atom system.

We performed a series of simulations of the two-dimensional XY and HXY models in order to confirm the emergent Coulomb lattice Green's function of the HXY model and to probe the effective Coulombic behaviour of the two models. This, combined with analytic work on the MR electrostatic and Villain models, allowed us to elucidate the emergent Coulombic physics of XY-type spin models and to show that topological-sector fluctuations in the emergent electric field of the XY models correspond to twist fluctuations in their spin fields. The signature of the topological-sector fluctuations of Chapter 5 could therefore be observable in ultrathin ferromagnetic metallic films [61], magnetic Langmuir-Blodgett films [62, 63], or ferromagnetic films with a 'washer' geometry (PBCs in one direction).

The emergent electrostatics shown by the mapping allowed us to use the Villain model to show that BH theory applies to the general BKT system: the unique value of the effective critical exponent of BH theory is hidden in the classic experimental data of the superfluid ^{4}He film [11]. This unification of identical, experimentally measurable signatures in the ferromagnetic and superfluid films is a triumph of both BH and BKT theory, and provides an incredible example of the power of statistical mechanics and the renormalization group.

Appendix A

Dimensional Analysis of the Two-dimensional Coulomb Gas

In the following, $[\dots]$ denotes the units of some quantity, L denotes the dimensions of length, d is the spatial dimensionality of the system, and ϵ_0 is the vacuum permittivity in d-dimensional space.

With Gauss' law on a lattice,

$$\hat{\boldsymbol{\nabla}} \cdot \mathbf{E}(\mathbf{x}) = \rho(\mathbf{x})/\epsilon_0, \tag{A.1}$$

and the dimensions of the electric-charge density in d dimensions,

$$[\rho(\mathbf{x})] = [q]\, L^{-d}, \tag{A.2}$$

it follows that

$$[\mathbf{E}(\mathbf{x})] = [q]\, L^{(1-d)}\, [\epsilon_0]^{-1}\, . \tag{A.3}$$

The exponent of the Boltzmann probability must be dimensionless, hence,

$$\begin{aligned}
1 =& \left[\frac{a^d \beta \epsilon_0}{2} \sum_{\mathbf{x}\in D} |\mathbf{E}(\mathbf{x})|^2 \right] && \text{(A.4)}\\
=& L^d\, [\beta]\, [\epsilon_0]\, [\mathbf{E}(\mathbf{x})]^2 && \text{(A.5)}\\
\Leftrightarrow [\epsilon_0]^{-1} =& L^d\, [\beta]\, [\mathbf{E}(\mathbf{x})]^2 && \text{(A.6)}\\
\Rightarrow [\mathbf{E}(\mathbf{x})] =& [q] L^{(1-d)} L^d\, [\beta]\, [\mathbf{E}(\mathbf{x})]^2 && \text{(A.7)}\\
\Leftrightarrow [\mathbf{E}(\mathbf{x})] =& [q]^{-1} L^{-1}\, [\beta]^{-1}\, . && \text{(A.8)}
\end{aligned}$$

In $d = 2$, we set the charge to be dimensionless, and it follows that

$$[\mathbf{E}(\mathbf{x})] = [\beta]^{-1} L^{-1}, \tag{A.9}$$

and hence that

$$[\epsilon_0] = [\beta]\,. \tag{A.10}$$

The same dimensions follow for the electric fields of the continuum system.

Appendix B

Spin-wave Analysis

B.1 Relationship between ψ and the Magnetization

The magnetization of the harmonic model is related to the quantity ψ by

$$
\begin{aligned}
\langle m\rangle =& \langle\frac{1}{N}\sum_{\mathbf{x}\in D}\cos(\psi(\mathbf{x}))\rangle && \text{(B.1)}\\
=& \frac{1}{N}\sum_{\mathbf{x}\in D}\langle\cos(\psi(\mathbf{x}))\rangle && \text{(B.2)}\\
=& \langle\cos(\psi(\mathbf{0}))\rangle && \text{(B.3)}\\
=& \sum_{p=0}^{\infty}\frac{(-1)^p}{p!}\langle\psi^{2p}(\mathbf{0})\rangle && \text{(B.4)}\\
=& \sum_{p=0}^{\infty}\frac{(-1)^p}{p!}(2p-1)!!\langle\psi^{2}(\mathbf{0})\rangle^p && \text{(B.5)}\\
=& \sum_{p=0}^{\infty}\frac{1}{2^p p!}\langle-\psi^{2}(\mathbf{0})\rangle^p && \text{(B.6)}\\
=& \sum_{p=0}^{\infty}\frac{1}{p!}\langle-\frac{1}{2}\psi^{2}(\mathbf{0})\rangle^p && \text{(B.7)}\\
=& \exp\left[\left(-\frac{1}{2}\langle\psi^{2}(\mathbf{0})\rangle\right)\right], && \text{(B.8)}
\end{aligned}
$$

where Wick's theorem is used in Eq.(B.5).

B.2 Relationship between ψ and φ

In all XY-type spin models, the quantity

$$\langle\psi(\mathbf{x})\psi(\mathbf{x}')\rangle = \langle\varphi(\mathbf{x})\varphi(\mathbf{x}')\rangle - \langle\varphi(\mathbf{x})\bar{\varphi}\rangle - \langle\varphi(\mathbf{x}')\bar{\varphi}\rangle + \langle\bar{\varphi}\bar{\varphi}\rangle. \tag{B.9}$$

becomes

$$\langle\psi(\mathbf{x})\psi(\mathbf{x}')\rangle = \langle\varphi(\mathbf{x})\varphi(\mathbf{x}')\rangle \tag{B.10}$$

because the final three terms of the above expression are zero:

$$\begin{aligned}
\langle\varphi(\mathbf{x})\bar{\varphi}\rangle =& \langle\varphi(\mathbf{x})\frac{1}{N}\sum_{\mathbf{x}''}\varphi(\mathbf{x}'')\rangle && \text{(B.11)}\\
=&\frac{1}{N}\sum_{\mathbf{x}''}\langle\varphi(\mathbf{x})\varphi(\mathbf{x}'')\rangle && \text{(B.12)}\\
=&\frac{1}{N}\sum_{\mathbf{x}''}\frac{1}{\beta J}\sum_{\mathbf{k}\neq\mathbf{0}}\frac{e^{i\mathbf{k}\cdot(\mathbf{x}-\mathbf{x}'')}}{2N(2-\cos(k_x a)-\cos(k_y a))} && \text{(B.13)}\\
=&\frac{1}{\beta J}\sum_{\mathbf{k}\neq\mathbf{0}}\frac{e^{i\mathbf{k}\cdot\mathbf{x}}}{2N(2-\cos(k_x a)-\cos(k_y a))}\frac{1}{N}\sum_{\mathbf{x}''}e^{-i\mathbf{k}\cdot\mathbf{x}''} && \text{(B.14)}\\
=&\frac{1}{\beta J}\sum_{\mathbf{k}\neq\mathbf{0}}\frac{e^{i\mathbf{k}\cdot\mathbf{x}}}{2N(2-\cos(k_x a)-\cos(k_y a))}\delta^{(2)}(\mathbf{k}) && \text{(B.15)}\\
=&0. && \text{(B.16)}
\end{aligned}$$

Appendix C

The Decoupling of the Internal Energy of the Lattice Electric Field

The internal energy of the general electric field of the two-dimensional lattice system is given by

$$U_0 = \frac{\epsilon_0 a^2}{2} \sum_{\mathbf{x} \in D} |\mathbf{E}(\mathbf{x})|^2 \,. \tag{C.1}$$

This expression generates terms which go like the sum of the squares of each contribution to the total field along with some cross terms which sum to zero:

$$\begin{aligned}
U_0 =& \frac{\epsilon_0 a^2}{2} \sum_{\mathbf{x} \in D} \left[| - \tilde{\boldsymbol{\nabla}} \phi(\mathbf{x}) + \tilde{\mathbf{E}}(\mathbf{x})|^2 \right] + \frac{\epsilon_0 a^2}{2} \sum_{\mathbf{x} \in D} \left\{ |\bar{\mathbf{E}}|^2 + 2\, \bar{\mathbf{E}} \cdot \left[-\tilde{\boldsymbol{\nabla}} \phi(\mathbf{x}) + \tilde{\mathbf{E}}(\mathbf{x}) \right] \right\} && \text{(C.2)} \\
=& \frac{\epsilon_0 a^2}{2} \sum_{\mathbf{x} \in D} \left[| - \tilde{\boldsymbol{\nabla}} \phi(\mathbf{x}) + \tilde{\mathbf{E}}(\mathbf{x})|^2 \right] + \frac{L^2 \epsilon_0}{2} |\bar{\mathbf{E}}|^2 + \epsilon_0 a^2\, \bar{\mathbf{E}} \cdot \sum_{\mathbf{x} \in D} \left[-\tilde{\boldsymbol{\nabla}} \phi(\mathbf{x}) + \tilde{\mathbf{E}}(\mathbf{x}) \right] && \text{(C.3)} \\
=& \frac{\epsilon_0 a^2}{2} \sum_{\mathbf{x} \in D} \left[|\tilde{\boldsymbol{\nabla}} \phi(\mathbf{x})|^2 + |\tilde{\mathbf{E}}(\mathbf{x})|^2 \right] - \epsilon_0 a^2 \sum_{\mathbf{x} \in D} \tilde{\boldsymbol{\nabla}} \phi(\mathbf{x}) \cdot \tilde{\mathbf{E}}(\mathbf{x}) + \frac{L^2 \epsilon_0}{2} |\bar{\mathbf{E}}|^2 && \text{(C.4)} \\
=& \frac{\epsilon_0 a^2}{2} \sum_{\mathbf{x} \in D} \left[|\tilde{\boldsymbol{\nabla}} \phi(\mathbf{x})|^2 + |\tilde{\mathbf{E}}(\mathbf{x})|^2 \right] + \frac{L^2 \epsilon_0}{2} |\bar{\mathbf{E}}|^2 \\
& + \epsilon_0 a^2 \sum_{\mathbf{x} \in D} \phi(\mathbf{x}) \left[\tilde{E}_x(\mathbf{x} + \frac{a}{2} \mathbf{e}_x) - \tilde{E}_x(\mathbf{x} - \frac{a}{2} \mathbf{e}_x) + \tilde{E}_y(\mathbf{x} + \frac{a}{2} \mathbf{e}_y) - \tilde{E}_y(\mathbf{x} - \frac{a}{2} \mathbf{e}_y) \right] && \text{(C.5)} \\
=& \frac{\epsilon_0 a^2}{2} \sum_{\mathbf{x} \in D} \left[|\tilde{\boldsymbol{\nabla}} \phi(\mathbf{x})|^2 + |\tilde{\mathbf{E}}(\mathbf{x})|^2 \right] + \frac{L^2 \epsilon_0}{2} |\bar{\mathbf{E}}|^2, && \text{(C.6)}
\end{aligned}$$

where the sum in the final term of the second line returns zero since it is a sum over the $\mathbf{k} \neq \mathbf{0}$ modes, and the sum over the auxiliary-field elements in Eq. (C.5) is zero because it is the sum of the rotational degrees of freedom of the field leaving site $\mathbf{x}$.

It follows that

$$U_0 = U_{\mathrm{Poisson}} + U_{\mathrm{Rot.}} + U_{\mathrm{Harm.}}, \tag{C.7}$$

where $U_{\mathrm{Poisson}} := \epsilon_0 a^2 \sum_{\mathbf{x}\in D} |\tilde{\boldsymbol{\nabla}}\phi(\mathbf{x})|^2/2$, $U_{\mathrm{Rot.}} := \epsilon_0 a^2 \sum_{\mathbf{x}\in D} |\tilde{\mathbf{E}}(\mathbf{x})|^2/2$, and $U_{\mathrm{Harm.}} := L^2\epsilon_0|\bar{\mathbf{E}}|^2/2$.

Appendix D

The Relationship between the BH and AHNS Theories

Combining Eqs. (6.36), (7.57) and (7.65), it follows that

$$\tilde{K}_{\text{eff.}}(L(\omega),T) = \frac{\beta J}{C} p(\omega,T) \left(1 + \left(\frac{q(\omega,T)}{p(\omega,T)}\right)^2\right) \tag{D.1}$$

in spin-stiffness notation (set as an equality as the Bishop-Reppy experiment is in the asymptotic regime). From the standard manipulation of complex numbers, we have that

$$\frac{q(\omega,T)}{p(\omega,T)} = \frac{\epsilon''(\omega,T)}{\epsilon'(\omega,T)}. \tag{D.2}$$

We combine this with Eqs. (7.63) and (7.64) to find that

$$\frac{q(\omega,T)}{p(\omega,T)} = \frac{\pi}{4} \left.\frac{\partial \ln(\epsilon(r,T))}{\partial \ln(r)}\right|_{r=L(\omega)}, \tag{D.3}$$

from which Eq. (D.1) becomes

$$\tilde{K}_{\text{eff.}}(L(\omega),T) = \frac{\beta J}{C} p(\omega,T) \left(1 + \left(\frac{\pi}{4} \left.\frac{\partial \ln(\tilde{K}_{\text{eff.}}^{-1}(r,T))}{\partial \ln(r)}\right|_{r=L(\omega)}\right)^2\right), \tag{D.4}$$

where $\tilde{K}_{\text{eff.}}^{-1}(r,T)$ is the static, distant-dependent effective spin stiffness that includes the effect of screening only from topological-defect pairs whose separation distance $d \leq r$, as defined by Nelson and Kosterlitz [9].

The BH ansatz [19] given by Eq. (2.135) amounts to asserting that the Nelson-Kosterlitz effective spin stiffness is constant across a sample. Hence, in order for the BH [19, 20] and

AHNS [10] theories to agree, we require that $\tilde{K}_{\mathrm{eff.}}(r,T)$ can be replaced with $\tilde{K}_{\mathrm{eff.}}(L,T)$ for all $r < L$, which is certainly true in the region of the critical point for topological defects ($T^*(L)$), where the Nelson-Kosterlitz effective spin stiffness becomes scale independent. In Fig. 7.3, the black circles (full AHNS theory) and the blue circles (constant Nelson-Kosterlitz effective spin stiffness) coincide. Outside of this region, where BH theory is not predicted to apply, we observe a deviation between these two data sets. There is therefore no contradiction between the two theories, since BH theory is only predicted to apply at $T = T^*(L)$.

Appendix E

Simulation Details

E.1 The Coulomb Gas

The two-dimensional Coulomb gas was simulated using the MR algorithm on an $L \times L$ lattice of lattice spacing $a = 1$. One charge-hop sweep corresponded to picking a charge site at random, picking the x or y direction at random, then proposing a charge hop in the positive or negative direction (at random), repeating this $2N$ times (replacing each site / field bond after each proposal). One auxiliary-field sweep corresponded to picking a charge site at random and proposing a field rotation around the site, repeating this N times (the range of field rotation was tuned at each temperature to keep the acceptance rates between 40 and 60%.). One global sweep corresponded to proposing a winding update in the positive or negative (at random) x and y directions. For all simulations, we performed five auxiliary-field sweeps per charge-hop sweep, and, for those simulations that also employed the global update, we performed one global update per charge-hop sweep. One charge-hop sweep corresponds to one Monte Carlo time step.

All data sets were averaged over multiple runs of 10^6 charge-hop sweeps per lattice site, with all those presented outside of Chapter 5 averaged over 16 runs, barring the $L = 64$ and $L = 128$ data sets, which were averaged over 48 runs.

The $L = 32$ data set in Fig. 5.2 was averaged over 512 runs between $T = 1.0$ and 1.1375, 992 and 768 runs between $T = 1.15$ and 1.45 with the global update off and on respectively, and over 256 runs between $T = 1.46$ and 1.75. The $L = 64$ data set in Fig. 5.2 was averaged over 608 and 446 runs between $T = 1.15$ and 1.45 with the global update off and on respectively, over 384 runs between $T = 1.5$ and 1.6, and over 256 runs between $T = 1.65$ and 1.75.

The $L = 8$ data set in Fig. 5.3 was averaged over 128 runs ($T = 0.1 - 1.1$), 256 runs ($T = 1.15 - 1.39; T = 1.41 - 1.44; T = 1.46 - 1.49$), 768 runs ($T = 1.4; T = 1.45; T = 1.5 - 1.75$), and 256 runs ($T = 1.8 - 2.5$); the $L = 16$ data set was averaged over 128 ($T = 0.1 - 1.1$) and 256 runs ($T = 1.15 - 2.5$); the $L = 32$ data set was averaged over 128 runs ($T = 0.1 - 1.1$), 256 runs ($T = 1.15 - 2.0$), and 128 runs ($T = 2.0 - 2.5$); the $L = 64$ data set was averaged over 128 runs ($T = 0.1 - 1.1$), 448 runs ($T = 1.15 - 1.45$), 384 runs ($T = 1.5 - 1.6$), 256 runs ($T = 1.65 - 2.0$), and 128 runs ($T = 2.05 - 2.5$).

We also simulated the $L = 10$, $L = 20$, and $L = 40$ systems over small temperature ranges to calculate additional crossover points for Fig. 5.4: all data sets were averaged over 512 runs.

E.2 The XY Models

The XY and HXY models were simulated using the standard Metropolis update scheme. One sweep corresponded to picking a spin site at random, then proposing a spin rotation, repeating this N times (replacing each site after each proposal). The range of spin rotation was tuned at each temperature to keep the acceptance rates between 40 and 60%.

All non-quench data sets were averaged over 16 runs of 10^6 sweeps per lattice site, barring the $L = 64$ data, which was averaged over 32 runs. The quench test performed on the HXY model in Chapter 6 was one run of 10^5 sweeps per lattice site.

Bibliography

[1] A. M. Salzberg and S. Prager. Equation of State for a Two-Dimensional Electrolyte. *J. Chem. Phys.*, 38:2587, 1963.

[2] V. L. Berezinskii. Destruction of Long-range Order in One-dimensional and Two-dimensional Systems having a Continuous Symmetry Group I. Classical Systems. *Sov. Phys. JETP*, 32:493, 1971.

[3] J. M. Kosterlitz and D. J. Thouless. Ordering, metastability and phase transitions in two-dimensional systems. *J. Phys. C: Solid State Phys.*, 6:1181, 1973.

[4] J. V. José, L. P. Kadanoff, S. Kirkpatrick, and D. R. Nelson. Renormalization, vortices, and symmetry-breaking perturbations in the two-dimensional planar model. *Phys. Rev. B*, 16:1217, 1977.

[5] M. R. Beasley, J. E. Mooij, and T. P. Orlando. Possibility of Vortex-Antivortex Pair Dissociation in Two-Dimensional Superconductors. *Phys. Rev. Lett.*, 42:1165, 1979.

[6] S. A. Wolf, D. U. Gubser, W. W. Fuller, J. C. Garland, and R. S. Newrock. Two-Dimensional Phase Transition in Granular NbN Films. *Phys. Rev. Lett.*, 47:1071, 1981.

[7] D. J. Resnick, J. C. Garland, J. T. Boyd, S. Shoemaker, and R. S. Newrock. Kosterlitz-Thouless Transition in Proximity-Coupled Superconducting Arrays. *Phys. Rev. Lett.*, 47:1542, 1981.

[8] P. Minnhagen. Universal resistive transition for two-dimensional superconductors. *Phys. Rev. B*, 24:6758, 1981.

[9] D. R. Nelson and J. M. Kosterlitz. Universal jump in the superfluid density of two-dimensional superfluids. *Phys. Rev. Lett.*, 39:1201, 1977.

[10] V. Ambegaokar, B. I. Halperin, D. R. Nelson, and E. D. Siggia. Dissipation in two-dimensional superfluids. *Phys. Rev. Lett.*, 40:783, 1978.

[11] D. J. Bishop and J. D. Reppy. Study of the Superfluid Transition in Two-Dimensional ^{4}He Films. *Phys. Rev. Lett.*, 40:1727, 1978.

[12] D. J. Bishop and J. D. Reppy. Study of the superfluid transition in two-dimensional ^{4}He films. *Phys. Rev. B*, 22:5171, 1980.

[13] R. J. Birgeneau and J. D. Litster. Bond orientational order model for smectic B liquid crystals. *J. Physique Lett.*, 39:L399, 1978.

[14] S. L. Sondhi, S. M. Girvin, J. P. Carini, and D. Shahar. Continuous quantum phase transitions. *Rev. Mod. Phys.*, 69:315, 1997.

[15] A. Trombettoni, A. Smerzi, and P. Sodano. Observable signature of the Berezinskii-Kosterlitz-Thouless transition in a planar lattice of Bose-Einstein condensates. *New J. Phys.*, 7:57, 2005.

[16] Z. Hadzibabic, P. Krüger, M. Cheneau, B. Battelier, and J. Dalibard. Berezinskii-Kosterlitz-Thouless crossover in a trapped atomic gas. *Nature*, 441:1118, 2006.

[17] V. M. Vinokur, T. I. Baturina, M. V. Fistul, A. Yu. Mironov, M. R. Baklanov, and C. Strunk. Superinsulator and quantum synchronization. *Nature*, 452:613, 2008.

[18] T. I. Baturina and V. M. Vinokur. Superinsulator–superconductor duality in two dimensions. *Ann. Phys.*, 331:236, 2013.

[19] S. T. Bramwell and P. C. W. Holdsworth. Magnetization and universal sub-critical behaviour in two-dimensional XY magnets. *J. Phys.: Condens. Matter*, 5:L53, 1993.

[20] S T Bramwell and P. C. W. Holdsworth. Magnetization: A characteristic of the Kosterlitz-Thouless-Berezinskii transition. *Phys. Rev. B*, 49:8811, 1994.

[21] A. Taroni, S. T. Bramwell, and P. C. W. Holdsworth. Universal window for two-dimensional critical exponents. *J. Phys.: Condens. Matter*, 20:275233, 2008.

[22] A. Vallat and H. Beck. Coulomb-gas representation of the two-dimensional XY model on a torus. *Phys. Rev. B*, 50:4015, 1994.

[23] J. Villain. Theory of one-and two-dimensional magnets with an easy magnetization plane. II. The planar, classical, two-dimensional magnet. *J. Physique*, 36:581, 1975.

[24] A. C. Maggs and V. Rossetto. Local Simulation Algorithms for Coulomb Interactions. *Phys. Rev. Lett.*, 88:196402, 2002.

[25] N. D. Mermin and H. Wagner. Absence of Ferromagnetism or Antiferromagnetism in One- or Two-Dimensional Isotropic Heisenberg Models. *Phys. Rev. Lett.*, 17:1133, 1966.

[26] D. J. Thouless. *Topology of Strongly Correlated Systems: Edited by P Bicudo et al.* World Scientific, Singapore, 2001. ISBN 9810245726.

[27] R. G. Palmer. Broken ergodicity. *Adv. Phys.*, 31:669, 1982.

[28] C.-A. Coulomb. Second mémoire sur l'électricité et le magnétisme. *Histoire de l'Académie Royale des Sciences*, page 578, 1785.

[29] W. Janke and K. Nather. Monte Carlo simulation of dimensional crossover in the XY model. *Phys. Rev. B*, 48:15807, 1993.

[30] L. Levrel, F. Alet, J. Rottler, and A. C. Maggs. Local simulation algorithms for Coulombic interactions. *Pramana*, 64:1001, 2005.

[31] V. Rossetto. *Mécanique statistique de systèmes sous constraintes : topologie de l'ADN et simulations électrostatiques. Deuxième partie : Simulations locales d'interactions coulombiennes.* PhD thesis, l'université Pierre-et-Marie-Curie, 2002.

[32] A. C. Maggs. Auxiliary field Monte Carlo for charged particles. *J. Chem. Phys.*, 120: 3108, 2004.

[33] A. C. Maggs and J. Rottler. Auxiliary field simulation and Coulomb's law. *Comput. Phys. Commun.*, 169:160, 2005.

[34] L. Levrel and A. C. Maggs. Boundary conditions in local electrostatics algorithms. *J. Chem. Phys.*, 128:214103, 2008.

[35] S. Raghu, D. Podolsky, A. Vishwanath, and D. A. Huse. Vortex-dynamics approach to the Nernst effect in extreme type-II superconductors dominated by phase fluctuations. *Phys. Rev. B*, 78:184520, 2008.

[36] S. T. Banks. *Fluctuations of Global Quantities in Highly Correlated Systems.* PhD thesis, University College London, 2005.

[37] P. Archambault, S. T. Bramwell, and P. C. W. Holdsworth. Magnetic fluctuations in a finite two-dimensional XY model. *J. Phys. A*, 30:8363, 1997.

[38] P. Minnhagen and B. J. Kim. Direct evidence of the discontinuous character of the Kosterlitz-Thouless jump. *Phys. Rev. B*, 67:172509, 2003.

[39] J. M. Kosterlitz. The critical properties of the two-dimensional XY model. *J. Phys. C: Solid State Phys.*, 7:1046, 1974.

[40] J. V. José, L. P. Kadanoff, S. Kirkpatrick, and D. R. Nelson. Erratum: Renormalization, vortices, and symmetry-breaking perturbations in the two-dimensional planar model. *Phys. Rev. B*, 17:1477, 1978.

[41] J. Tobochnik and G. V. Chester. Monte Carlo study of the planar spin model. *Phys. Rev. B*, 20:3761, 1979.

[42] D. C. Mattis. Transfer matrix in plane-rotator model. *Phys. Lett. A*, 104:357, 1984.

[43] H. Weber and P. Minnhagen. Monte Carlo determination of the critical temperature for the two-dimensional XY model. *Phys. Rev. B*, 37:5986, 1988.

[44] C. M. Lapilli, P. Pfeifer, and C. Wexler. Universality away from critical points in two-dimensional phase transitions. *Phys. Rev. Lett.*, 96:140603, 2006.

[45] J. Als-Nielsen, S. T. Bramwell, M. T. Hutchings, G. J. McIntyre, and D. Visser. Neutron scattering investigation of the static critical properties of Rb 2 CrCl 4. *J. Phys.: Condens. Matter*, 5:7871, 1993.

[46] S. G. Carling, P. Day, and D. Visser. Dimensionality crossovers in the magnetization of the weakly ferromagnetic two-dimensional manganese alkylphosphonate hydrates $MnC_nH_{2n+1}PO_3.H_2O$, $n = 2 - 4$. *J. Phys.: Condens. Matter*, 7:L109, 1995.

[47] S. J. Clarke, A. Harrison, T. E. Mason, G. J. McIntyre, and D. Visser. Magnetic ordering and fluctuations in the S= 1/2 square Heisenberg antiferromagnet $Cu(DCO_2)_2.4D_2O$. *J. Phys.: Condens. Matter*, 4:L71, 1992.

[48] T. Chattopadhyay, P. J. Brown, A. A. Stepanov, A. I. Zvyagin, S. N. Barilo, and D. I. Zhigunov. Antiferromagnetic ordering in Gd_2CuO_4. *J. Magn. Magn. Mater.*, 104:607, 1992.

[49] C. Bellitto, P. Filaci, and S. Patrizio. Zero-field magnetic susceptibility study of the magnetic phase transition in the two-dimensional ionic ferromagnet bis(benzylammonium) tetrabromochromate(II), $(C_6H_5CH_2NH_3)_2CrBr_4$. *Inorg. Chem.*, 26:191, 1987.

[50] A. Paduan-Filho and C. C. Becerra. Magnetic properties and critical behavior of the pure and diluted two-dimensional weak ferromagnet $(CH_3NH_3)_2Mn_{1-x}Cd_xCl_4$. *J. Appl. Phys.*, 91:8249, 2002.

[51] K. W. Krämer, H. U. Güdel, P. Fischer, F. Fauth, M. T. Fernandez-Diaz, and T. Hauß. Triangular antiferromagnetic order in the honeycomb layer lattice of $ErCl_3$. *Eur. Phys. J. B*, 18:39, 2000.

[52] F. C. Coomer, V. Bondah-Jagalu, K. J. Grant, A. Harrison, G. J. McIntyre, H. M. Rønnow, R. Feyerherm, T. Wand, M. Meißner, D. Visser, and D. F. McMorrow. Neutron diffraction studies of nuclear and magnetic structures in the S= 1/2 square Heisenberg antiferromagnets $(d_6\text{-}5CAP)_2CuX_4$ (x = Br and Cl). *Phys. Rev. B*, 75:094424, 2007.

[53] M. Pärnaste, M. Marcellini, E. Holmström, N. Bock, J. Fransson, O. Eriksson, and B. Hjörvarsson. Dimensionality crossover in the induced magnetization of Pd layers. *J. Phys.: Condens. Matter*, 19:246213, 2007.

[54] M. Pärnaste, M. Marcellini, and B. Hjörvarsson. Oscillatory exchange coupling in the two-dimensional limit. *J. Phys.: Condens. Matter*, 17:L477, 2005.

[55] F. Huang, M. T. Kief, G. J. Mankey, and R. F. Willis. Magnetism in the few-monolayers limit: A surface magneto-optic Kerr-effect study of the magnetic behavior of ultrathin films of Co, Ni, and Co-Ni alloys on Cu(100) and Cu(111). *Phys. Rev. B*, 49:3962, 1994.

[56] F. Huang, G. J. Mankey, M. T. Kief, and R. F. Willis. Finite-size scaling behavior of ferromagnetic thin films. *J. Appl. Phys.*, 73:6760, 1993.

[57] M. Gajdzik, T. Trappmann, C. Sürgers, and H. v. Löhneysen. Morphology and magnetic properties of submonolayer Gd films. *Phys. Rev. B*, 57:3525, 1998.

[58] W. C. Chew. Electromagnetic theory on a lattice. *J. Appl. Phys.*, 75:4843, 1994.

[59] F. L. Spitzer. *Graduate Texts in Mathematics: Volume 34*. Springer, New York, 1964. ISBN 978-1-4757-4231-2.

[60] J. J. Binney, N. J. Dowrick, A. J. Fisher, and M. E. J. Newman. *The Theory of Critical Phenomena: An Introduction to the Renormalization Group*. Oxford University Press, Oxford, 1992. ISBN 0198513933.

[61] A. Liebig, P. T. Korelis, M. Ahlberg, and B. Hjörvarsson. Experimental realization of amorphous two-dimensional XY magnets. *Phys. Rev. B*, 84:024430, 2011.

[62] S. Gayen, M. K. Sanyal, A. Sarma, M. Wolff, K. Zhernenkov, and H. Zabel. Polarized neutron reflectivity study of spin vortices formed in Gd-based Langmuir-Blodgett films. *Phys. Rev. B*, 82:174429, 2010.

[63] M. K. Mukhopadhyay, M. K. Sanyal, T. Sakakibara, V. Leiner, R. M. Dalgliesh, and S. Langridge. Polarized neutron scattering and sub-Kelvin magnetization measurements in two-dimensional gadolinium stearate Langmuir-Blodgett films. *Phys. Rev. B*, 74: 014402, 2006.

[64] M. Greiner, O. Mandel, T. Esslinger, T. W. Hänsch, and I. Bloch. Quantum phase transition from a superfluid to a Mott insulator in a gas of ultracold atoms. *Nature*, 415:39, 2002.

[65] T. Stöferle, H. Moritz, C. Schori, M. Köhl, and T. Esslinger. Transition from a strongly interacting 1D superfluid to a Mott insulator. *Phys. Rev. Lett.*, 92:130403, 2004.

[66] N. Murray, M. Krygier, M. Edwards, K. C. Wright, G. K. Campbell, and C. W. Clark. Probing the circulation of ring-shaped Bose-Einstein condensates. *Phys. Rev. A*, 88: 053615, 2013.